Aerosol processes in the Planetary Boundary Layer: High resolution Aerosol Mass Spectrometry on a Zeppelin NT Airship

Florian Rubach

JÜLICH
FORSCHUNGSZENTRUM

Schriften des Forschungszentrums Jülich
Reihe Energie & Umwelt / Energy & Environment Band / Volume 196

Forschungszentrum Jülich GmbH
Institute for Energy and Climate Research (IEK)
Troposphere (IEK-8)

Aerosol processes in the Planetary Boundary Layer: High resolution Aerosol Mass Spectrometry on a Zeppelin NT Airship

Florian Rubach

Schriften des Forschungszentrums Jülich
Reihe Energie & Umwelt / Energy & Environment Band / Volume 196

ISSN 1866-1793 ISBN 978-3-89336-918-8

Bibliographic information published by the Deutsche Nationalbibliothek.
The Deutsche Nationalbibliothek lists this publication in the Deutsche Nationalbibliografie; detailed bibliographic data are available in the Internet at http://dnb.d-nb.de.

Publisher and Distributor: Forschungszentrum Jülich GmbH
Zentralbibliothek
52425 Jülich
Tel: +49 2461 61-5368
Fax: +49 2461 61-6103
Email: zb-publikation@fz-juelich.de
www.fz-juelich.de/zb

Cover Design: Grafische Medien, Forschungszentrum Jülich GmbH

Printer: Grafische Medien, Forschungszentrum Jülich GmbH

Schriften des Forschungszentrums Jülich
Reihe Energie & Umwelt / Energy & Environment, Band / Volume 196

D 468 (Diss., Wuppertal, Univ., 2013)

ISSN 1866-1793
ISBN 978-3-89336-918-8

Contents

Abstract

Atmospheric aerosol plays an ambivalent role for mankind. On the one hand, aerosol is known to have adverse health effects and even increase mortality. On the other hand, a raised aerosol concentration in the atmosphere is the only anthropogenic contribution to the Earth's climate known to have a net cooling effect by scattering light and acting as cloud condensation nuclei (CCN). Among other things, the magnitude of these effects depend on the chemical composition of the aerosol.

In this work, an Aerosol Mass Spectrometer (AMS) was adapted for airborne aerosol chemical composition measurements on a Zeppelin NT airship. The Zeppelin platform allows for measurements with high spatial resolution throughout the entire planetary boundary layer (PBL). The new instrument was successfully operated aboard the Zeppelin NT on nine out of ten flight days of a seven week campaign in two countries in the context of the European project PEGASOS. The mass concentrations of the measured aerosol chemical species are presented for these days.

The campaign observations revealed a higher relative concentration of nitrate aerosol in the Netherlands compared to the Po Valley in northern Italy. For sulfate aerosol, the situation was opposite. Furthermore, the organic aerosol was more aged in the Po Valley than in the Netherlands.

The influence of the aerosol chemical composition on the cloud droplet activation was studied by computation of the critical activation diameter and comparing to aerosol number size distribution measurements. In some situations, the chemical composition was the driving force behind changes in CCN concentration, in other situations its effect was overshadowed by changes in the size distribution.

Differences between the individual layers of the PBL were identified in the mass concentrations of the aerosol chemical species and the organic aerosol age.

A backward trajectory analysis was used in conjunction with the obtained data to estimate the aerosol production rate of the Po Valley to 0.60 $(\mu g/m^3)/h$ for organic aerosol, 0.88 $(\mu g/m^3)/h$ for nitrate aerosol, and 0.15 $(\mu g/m^3)/h$ for sulfate aerosol.

The aerosol ion balance was used to gain insights into organic aerosol functionalization patterns.

1. Introduction

1.1. Atmospheric aerosol and its relevance

An aerosol is defined as a suspension of solid or liquid particulate matter in a gaseous medium. In the atmospheric science, the term aerosol often refers to the particulate phase only.

In the atmosphere, many apparent phenomena such as dust, smoke, fume, smog, haze, fog, or mist can be classified as aerosol (Seinfeld and Pandis, 1998). Generally, atmospheric aerosols consist of particles spanning a broad range of sizes from few nm to tens of µm. Particles can either be directly emitted into the atmosphere as primary aerosols (e.g. pollen, sea spray, ash, soot) or they are formed by chemical processing of precursor gases. Precursor gases are sulfur dioxide SO_2, nitrous oxides NO_x or volatile organic compounds (VOCs) from biogenic or anthropogenic sources. By the chemical processing, they produce substances with sufficiently low vapour pressures to either condense on pre-existing particles or form new ones by nucleation.

Particle size and composition change by various processes like evaporation, coagulation, chemical reactions, and the activation to a cloud droplet (Seinfeld and Pandis, 1998; Finlayson-Pitts and Pitts, 2000). Depending on the size of particles, different loss processes lead to atmospheric lifetimes of aerosol particles from minutes to weeks. One example of a loss process is the gravitational settling. The larger a particle is, the faster it deposits to the ground by this process. The smaller a particle is, the more its gravitational settling is limited by friction. For small particles collision with other particles and coagulation is an important sink. In a dry deposition situation, gravitational settling and inertial impaction of big particles and Brownian diffusion of small particles lead to a preferred removal of particles at the lower and upper end of the particle size spectrum. Particles in the intermediate size range can only effectively be removed by wet deposition, typically by the particles acting as a CCN or by being washed out by precipitation.

Particles can have adverse effects on human health. Especially small particles can penetrate deep into the lungs (Hussain et al., 2011), increasing the potential for harmful health effects. These effects are not limited to mere breathing problems; Klemm et al. (2000) for example reported an increased mortality rate from increased fine particulate matter concentrations. Pope (2007) concluded, that "adverse health effects are dependent on both exposure concentrations and length of exposure" and that "long-term exposures have larger, more persistent cumulative effects than short-term exposures".

Particles also influence the radiative budget of the Earth and thus play a role in the climate system. The direct effect of aerosol particles in the atmosphere can be cooling, because they reflect sunlight by scattering. On the other hand, light absorbing particles like soot can heat up from sunlight absorption, leading to a warming effect in the layer where they are present. This effect can shorten the lifetime of clouds and is classified as semidirect effect. Furthermore, aerosol particles indirectly act upon the climate by influencing the properties of clouds. At a constant water concentration, an increased CCN number concentration leads to more and smaller cloud droplets, effectively increasing the cloud albedo, i. e. its ability to scatter light back into space (Twomey, 1974). Additionally, an increased CCN number concentration leads to a prolonged cloud lifetime, also leading to a cooling effect on climate (Albrecht, 1989). The net climate effect of anthropogenic influence on aerosol concentrations is cooling, but the uncertainty of the strength especially of the indirect effects remains high as of today (IPCC, 2007, see Figure 1.1).

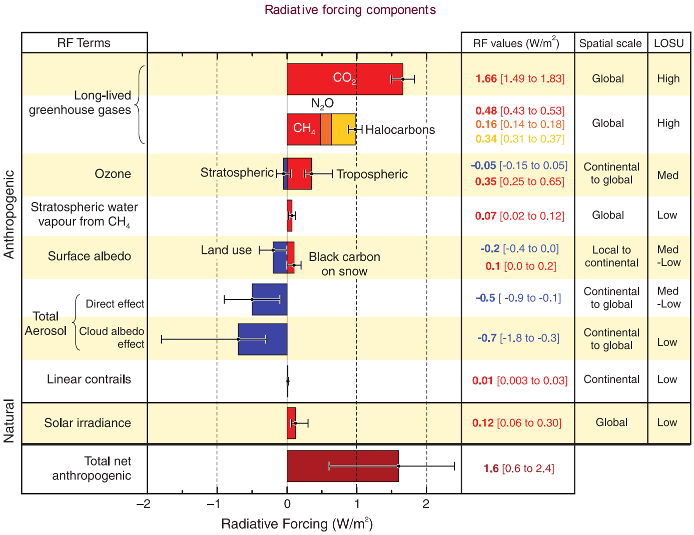

Figure 1.1.: Global average radiative forcing in 2005 (best estimates and 5 to 95% uncertainty ranges) with respect to 1750 for various contributors. Figure taken from IPCC (2007).

1.2. Aerosol properties

1.2.1. Particle concentration

According to Hinds (1999), the most commonly measured aerosol property is the mass concentration, being defined as the mass of particles in a unit volume of aerosol. For atmospheric aerosols, it is typically given in $\mu g/m^3$. Typical atmospheric mass concentrations range from $0.1\,\mu g/m^3$ to $1000\,\mu g/m^3$, special events such as dust storms ranging up to $1 \times 10^8\,\mu g/m^3$ (Seinfeld and Pandis, 1998; Hinds, 1999).

Aerosol concentrations are often also expressed based on their number concentration, the number of particles in a unit volume of aerosol. A common unit for the number concentration is cm^{-3}.

1.2.2. Particle size

The size of a particle influences all of its physical properties (Hinds, 1999). For example, increasing the diameter of a spherical particle by a factor of two gives a four times larger surface as well as an eightfold increased volume and mass.

Usually, particle size is given as physical or geometric diameters D_p in µm or nm. This measure assumes that the particles are spheres, which is approximately true for most liquid particles, but not necessarily for solid particles (Seinfeld and Pandis, 1998; Hinds, 1999). For irregularly shaped particles, equivalent diameters depending on the physical property of interest can be defined. The simplest example would be the equivalent volume diameter D_{ve}, representing a spherical particle with the same volume as the irregular particle. Other examples include the electrical mobility diameter D_{me}, characterizing the drift of a charged particle through a gas in an electric field, and the aerodynamic diameter D_a, characterizing the movement of a particle in air under the influence of the gravitation.

The electrical mobility diameter depends on gas properties, particle charge and D_p, but for example not on the particle density. This diameter is used for classification in a differential mobility analyser (DMA, see subsection 2.3.1 for details).

D_a for an irregular particle is defined as the diameter of a spherical particle with the density $1\,g/c\,m^3$ and an equivalent settling velocity (Hinds, 1999).The settling velocity is the maximum velocity a particle reaches when undergoing gravitational settling in air. It is reached, when the gravitational force is equal and opposite to the drag force of the surrounding medium. D_a depends on the size of a particle relative to the mean free path in the surrounding gas, the so called Knudsen number. The dependency on the Knudsen number simplifies at low pressures and is then called vacuum aerodynamic diameter D_{va} (Jimenez et al., 2003a; DeCarlo et al., 2004). This diameter is relevant for the classification of particle sizes in an AMS (see section 1.3 for details).

1.2.2.1. Particle size classification

Atmospheric aerosol particles appear at many sizes and corresponding concentrations. This is described by aerosol size distributions. As the particle diameter is a continuous quantity, listing the concentrations for each particle size is infeasible. Instead, the particles are usually classified into intervals. Atmospheric aerosol size distributions usually have continuously enough particle numbers in each size class to be approximated as continuous size distributions with finite but small classification intervals. It is often possible to describe observed size distributions as a sum of individual log-normal distributions as defined in Equation 1.1 (Seinfeld and Pandis, 1998).

$$n^{\circ}{}_{N}\left(\log D_p\right) = \frac{N}{\sqrt{2\pi}\log\sigma}\exp\left(-\frac{\left(\log D_p - \log\overline{D}_p\right)^2}{2\left(\log\sigma\right)^2}\right) \tag{1.1}$$

Here, N is the number concentration, D_p is the particle diameter, $\overline{D}_p$ is the mean particle diameter and σ is the standard deviation of the log-normal distribution.

Following Jaenicke (1993), a typical remote continental aerosol size distribution can be modelled using three log-normal distributions with their mean particle sizes at around 0.02 µm, 0.1 µm and 1.8 µm. The resulting size distribution is shown in Figure 1.2, Figure 1.3 and Figure 1.4, plotted as number, surface and volume distribution, respectively.

In terms of number concentration (Figure 1.2), the most prominent peak in the distribution is located mainly between 0.01 µm and 0.1 µm. Particles in this size range are typically called Aitken mode particles. These particles can be formed by gas-to-particle conversion. One example of such a process would be the condensation of hot vapours produced by combustion processes. Also homogeneous nucleation of a substance with high enough concentration and low enough vapour pressure can yield Aitken mode particles. Observations in the last decade revealed, that these and other processes can also produce particles smaller than 0.01 µm, called nucleation mode particles (not shown, Kulmala et al., 2004). Due to their low mass and small size, studying these particles is difficult. They have been observed as a distinct mode only in short bursts of very high number concentrations close to their source. Nucleation mode and Aitken mode particles usually have a short lifetime. Partly, this is because they can serve as nuclei for condensation of species with low vapour pressures. Also, they can coagulate with bigger particles.

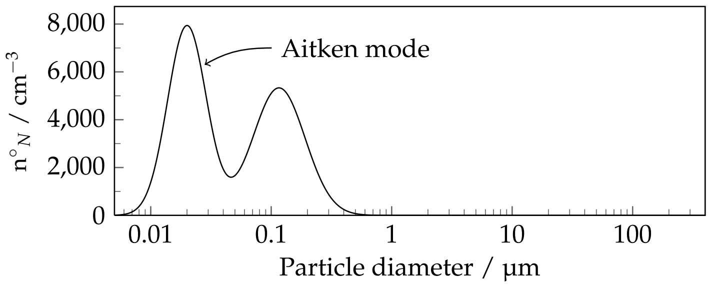

Figure 1.2.: Typical remote continental aerosol size distribution, modelled using three log-normal size distributions. The parameters for this plot are taken from Jaenicke (1993).

Looking at the particle size distribution in terms of particle surface (Figure 1.3), the most significant peak is located between 0.1 µm and 1 µm. These particles are considered to constitute the accumulation mode. Coagulation of Aitken mode particles typically result in particles of this size range. Accumulation mode particles can also be directly emitted into the atmosphere, for example by incomplete combustion. The name of this mode originates from the fact, that particle removal effects such as coagulation or gravitational settling are least effective here (Seinfeld and Pandis, 1998; Finlayson-Pitts and Pitts, 2000). Coagulation is a slow process for accumulation mode particles and due to the logarithmic nature of the size distribution, a coagulation of two accumulation mode particles produces another accumulation mode particle in most cases (Seinfeld and Pandis, 1998). Accumulation mode particles typically make up the dominant part of the surface concentration, with the consequence that interaction with the gas phase is maximal in this size range. The main removal process for the accumulation mode is wet deposition. When aqueous-phase chemical reactions take place after wet deposition in fog or cloud droplets, the evaporation of these droplets can yield in larger particles, leading to two modes in the range of 0.1 µm to 1 µm (not depicted). The smaller one of these modes is called the condensation mode, the larger one the droplet mode (Hering and Friedlander, 1982). The combination of Aitken mode and accumulation mode particles is often referred to as fine particles.

Figure 1.4 depicts the size distribution in terms of particle volume. It can be seen that the particles with more than 1 µm in diameter contribute the most to the total volume. These particles are termed coarse mode particles. They are usually

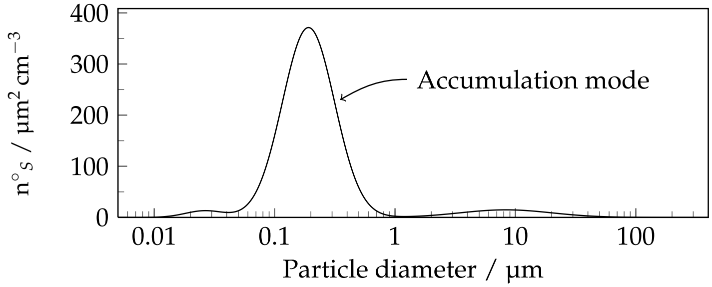

Figure 1.3.: The same size distribution as in Figure 1.2, expressed in terms of particle surface.

directly emitted into the atmosphere by mechanical processes. Anthropogenic coarse particles can for example originate from industrial or agricultural processes. Also, abrasion of tires and road material from traffic can be a source. Naturally produced coarse particles include pollen and bacteria as well as particles from bubble bursting or wave breaking on the ocean. Coarse particles settle on short time scales by means of sedimentation.

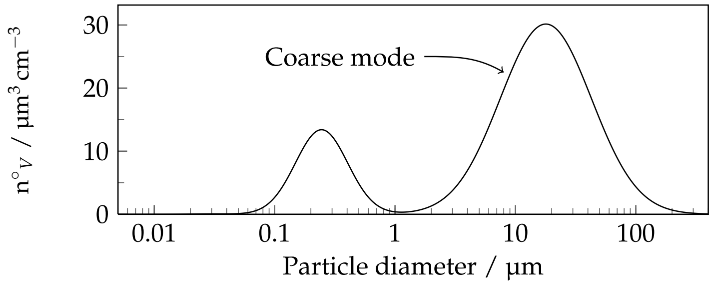

Figure 1.4.: The same size distribution as in Figure 1.2, expressed in terms of particle volume.

As can be seen from Figure 1.2, Figure 1.3 and Figure 1.4, the importance of the different particle sizes can vary greatly, depending on whether the number, surface or volume concentration is of interest. The fine mode usually makes up the majority of particles by number, but usually only makes up a few percent of the total mass (Finlayson-Pitts and Pitts, 2000). This can be illustrated when looking at spherical particles of identical composition: It would need one thousand particles of 100 nm diameter or one million 10 nm particles to get to the same particulate mass as by a single particle of 1 µm diameter. For toxicological effects related to the number of particles, the fine mode is more important than other modes. The accumulation mode generally has a considerable fraction of the mass and the majority of the surface area (Finlayson-Pitts and Pitts, 2000). Therefore, this mode is of importance for gas phase deposition and other heterogeneous chemistry processes. The coarse mode has the largest mass fraction of the particulate matter. Although the effect on visibility per unit particle mass is bigger for accumulation mode particles, the coarse mode particles can have a significant contribution to the reduction of visibility due to their higher mass concentration (Seinfeld and Pandis, 1998).

The mass concentration of particles is often used as an indicator for air quality. The notations PM_{10}, $PM_{2.5}$, and PM_1 are commonly used and refer to the particle mass concentration of all particles up to 10 µm, 2.5 µm, and 1 µm aerodynamic diameter, respectively.

1.2.3. Tropospheric aerosol

Tropospheric aerosol is composed of varying amounts of sulfate, nitrate, ammonium, sodium, chloride, crustal materials, trace metals, water and carbonaceous materials (Seinfeld and Pandis, 1998).

Sulfate aerosols arise from atmospheric oxidation of sulfur-containing compounds such as SO_2 or dimethyl sulfide (DMS). The former is, except from volcanic eruptions, mainly of anthropogenic origin, whereas the latter is produced by biogenic processes. Except from minor contributions by sea spray, sulfate aerosol is a secondary aerosol. Nitrate aerosols can be formed from the atmospheric oxidation of NO_x, which can have anthropogenic or biogenic sources. Nitrate aerosols are produced by atmospheric processes and are thus of secondary character. Ammonia originates in the degradation of plant litter and animal faeces. It can neutralize sulfate and nitrate aerosols initially formed as H_2SO_4 and HNO_3.

Sodium and chloride in aerosols mainly come from sea spray, even hundreds of kilometres from the coast (Seinfeld and Pandis, 1998). Chloride can also originate from the neutralization of HCl vapours which can be formed by incinerators or power stations (Seinfeld and Pandis, 1998). Crustal materials are for example soil dust or windblown minerals (Seinfeld and Pandis, 1998). Trace metals in aerosols can originate from the combustion of leaded fuels (Peirson et al., 1974), but also from plants (Beauford et al., 1975). In addition particles contain water, depending on the relative humidity.

Carbonaceous materials in aerosols can be divided in the categories elemental carbon (EC) and organic carbon (OC). Elemental carbon, also called black carbon or soot is a primary aerosol directly emitted predominantly in incomplete combustion processes. Organic carbon aerosol can be directly emitted into the atmosphere by biomass burning and other combustion processes, but it can also arise from secondary organic aerosol (SOA) formation.

SOA will be formed, when VOCs undergo multistep atmospheric oxidation by ozone, $OH \cdot$ or $NO_3 \cdot$ (Pandis et al., 1992). The products of such oxidation usually have a lower vapour pressure than the reactants (Odum et al., 1996; Hoffmann et al., 1997; Kamens and Jaoui, 2001). When the supersaturation of a product is high enough to overcome the nucleation barrier imposed by the Kelvin effect (von Helmholtz, 1886), it will condense and form particles. This process is called homogeneous nucleation. However, when pre-existing particles are available, the oxidation products can condense on these without supersaturation. It is then sufficient to reach the saturation vapour pressure determined by the given mixture.

Biogenic sources have been estimated to emit 430-1150 Tg carbon per year in the form of VOCs, whereas anthropogenic sources are estimated to 160 Tg carbon per year (Fehsenfeld et al., 1992; Guenther et al., 1995). Biogenic VOCs are for example isoprene, monoterpenes, and sesquiterpenes. Typical anthropogenic emissions include alkanes, alkenes, and benzene and toluene.

Studies have shown, that SOA makes up more than 50 % of the total observed organic aerosol (Kanakidou et al., 2005). Figure 1.5 shows the composition of non-refractory sub-micron aerosol particles, i. e. composed of material that evaporates at 600 °C, in the northern hemisphere (Zhang et al., 2007). The instrument used for the measurement of these compositions is the AMS (see section 1.3), which was also employed in this study. In all measurement sites, organic material constitutes a significant portion (18 % to 70 %) of the detected total aerosol mass, although the AMS cannot detect refractory aerosols such as elemental carbon.

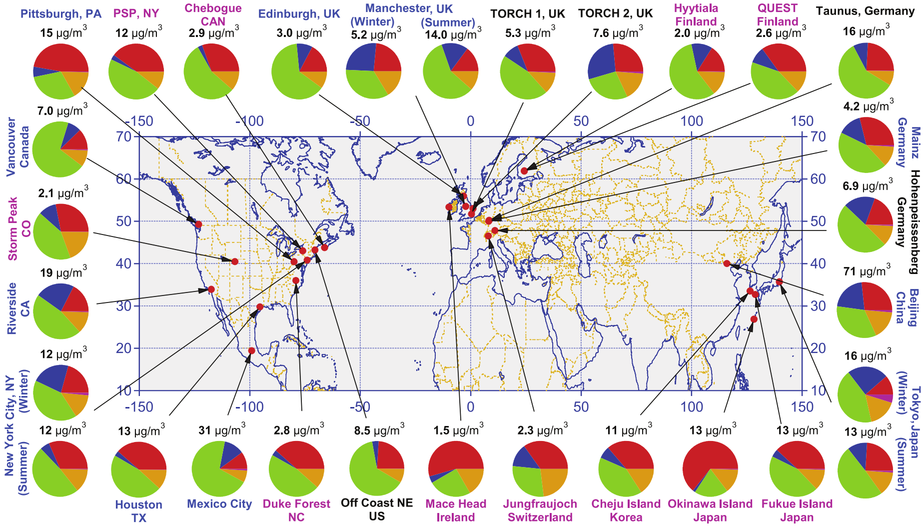

Figure 1.5.: Chemical composition and average mass concentration as measured with the Aerosol Mass Spectrometer in various locations in the northern hemisphere. Blue font indicates urban areas, black font stands for locations downwind of urban areas and pink means a rural/remote sampling site. The pie charts show the chemical composition, apportioned in organics (green), sulfate (red), nitrate (blue), ammonium (orange) and chloride (purple). Figure taken from Zhang et al. (2007).

1.3. Aerosol mass spectrometry

In the last century, analysis of atmospheric aerosol chemical composition was limited to collecting particulate matter on filters for long periods of time and analysing these filters with classic analytical techniques. This type of analysis is referred to as an offline technique, because sampling the aerosol and analysing it are separate processes. Instrumental advances in the last decades made it possible to use online mass spectrometry on in situ evaporated aerosol particles. An instrument capable of measuring the chemical composition of non-refractory aerosol particles in real-time using mass spectrometry is the AMS (Jayne et al., 2000; Jimenez et al., 2003b). It has been developed by Aerodyne Research Incorporation, Billerica, United States of America. It determines the composition of measured aerosol via the acquisition of mass spectra, either size-resolved or averaged over all sampled particle sizes. The instrument used in this study is based upon a variant of the instrument first described in DeCarlo et al. (2006). This variant employs a high resolution time of flight mass spectrometer instead of the quadrupole mass spectrometer used in earlier versions of the instrument and is called High Resolution Time of Flight Aerosol Mass Spectrometer (HR-ToF-AMS).

The AMS was applied in many laboratory and field studies (see Canagaratna et al., 2007 and the references therein, for long term field observations also see Zhang et al., 2007). It can determine the size resolved aerosol composition in terms of inorganic species and the total of organics. Using statistical techniques like positive matrix factorization (PMF, Paatero and Tapper, 1994), it is possible to divide the organic fraction into several sub classes associated with hydrocarbon-like organic aerosol (HOA), oxidised organic aerosol (OOA) and other organic aerosol types (Ulbrich et al., 2009; Zhang et al., 2011).

The instrument is described in detail in section 2.4.

1.4. Pan-European gas-aerosols-climate interaction study (PEGASOS)

The Pan-European gas-aerosols-climate interaction study (PEGASOS) is a large scale integrating project with 26 European partner organizations. The project aims at quantifying the magnitude of regional to global feedbacks between atmospheric chemistry and a changing climate and reducing the corresponding uncertainty of the major ones (Pandis, 2010; FORTH/ICE-HT). Also, mitigation strategies and policies to improve air quality while limiting their impact on climate change are to be identified (Pandis, 2010; FORTH/ICE-HT).

A series of scientific questions detailing the aforementioned objectives are addressed by the project in the form of 18 work packages in 4 themes. The studies performed in this work are part of the work package “Airborne field studies” in theme “Atmospheric Processes”, along with work packages dealing with ground based observations, laboratory studies, and data integration and parametrization. The other themes deal with emissions and exchange processes, links between air pollution and climate change, and the integration with policy.

1.5. Planetary boundary layer (PBL)

The PBL is the lowest part of the atmosphere, in direct contact with the surface. Its structure is influenced by radiative processes, leading to a characteristic evolution as a function of daytime (depicted in Figure 1.6).

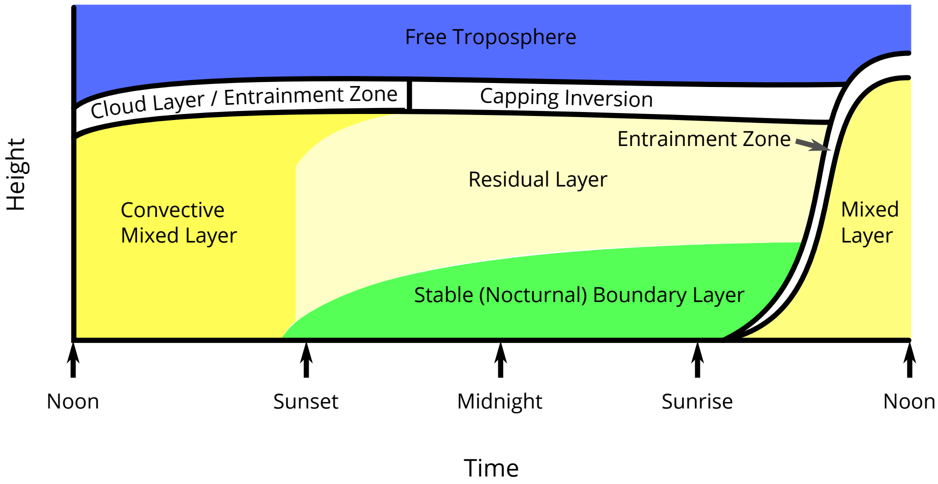

Figure 1.6.: Idealized boundary layer evolution (graph adapted from Stull, 1988). Three major parts are the very turbulent mixed layer, a less turbulent residual layer containing former mixed layer air, and the stable nocturnal boundary layer (Stull, 1988).

Under ideal conditions, the earth's surface heats up during the day, leading to a single, convectively mixed layer (ML) throughout the PBL. In the evening, radiative cooling lowers the temperatures starting from the ground, with warmer air above. This inverted temperature profile prevents mixing of air masses to higher levels, hence the newly formed layer at the earth surface is called stable nocturnal boundary layer (NBL). Above the NBL, the air still has a temperature profile similar to the day before, but no longer has direct contact to the surface and its emissions. This layer is called the residual layer (RL), as it reflects the residual of the previous days ML. In the morning, radiative heating of the earth's surface causes a new ML to grow from the ground, first incorporating the NBL and then the RL. The evolving ML is capped by an entrainment zone, where overshooting of convective processes leads to an entrainment of air from above.

To better classify the stability or instability of a layer including effects from pressure and water content, the equivalent potential temperature θ_e is used in this work. θ_e is defined as the temperature an air parcel would reach if it was brought adiabatically to standard pressure and all water in the parcel would condense (Bolton, 1980).

1.6. Focus of this work

The main goal of this work was to enable mobile measurements of aerosol chemical composition throughout the entire PBL and give insights into details of regional aerosol chemical processes.

While there have been numerous airborne studies of aerosol chemical composition (see Heald et al., 2011 and the references therein), there have been only few airborne research activities with a focus on measurements in the PBL (Bahreini et al., 2003; Sorooshian et al., 2008; Murphy et al., 2009; Morgan et al., 2010; Nowak et al., 2010), of which only two (Sorooshian et al., 2008; Nowak et al., 2010) performed low altitude measurements over land. Previous studies were limited by the fact, that fast-moving aircraft with sufficient scientific payload rarely get permits for flying low over populated area. Furthermore, the velocity of such aircraft means, that within a regular time resolution of minutes, a large distance is covered. Increasing the time resolution however, would lead to low signal to noise ratios and is not a suitable solution.

The Zeppelin NT overcomes these limitations of gas phase and aerosol measurements in the PBL. With its scientific payload of approx. 1 ton and the ability to operate at low velocities throughout the lowest kilometre of the atmosphere, it is an ideal platform for characterizing the PBL in terms of height profiles and local chemical processes, as well as the dynamic processes in the PBL evolution.

A significant part of this work was focused on opening the use of this new platform for aerosol mass spectrometry by the adaptation of an aerosol mass spectrometer to aeronautic requirements (see section 2.5 and section 2.6).

Subsequently, 10 measurement flights were performed during a set of two consecutive campaigns in two European countries over the course of seven weeks. An overview of the data obtained during these flights is presented in chapter 3. Elected aspects of the observations are discussed in detail in chapter 4.

2. Experimental section

2.1. PEGASOS campaigns

In 2012, Zeppelin based measurements with the AMS were performed in two regions. For the eastbound PEGASOS campaign, the airship was transferred to Rotterdam, NL, where flights were performed from 19 May to 27 May. Flights with AMS measurements during this period are tabulated in Table 2.1 below.

Table 2.1.: 2012 PEGASOS flights starting from Rotterdam.

Date	Flight No.	Meteorology at airport, 10 UTC
21 May	F011	Clear sky, 19 °C, 70 % RH, wind NNW 4-7 knots
22 May	F012	Clear sky, 23 °C, 65 % RH, wind NW 4-6 knots
24 May	F013	Clear sky, 26 °C, 55 % RH, wind NE 6-9 knots

During this period, a weak low pressure system over central Europe was displaced by a strong high pressure system over northern Europe, leading to winds from northerly directions. The flight tracks starting from Rotterdam are shown in Figure 2.1. The background of Figure 2.1 (and Figure 2.2) corresponds to elevation data taken from publicly available Shuttle Radar Topography Mission (SRTM, Jarvis et al., 2008) data.

Afterwards, the Zeppelin NT was relocated to Ozzano, IT for the southbound PEGASOS campaign. From there, flights into the Po Valley were performed from 18 June to 13 July. Flights with AMS measurements during this period are tabulated in Table 2.2.

The meteorology in the Po valley during the period of measurements was largely influenced by low pressure systems in the northwest of Europe and in the western Mediterranean. These systems triggered the transport of air masses from southwest and west across the Apennines into the Po Valley (21 June, 25 June, 30 June to mid July). When the low pressure regimes in the northwest of Europe moved to the northeast of Europe, air masses were transported into the Po Valley over the Adriatic Sea from the east. Additionally, there was a sea breeze / land breeze

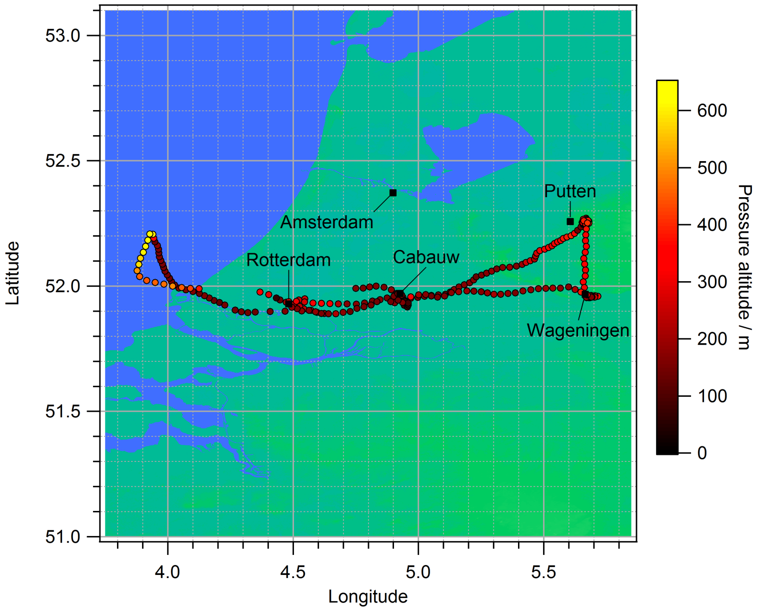

Figure 2.1.: Overview of flight tracks with the AMS on board of the Zeppelin NT in the Netherlands during the 2012 westbound PEGASOS-Campaign. The shown data points are coloured by pressure altitude.

Table 2.2.: Summary of 2012 PEGASOS flights starting from Ozzano.

Date	Flight No.	Meteorology at airport, 10 UTC
20 June	F027, F028	Clear sky, 35 °C, 30 % RH, wind W 4-6 knots
21 June	F029, F030	Clear sky, 33 °C, 30 % RH, wind NW 5-7 knots
22 June	F031	Clear sky, 31 °C, 40 % RH, wind WNW 6-8 knots
24 June	F032	Clear sky, 30 °C, 50 % RH, wind variable 2-3 knots
1 July	F039	Clear sky, 34 °C, 30 % RH, wind variable 3-4 knots
3 July	F040	Clear sky, 30 °C, 40 % RH, wind WNW 4-6 knots
4 July	F041	Clear sky, 30 °C, 40 % RH, wind variable 3-4 knots

effect on the Po Valley air circulation from 1 July on. Overall, the wind speeds were low.

The flight tracks starting from Ozzano are shown in Figure 2.2.

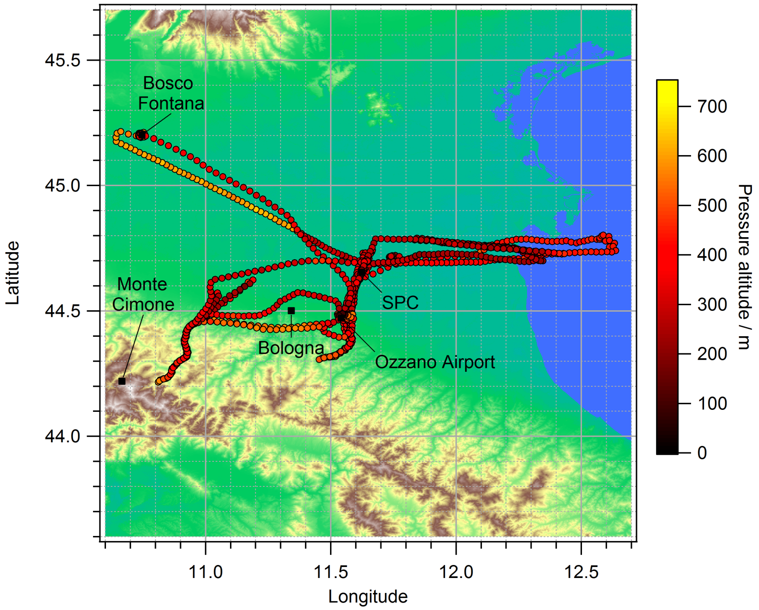

Figure 2.2.: Overview of flight tracks with the AMS on board of the Zeppelin NT in Italy during the 2012 southbound PEGASOS-Campaign. The shown data points are coloured by pressure altitude.

2.2. Airship Zeppelin NT as a measurement platform

The Zeppelin NT is a semi-rigid airship of 75 m length and a maximum hull diameter of 14 m. Using He as lifting gas, it achieves a maximum payload of 1900 kg. It is propelled by three engines, one in the back and two at the sides. The side engines can be turned upward by 90° and downward by 30°. The aft engine powers a sidewards mounted steering propeller as well as a pushing propeller capable of turning 90° downward. The propeller configuration allows for take-off and landing without horizontal velocity. The Zeppelin NT has a cruising speed of 115 km/h, a maximum flight endurance of 24 h, a maximum range of 900 km, and a maximum flight altitude of 2600 m. The maximum altitude which can actually be reached is limited by several factors. The expansion of He inside the hull due

Figure 2.3.: Airship Zeppelin NT as used during the 2012 PEGASOS mission. The Top-Platform is highlighted in red, the gondola including a nose-boom in blue, and the Mast-Truck in green.

to reduced outside pressure at higher altitudes defines the pressure limit. This limit is maintained when changing altitudes by inflatable compartments inside the airship hull (Ballonets), containing varying amounts of ambient air. When there is no air in the Ballonets and the maximum He pressure is reached, the Zeppelin is flying at maximum altitude. The amount of payload influences how much He has to be used. The more He, the less inflated the Ballonets can be at ground level, limiting the ability to compensate for reduced pressure at higher altitude. Another factor influencing the reachable altitude is the ambient temperature. When it rises, the density of air decreases, reducing the difference in density to He and hence reducing the lifting capacity. An effect increasing the maximum altitude is the so called superheat effect. When absorption of solar radiation increases the temperature of the Zeppelin hull, the He therein is warmed beyond the ambient temperature, increasing the density difference between He and the surrounding air. Considering all the aforementioned factors, the maximum achievable altitude for the heaviest instrument combination, containing the AMS and weighing more than 1000 kg, was varying between 400 m and 750 m.

The airship is trimmed so the take-off is done with a total weight of the airship of about 300 kg. For landing, the Zeppelin NT comes to ground and is then pulled to and connected with the truck-mounted mooring mast (highlighted in green in Figure 2.3). Afterwards, it can spin freely around this mast, analog to a flag on a pole.

For the scientific experiments during the PEGASOS campaign, a Top-Platform of approx. 500 kg was strapped to the top of the airship (highlighted in red in Figure 2.3). Further instrumentation was installed inside the gondola (highlighted in blue in Figure 2.3). These instruments were mounted to the seat rail instead of passenger seats and sampled air via inlet lines either from the nose-boom at the tip of the gondola, from below the bottom hatch or from a window in one of the two doors of the gondola.

2.2.1. Cabin layouts

Because of space and mass limitations, not all instruments developed for the Zeppelin-based measurements can be installed at the same time. For different scientific tasks, the instruments have been grouped into three distinct combinations, named cabin layouts. The cabin layouts are characterized by the letters CL and a number. The instrument racks in a cabin layout are referred to by a three letter acronym.

There are several instrument racks present in every cabin layout, namely CPN, COD, NOX, and Top-Platform. The CPN rack contains instruments to measure particle size distributions from 1 nm to 20 µm and particle number concentrations. The COD instrument measures the concentration of CO. The NOX rack contains instruments to measure concentrations of NO, NO_2, and O_3. It also houses a spectroradiometer with a downward-looking entrance optic, measuring the upwelling spectral actinic flux density in the wavelength range of 280 nm to 650 nm. Photolysis frequencies are calculated from this spectroradiometer and a second, upward-looking one on the Top-Platform. The Top-Platform also contains instruments based on laser-induced fluorescence. These instruments measure the concentration of highly reactive $OH\cdot$ and $HO_2\cdot$ radicals, and the total reactivity of $OH\cdot$ radicals (Holland et al., 2003; Lu et al., 2010).

The cabin layout CL8 additionally contains the LOP, FFL, and HGC racks to characterize photochemistry in more detail. The LOP rack houses a long path absorption instrument to measure nitrous acid (HONO, Häseler et al., 2009). The FFL rack contains a laser-induced fluorescence instrument for the detection of formaldehyde (HCHO, Hottle et al., 2009). The HGC rack consists of a fast gas chromatography system coupled with a quadrupole mass spectrometer, used for determining VOC concentrations.

Cabin layout CL9 consists of the always present instruments and the API and NAS instruments, suitable for investigating nucleation in more detail. The API rack comprises an atmospheric pressure interface time-of-flight mass spectrometer (APi-TOF). It can determine the composition of naturally charged ions and clusters up to m/z 1000 (Junninen et al., 2010). The NAS rack contains a nanometre air ion spectrometer, measuring the distribution of ions over a range of electrical mobilities and the distribution of aerosol particles in the size range of 2 nm to 40 nm.

2.3. The SOA cabin layout

CL5 is the cabin layout for Secondary Organic Aerosol measurements. For this cabin layout, three instruments are mounted into the cabin in addition to the always present instruments described in subsection 2.2.1. As data of the instruments in CL5 is used in this work, they are described in more detail below.

2.3.1. CPN rack

The CPN rack contains a particle size magnifier (PSM, Vanhanen et al., 2011), three condensation particle counters (CPC, Agarwal and Sem, 1980), two aerosol neutralisers, two differential mobility analysers (DMA, Liu and Pui, 1974), and an optical particle counter (OPC).

Air is sampled through three stainless steel inlet lines at the bottom of the Zeppelin. Through one inlet line, sampled air passes the PSM into a CPC, determining the total particle number concentration. The PSM condenses supersaturated ethylene glycol vapour on particles as small as 1 nm, growing them to sizes measurable by a CPC. The second inlet line splits into two flows, one going through an aerosol neutraliser and the nano-DMA into the second CPC, the other going through another aerosol neutraliser and a long DMA into the third CPC. In these instruments, the particle size distribution between 2.5 nm and 440 nm is measured. The OPC samples through the third inlet line, optically determining the size distribution of particles between 250 nm and 30 µm.

In a CPC, supersaturated vapours are condensed on particles, effectively increasing their diameter. The resulting bigger particles are then individually detected by an optical system. Using the number of particles detected per unit of time and the volume of air going through the CPC in the same amount of time, a concentration of particles per volume can be calculated.

In the aerosol neutraliser, the β-decay of ^{85}Kr is used to ensure always the same equilibrium charge distribution of sampled aerosol particles.

The nano-DMA and long DMA are variants of the same instrument. It contains two concentric metal cylinders. At the top of the space between the cylinders, aerosol and particle free sheath air are introduced. The sheath air surrounds the inner cylinder as a laminar flow, the aerosol forms a second laminar flow along the inner walls of the outer cylinder, around the sheath air. When a negative voltage is applied to the inner cylinder while the outer cylinder is grounded, positively charged particles are attracted to the inner cylinder and drift through the sheath air. Particles with a high electrical mobility and therefore a small mobility diameter reach the inner cylinder further up than particles with low electrical mobility. At the given voltage, particles with a certain mobility diameter reach a small slit at the bottom of the central cylinder, from where they leave the DMA to the CPC. All particles not exiting through the slit are either collected on the inner cylinder or removed with an excess flow. The particles leaving through the slit at a given voltage are called a size class and can be considered to be monodisperse with the electrical mobility diameter D_{me}.

The nano-DMA's dimensions are optimized so monodisperse particles with mobility diameters of 2.5 nm to 70 nm can be selected to leave the DMA. The long DMA can select monodisperse particles between 10 nm and 440 nm. These values depend on the flows applied in the DMA. Here, the values for the used flows are reported. The voltages of the inner cylinders are scanned, controlled by a computer. The number density N in each size class is determined by the CPC's downstream of the DMA's. Particle size distributions are determined when N in each size class is plotted as a function of D_{me}.

In the OPC, light scattering of particles according to the Mie theory is used to determine their size distribution.

CPN rack data used in this work were provided by R. Tillmann.

2.3.2. PSI rack

The PSI rack contains an Aethalometer, a Welas optical particle spectrometer, and a white-light humidified optical particle spectrometer (WHOPS). It has been developed at the Paul Scherrer Institute, Villingen, Switzerland.

The Aethalometer measures the aerosol light absorption coefficient which is translated into the ambient black carbon mass concentration. For this purpose, air is sampled through a quartz fibre filter tape. The blackening of the tape due to absorbing aerosol particles is monitored at different wavelengths, while keeping track of the unloaded filter tape as a reference signal. The black carbon concentration is calculated from the attenuation of reflected light with respect to the reference. When the filter tape gets too dark, it is advanced to a new position, allowing to continue the measurements.

A flow of 5 l/min is directly guided into a Welas optical particle counter, where particles are illuminated in a sampling volume. The particles scatter the light into a detector positioned in a 90° angle to the incoming light. Calibrating with materials of known size and refractive index, the resulting scattered light intensity for each particle can be attributed to a particle diameter. In this way the polydisperse number size distribution of particles with diameters larger than 200 nm is measured.

The WHOPS contains a diffusion drier, a DMA, a humidifier, and another Welas optical particle counter. Sampled aerosol is first dried and then guided into a DMA, where particles with a specific D_{me} are selected. The resulting monodisperse aerosol is then guided into an optical particle counter, alternatingly with or without a humidification. Without humidification, the resulting particle size distribution reflects the variation of optical properties for the dried particles of the selected mobility diameter. The hygroscopic growth factor at approx. 93 % relative humidity can be determined by comparing the dry and humidified particle size distributions.

PSI rack data shown in this work are preliminary and part of a dissertation by B. Rosati.

2.3.3. HGC rack

The HGC rack contains a fast gas chromatography system with a quadrupole mass spectrometer as detector. It is capable of identifying and quantifying more than 50 volatile organic compounds (VOC), among others Alkanes, Aromatics, Ketones, and Terpenes. The detection limits for these substances are in the low ppt range. Three minute chromatograms are acquired after adsorbing for three minutes. The alternation of sampling and analysis is performed by two identical subsystem working as a tandem system. This leads to a time resolution of three minutes.

2.3.4. NOX rack

The NOX rack contains instruments for measuring NO, NO_2, and O_3. NO and NO_2 are detected via a modified commercial chemiluminescence detector from Eco Physics (CLD TR 780, Rohrer and Brüning, 1992). In it, NO_2 is photolytically converted to NO via a LED. The sum of NO and NO_2 (NO_x) is detected when the LED is on, without LED, only NO is detected. From the difference of the detected signals, the NO_2 mixing ratio is calculated. Sensitivity changes by water vapour variations and oxidation of NO with ambient O_3 in the inlet line are corrected for. The accuracy of the instrument has been determined to $\pm 7\,\%$ (Rohrer and Brüning, 1992). O_3 is measured by a commercial UV absorption instrument (ANSYCO O341M).

NOX rack data shown in this work are preliminary and are provided by F. Rohrer.

2.4. The Aerosol Mass Spectrometer (AMS)

A schematic drawing of the HR-ToF-AMS employed in this work is shown in Figure 2.4.

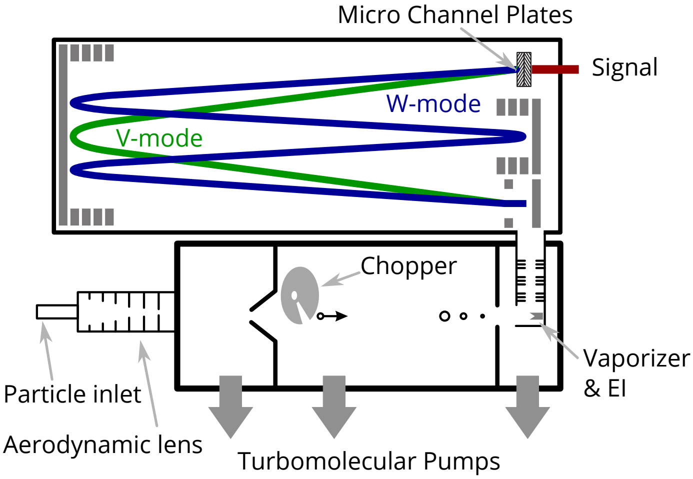

Figure 2.4.: Schematic drawing of the HR-ToF-AMS. The two available ion flight paths V-mode and W-mode are highlighted in green and blue, respectively. This graph is adapted from DeCarlo et al. (2006).

The instrument samples aerosol through a critical orifice. The diameter of the orifice is typically chosen in the range of 100 µm to 130 µm, depending on the intended use case. The critical orifice limits the flow into the instrument to approx. $100\,\mathrm{cm}^3/\mathrm{min}$. The aerosol then passes an aerodynamic lens consisting of a set of succeeding concentric orifices of varying diameter (Liu et al., 1995b,a; Zhang et al., 2004). Passing the aerodynamic lens, particles in the size range of 100 nm to 700 nm are focused on a narrow beam with a transmission efficiency greater than 50 % (Liu et al., 2007). For most diameters in this range the transmission efficiency is even 100 % (Liu et al., 2007).

After passing the aerodynamic lens, the aerosol enters a vacuum chamber with three pressure stages created by four turbomolecular pumps in conjunction with critical apertures. The region directly after the aerodynamic lens is called the aerosol sampling chamber and is maintained at $< 1 \times 10^{-1}$ Pa. By expansion into this vacuum, particles are accelerated to velocities depending on their vacuum aerodynamic diameter D_{va} (compare subsection 1.2.2). Smaller particles have high velocities after the expansion, whereas larger particles have lower velocities.

The following particle sizing chamber is kept at approx. 1×10^{-3} Pa and contains a rotating chopper which can be moved into the particle beam in order to modulate it. With the chopper in the particle beam at a defined frequency, particle packages with a common starting point and starting time but different velocities are created, which then continue moving towards the detection region. This mode is called particle time of flight mode (PToF). Alternatively, the particle beam path can be completely obstructed (chopper position "blocked") in order to block the particle beam and to measure the gaseous background, or completely unobstructed (chopper position "open") to let the particle beam pass. The difference between these two modes provides the so called MS-mode mass spectrum (MS).

In the particle detection chamber, the aerosol is impacted on a resistively heated tungsten surface (vaporizer), typically set to 600 °C. Compounds that have a lower boiling or decomposition temperature than the used temperature are evaporated and subsequently ionized by electron ionization (EI). The particle detection chamber is at a pressure of 1×10^{-4} Pa to 1×10^{-5} Pa. When arriving at the vaporizer, the particle concentration with respect to air is enhanced by approx. seven orders of magnitude, because the non-focused gaseous component of the aerosol is preferentially pumped away in the previous vacuum chambers.

The resulting fragment ions are directed into the mass spectrometer by electrostatic fields. The mass spectrometer is differentially pumped by a fifth turbomolecular pump. On their way, the ions are focused using a set of individually tunable electron lenses. A pulsed extraction into the mass spectrometer – orthogonal to the ion beam – sends the ions on a flight path to a detector, passing one or three times through dual-stage reflectron units. The ion flight path can be selected using various control voltages. The flight path for one reflectron pass looks similar to the letter V and is called V-Mode. The other mode makes use of a second installed reflectron and resembles the letter W, hence its name W-Mode. In W-Mode, the flight path is approximately doubled. As the ion time of flight is quadratically dependant on the mass to charge number ratio m/z of the ion, a longer flight path at the same data sampling rate results in a better resolution of the mass spectrometer. The disadvantage of prolonging the flight path is a reduced sensitivity due to a divergent ion beam and a reduced extraction frequency. Switching between V- and W-Mode is done after measurement periods in the order of minutes.

The core element of the mass spectrometers detector is a set of microchannel plates (MCP). It consists of two MCPs, their channels at an angle towards each other to prohibit the direct pass of an ion. Each of the microchannels acts as an electron multiplier, generating a measurable amount of electrons from each ion impacting the MCP set.

In the MS-mode of the instrument, mass spectra are acquired continuously at the extraction frequency and averaged to a user-set time resolution. The open and closed chopper positions are alternated in this mode. The averaged MS for the closed position contains a reduced gas-phase component and residual signal from slowly evaporating compounds on the vaporizer, whereas the averaged open MS additionally contains the particle information. The particulate mass spectrum can be calculated as the difference of both averaged MS.

When in PToF-Mode, the starting time for each particle package is known via an optosensor registering when the chopper is letting particles pass. To have a well-defined starting time, the chopper is only open 1 % of the time, effectively discarding 99 % of all sampled particles. The particles time of flight ends, when they impact the vaporizer. Because the entire process of ionization and acquisition of a mass spectrum can be considered fast compared to the flight times of particles in the particle sizing chamber, the acquisition of a mass spectrum can be interpreted as the end of the flight time. Typically, a set of 50 to 100 MS are acquired per particle package, leading to that number of size classes distinguishable by the instrument. The set of size-dependent MS is averaged over a user-defined time (typically 0.5 min to 5 min) to generate reliable data.

2.4.1. Quantification

The ion rate I measured by the AMS can be converted to a mass concentration C using Equation 2.1 (Jimenez et al., 2003b; Allan et al., 2003; Alfarra et al., 2004).

$$C = \frac{I \cdot MW}{N_A \cdot Q \cdot CE \cdot IE} \tag{2.1}$$

In this equation, MW is the molecular mass of the species yielding the respective ion, N_A is the Avogadro constant, Q is the volumetric flow rate into the instrument, CE is the collection efficiency and IE is the ionization efficiency.

The ionization efficiency is here defined as the ratio of ions detected to the number of parent molecules available in the ionization region of the instrument. For the AMS, this quantity is not only dependant on the efficiency of electron ionization, but also on the efficiency of ion transmission through the mass spectrometer.

The collection efficiency can be defined as the ratio between the number of particles introduced into the instrument and the number of particles being evaporated at the vaporizer. This quantity is often lower than unity because of several effects:

- Shape related losses: The aerodynamic lens does not focus non-spherical particles as good as spherical particles (Jayne et al., 2000; Alfarra et al., 2004)

- Particle bounce: Solid particles can reflect off the vaporizer before being completely evaporated (Canagaratna et al., 2007)
- Particle transmission: Particles with diameters outside the centre of the aerodynamic lens transmission function have a transmission efficiency below one (Zhang et al., 2004; Huffman et al., 2005; Liu et al., 2007)

Comparisons with other instruments like particle to liquid samplers (PILS) have shown that CE is only significantly greater than 0.5 when the aerosol is highly acidic, has a high ammonium nitrate mass fraction, or is embedded in air of high humidity (i. e. above 80 %). For ambient data, Middlebrook et al. (2012) developed a parametrization of CE based on these factors, which is applied to all data shown in this work. The uncertainty associated with the resulting CE is estimated to be 30 % (Middlebrook et al., 2012).

The measurement parameters in Equation 2.1 are calibrated for, as is the relationship between particle time of flight and D_{va} (see section 1.3). The calibration procedures are described in detail in subsection 2.4.2.

The raw data needs to be processed in several steps to make it accessible for interpretation. These steps are described in subsection 2.4.3.

2.4.2. Calibration procedures

2.4.2.1. Flow calibration

The AMS employs a pressure sensor after the critical orifice. The pressure measured here is linearly dependant on the flow through the orifice. For calibration purposes, the flow into the instrument can be reduced by means of a needle valve. Parameters for a linear equation which converts pressure into flow are obtained from recorded pressures and flows determined with a soap bubble flow meter.

The measured flow is, according to the manufacturer of the used flow meter, accurate to within 1 % (Sensidyne, LP).

2.4.2.2. Velocity calibration

As introduced in section 1.3, particles are accelerated by the expansion into the vacuum of the AMS chamber. Different velocities result, depending on the particles vacuum aerodynamic diameter D_{va}. The velocities can be calculated by measuring the particle time of flight (PToF) for the known distance between chopper and vaporizer. To characterize the relationship between particle velocity v_p and D_{va}, the empirical Equation 2.2 has been developed by Jayne et al. (2000) and modified by Allan et al. (2003).

$$v_p = \frac{L_c}{t_p} = v_l + \frac{v_g - v_l}{\left(\frac{D_{va}}{D^*}\right)^b} \tag{2.2}$$

Therein, L_c is the distance between chopper and vaporizer, v_l and v_g are the gas velocities inside and after the aerodynamic lens, respectively. D^* and b are calibration parameters.

In a velocity calibration, particles with known diameters and a narrow size distributions are introduced into the AMS. Polystyrene latex spheres (PSL) are normally used as calibration material. PSL are available in suspensions of monodisperse diameters between 50 nm and 600 nm, are spherical and have a known density of $1.05\,\mathrm{g/cm^3}$. As an alternative, monodisperse NH_4NO_3 aerosol of known size can be used, accounting for its bulk density and its Jayne shape factor (Jayne et al., 2000; Jimenez et al., 2003a; DeCarlo et al., 2004), a quantity correcting for the actual particle density and shape.

The parameters v_l, v_g, D^* and b in Equation 2.2 are then adjusted to best reproduce the data points of all calibration sizes.

2.4.2.3. Ionization efficiency calibration

As mentioned in section 2.4, the ionization efficiency IE can be understood as the ratio of detected ions to parent molecules available in the ionization region and depends on the efficiency of ionization as well as on the ion transmission efficiency through the mass spectrometer. Consequentially, IE is an important diagnostics for the instrument performance which is monitored regularly. Two approaches can yield IE values, namely the mass-based method and the single particle method. Both methods use monodisperse, dry NH_4NO_3 aerosol as calibration material. This aerosol is generated by size-selecting from a dried, polydisperse aerosol with a DMA. Particles with a defined mobility diameter and a single positive charge result from this method, along with a portion of particles with n charges and an about n times larger mobility diameter.

For the mass-based method, a CPC is sampling from the same aerosol generation setup as the AMS. Under these conditions, the aerosol mass concentration can be calculated from the CPC number concentration using the density of bulk NH_4NO_3, and the known particle diameter, assuming spherical particles. A linear regression of measured AMS mass concentration for a range of mass concentrations yields a correction factor for the assumed IE .

For the single particle method, the AMS is operated in the PToF mode and mass spectral responses for single particles are individually saved. Assuming a complete evaporation of particles on the vaporizer, the number of molecules per particle is calculated from particle density and volume and serves as number of ions available for ionization. The number of ions detected per particle can be calculated from the measured data. IE is given by the ratio between the two values.

The mass based method suffers from 10 % counting uncertainty of the used CPC (TSI, Inc., 2002) in addition to uncertainties originating from splitting the aerosol generator flow into two unequal flows. This uncertainty must be combined with the AMS signal uncertainty due to fluctuations of voltages and filament emission, uncertainties of the particle transmission efficiency, and uncertainties in the counting statistics. All together, the latter uncertainties are estimated to 10 % (Drewnick et al., 2005). Furthermore, accounting for multiply charged particles is difficult with this method.

The uncertainty of the single particle methods only originates from the aforementioned AMS uncertainties of 10 %. Multiply charged particles can easily be identified and disregarded with this method. The IE calibrations during the 2012 PEGASOS campaign have been performed with the single particle method.

2.4.2.4. Thresholding-related calibrations

The signal generated by ions impacting the MCP is logged by a thresholded 8-bit analog-to-digital converter (ADC) card operating at 1 GHz. The signal to noise ratio is drastically improved by the thresholding operation. The threshold for saving the data is set such that the electronic noise is crossing it only to a very minor fraction, whereas the signal generated by a single ion is guaranteed to cross it. The correct setting of the threshold is verified by the ratio of Argon to Nitrogen detected by the instrument, which is a known constant if ambient air is sampled. The abundance of nitrogen is high enough for multiple N_2^+ ions being detected in one MS extraction, meaning the threshold is always crossed by the nitrogen ion signal, even if the threshold is at a high level. Argon is so low in abundance, that no more than one Ar^+ ion is detected for one MS extraction. When the threshold is set too high, the Argon ion signal is classified as noise by the thresholding operation, leading to a measured Ar/N_2 lower than the actual value. A too high threshold setting would especially influence the measurement of organic aerosol, as the EI mass spectrum of organic molecules is spread out on many ions of abundance comparable to or lower than Ar^+.

Because the electronic noise is not logged during actual measurements due to the thresholding operation, the average of the noise has to be determined in a calibration. This average is mapped onto a known, integer number of the 256 channels of the ADC card. As the electronic noise can vary with temperature and other external influences, this calibration, also known as baseline reset, is performed regularly. New data acquisition software versions allow for an automated baseline reset in a user-defined interval. During the 2012 PEGASOS campaign, the baseline was reset immediately before the flights, also on refuelling stops.

The magnitude of the signal generated by one ion is determined by averaging over many ions of low abundance, to minimize the possibility of detecting two ions at once. At this stage, the signal is quantified as an area under the signal in bits as function of the acquisition time in ns, and is consequentially termed single ion area. Using this single ion area, signals can be expressed as multiples of ions detected per second.

2.4.3. Mass spectra interpretation

Mass spectra acquired by the AMS are highly fragmented. This is mainly originating in the hard EI method using 70 eV, but is enhanced by the vaporization of particles at 600 °C. Inorganic species like nitrate or sulfate as well as major ambient air constituents generally result in only a few fragments, whereas organic molecules yield a large number of fragments. When measuring ambient aerosol, many different compounds contribute to the organic part of the aerosol. The combination of a large number of compounds and a high degree of fragmentation leads to organic fragments being present on most m/z ratios acquired by the mass spectrometer. Typically, several fragments can be found on one m/z, also interfering with inorganic and air ions.

2.4.3.1. m/z calibration

Before the data evaluation starts, the m/z scale is adjusted for the whole set of measured mass spectra. The presence of background ions allows for a refinement of the parameters of the quadratic relationship between ion time of flight and m/z ratio for each saved mass spectrum. For this purpose, the time of flight of suitable ions with known mass and no obvious interference is selected for fitting a quadratic polynomial function. The exact ion time of flight is determined as the centre of a Gauss curve fitted to the ion signal peak.

2.4.3.2. Baseline subtraction

Very high signals created in the instrument e.g. by the N_2^+ ion can create erroneous signal after the decline of the ion signal, reaching out well into the next integer m/z ratio. This is illustrated in Figure 2.5.

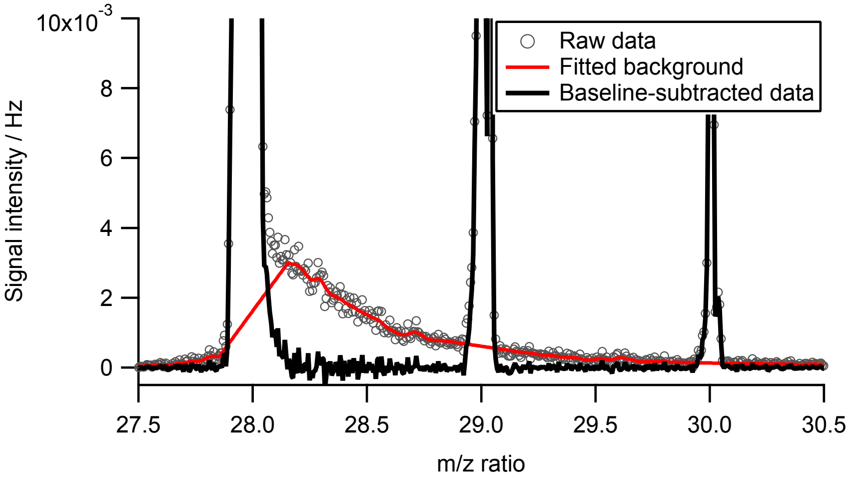

Figure 2.5.: Erroneous signal after a multi-ion event on m/z 28 $\left(N_2^+\right)$. The red line shows a peak baseline, constructed by linear interpolation between regions left and right of the peak region. The black line shows the baseline-subtracted raw data.

To correct for this behaviour, a peak baseline is generated by linear interpolation between regions left and right of all integer m/z ratios. This baseline is then subtracted from the raw data. In the given example, the difference in peak area created by this operation is minor because the peak following the N_2^+ ion signal is relatively big itself, but when small peaks directly follow big peaks, the baseline subtraction is crucial in obtaining correct data.

2.4.3.3. High resolution analysis

To quantify individual ions, the measured signal around every integer m/z is approximated by a peak shape function located at the exact m/z of selected ions. The peak shape function grows wider with rising m/z because of the quadratic relationship between the ion time of flight sampled at constant intervals and the m/z. The m/z dependence of the peak shape function width is quantified using a selection of reference ions similar to the m/z calibration described in subsubsection 2.4.3.1.

Because of the natural velocity distribution of ions, imperfections in the electric fields inside the mass spectrometer, and other effects, the ion peak shape function is not Gaussian. The earlier determined relation between peak width and m/z is used to gather normalized and averaged peak data of all selected ions for all selected mass spectra. The peak shape is then determined as a smoothed average of all data points. Optionally, the data points of one side of an ion peak can be omitted, allowing to discard interferences from other ions while still making use of the unaffected side of the peak. Figure 2.6 shows an example of a dataset for one flight day. In this example, the left sides of $C_4H_2^+$ and CH^+ have been omitted.

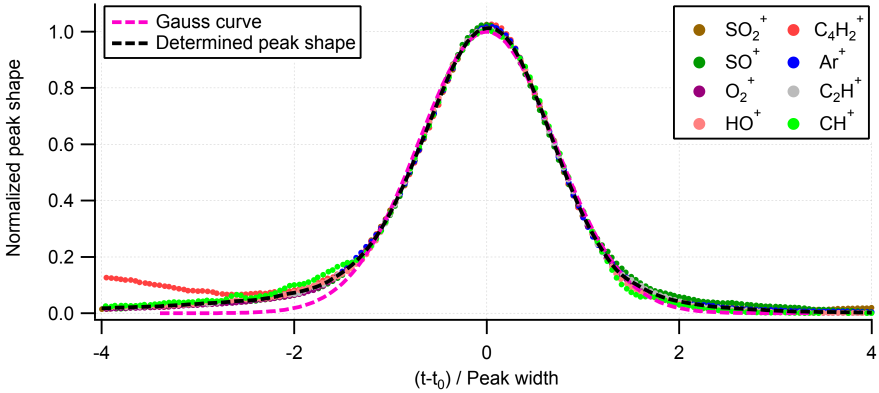

Figure 2.6.: Example of a dataset used for determining the peak shape to be used for high-resolution analysis. Selected ions are scaled to their signal intensity and peak width, the peak shape is determined from their average. Note, that for $C_4H_2^+$ and CH^+, values left of the peak centre have been ignored due to interference from other ions.

The determined peak shape is used for further analysis. Each ion that has been selected to be fit is represented by the peak shape function with fixed position, calculated width according to the peak position, but variable intensity. The intensities are adjusted, so that the combination of ion peak shapes best reproduces the measured signal. As a result, contributions of individual ions to a single integer m/z are obtained.

2.4.3.4. Relative ionization efficiencies

Directly applying Equation 2.1 (see page 25) to acquired AMS data would require knowing the parent species and its molecular mass for every measured ion. Also, ionization efficiency calibrations would be needed for all species. While this could be feasible for inorganic species, it is infeasible for the vast amount of organic compounds present in ambient particles. However, laboratory studies have demonstrated distinct linear relationships between IE and molecular mass for inorganic and organic species (Alfarra et al., 2004; Canagaratna et al., 2007), leading to the suggestion that the ratio between IE and molecular mass MW of a molecule can be expressed as a multiple of this ratio for a reference substance like nitrate:

$$\frac{IE}{MW} = RIE \cdot \frac{IE_{NO_3}}{MW_{NO_3}} \tag{2.3}$$

Where the factor RIE is the relative ionization efficiency. Inserting Equation 2.3 into Equation 2.1 yields Equation 2.4 for each species i.

$$C_i = \frac{I \cdot MW_{NO_3}}{N_A \cdot Q \cdot CE \cdot RIE_i \cdot IE_{NO_3}} \tag{2.4}$$

In Equation 2.4, RIE has to be specified on a per-species basis. This allows for the calibration of the AMS with only nitrate, provided that the RIE_i for all species i of interest are known. Table 2.3 shows commonly used values for the routinely measured AMS species.

Table 2.3.: Summary of RIE values commonly used for field data. See text for details.

Species	RIE
Organics	1.4
Nitrate	1.1
Ammonium	3.5 – 6
Sulfate	1.2
Chloride	1.3

For IE calibrations, only NO^+ and NO_2^+ signals are considered for quantification. These ions account for approximately 90 % of the total nitrate signal only, so the RIE of nitrate is set to 1.1 to compensate this.

Ammonium RIE values are higher than 1, probably because of higher sensitivity of the detector to ions of low m/z and/or because of a more efficient extraction of these ions into the mass spectrometer (Canagaratna et al., 2007). The exact value can vary with instrument performance and is determined during standard IE calibrations.

The RIE values are estimated to be accurate within 20 % for organics, 10 % for ammonium, and 15 % for sulfate.

2.4.3.5. Fragmentation table

With the used HR-ToF-AMS, most ions can be separated and individually quantified, but this approach is impossible for separating identical ions of separate origins. The most prominent example of this is the H_2O^+ ion, which can emerge from humidity in the sample air, particulate water, fragmentation of sulfuric acid, and from fragmentation of organic molecules. Another example is the CO_2^+ ion, which can be generated from CO_2 in the sampling air as well as from organic fragmentation. In these cases, additional information must be used to separate the total ion signal into the individual contributions. For this a so called fragmentation table was introduced by Allan et al. (2004). To confine some entries in the fragmentation table, measurements were performed with a High Efficiency Particulate Airfilter (HEPA-Filter) in the inlet line. These filter measurements were recorded at least before and after, sometimes also during the flights.

For H_2O^+, the contribution of particulate water is expressed as the total amount of H_2O^+ minus the contributions from humidity, sulfate, and organics. The humidity contribution can, for constant humidities, be derived as a constant fraction of the N_2^+ ion signal from measurements with a particle filter in the inlet line. When the humidity changes, time-dependant external data with measured humidities can be used. The contribution from sulfate is estimated via known fragmentation patterns of sulfate and the signal intensities of the SO^+ and SO_2^+ ions (Allan et al., 2004). The organic contribution is derived from laboratory observations and scaled to the organic contribution to the CO_2^+ ion (Aiken et al., 2008). The organic contribution to the CO_2^+ ion is in turn determined by fixing the gas-phase CO_2 contribution to this ion to a fraction of the N_2^+ ion signal, the exact fraction determined by examining particle-free filter measurements. These and other relations are also propagated to isotopes of affected ions.

2.4.3.6. Elemental analysis

Identified and quantified ions can be used to gather information about the elemental composition of the organic fraction of measured aerosol. The high resolution of the AMS employed in this work makes the identification of the sum formula of almost all $C_xH_yO_z$ fragments possible from their precise m/z. Once the elemental composition of each ion k is known, the elemental ratios for the whole organic mass is calculated. Weighting the mass fraction $F_{i,k}$ of element i in each ion k with the signal intensity I_k generated by the respective ion and summing for all n ions results in a mass concentration M_i relative to the entire organic mass spectrum (Aiken et al., 2007).

$$M_i = \sum_{k=1}^{n} I_k \cdot F_{i,k} \tag{2.5}$$

The relative mass concentration M_i is converted to a relative atomic fraction N_i by dividing by the elements mass MW_i.

$$N_i = \frac{M_i}{MW_i} \tag{2.6}$$

The relative atomic fractions of the elements are then used to calculate atomic ratios, e.g.

$$O/C = \frac{N_O}{N_C} \tag{2.7}$$

$$H/C = \frac{N_H}{N_C} \tag{2.8}$$

The elemental ratios obtained in this way were validated by Aiken et al. (2007) and Aiken et al. (2008), using various standards in the laboratory. The comparison yielded a linear relationship between measured and real elemental ratios, albeit with a correction factor α of 0.75 for O/C and 0.91 for H/C. These correction factors have been taken into account in this work.

Kroll et al. (2011) established the averaged carbon oxidation state $\overline{OS_C}$ as a metric for describing the chemistry of atmospheric aerosol. The $\overline{OS_C}$ value can be approximated from AMS elemental ratios by Equation 2.9, under the assumption of negligible nitrogen content and negligible peroxides.

$$\overline{OS_C} \approx 2 \cdot O/C - H/C \tag{2.9}$$

$\overline{OS_C}$ theoretically ranges from -4 for the most reduced organic compound methane $\left(CH_4\right)$ to $+4$ for the most oxidised organic compound carbon dioxide $\left(CO_2\right)$. Ambient observations typically show values in the range of -1.6 to $+0.6$ (Kroll et al., 2011).

2.5. Adaptation of the Aerosol Mass Spectrometer to Zeppelin requirements

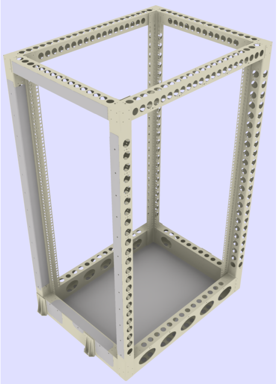

Figure 2.7.: 3D CAD drawing of a 19 inch Rack for mounting instruments, developed by Zeppelin Luftschifftechnik GmbH.

For operating on a Zeppelin, an instrument has to fulfil several requirements. It should be as light as possible, so reachable altitude and flight endurance are affected as little as possible (see section 2.2 for details). Also, it has to be mounted to fixation points already present in the Zeppelin. The mounting has to be in conformity with regulations for aircraft security, specifically the entire setup has to be able to withstand an emergency landing scenario mechanically intact. Aircraft security regulations also dictate measures for fire prevention.

To realize these requirements Zeppelin Luftschifftechnik GmbH has developed a light rack which is mountable to the seat rail inside the Zeppelin and can support up to 150 kg without deforming in the emergency landing scenario. It is compatible to 19 inch modules commonly used for electronics and parts of scientific instruments. Aluminium sheets close off the sides of the rack, making the rack a fire containment unit. A Halon fire extinguisher is mounted to a corner post of the rack. An opening placed in a front panel allows to quickly extinguish any fire arising inside the rack. These measures ease the use of standard (not necessarily fireproof) materials within the rack.

The AMS used in this study was mounted in a Zeppelin rack like shown in Figure 2.7. The details of this process are described in the following subsection.

2.5.1. Mounting in a 19 inch Rack

To ensure conformity with an emergency landing scenario, the entire setup needs to be able to withstand a deceleration of 29.4 $\mathrm{m/s^2}$ in downwards direction and flight direction, as well as a deceleration of 9.8 $\mathrm{m/s^2}$ in upwards direction and all horizontal directions. For certification of this ability, a statical calculation has to show enough reserves towards the used materials failure limits, generally dependant on the materials tensile strength. The statical calculation requires all objects in the rack to have known material properties proven by an inspection certificate. If this is not possible for an object, it has to have form closure to objects with proven properties in all directions.

The core parts of the AMS, the PToF chamber and the mass spectrometer, were not available with valid inspection certificates. Also, the complex geometry of these parts made it highly impractical to achieve form closure in all directions. To prove the tensile strength of the PToF chamber and the mass spectrometer, a new procedure was established. As a first step, a material probe of both parts was chemically dissolved and analysed with inductively coupled atom emission spectroscopy. With the resulting elemental composition, the PToF chamber alloy could be identified as EN AW 7075, the mass spectrometer alloy as EN AW 6060. Because different heat treatments of the same aluminium alloy can have drastically different tensile strengths (Horn, 1967), this information alone is not sufficient. In Horn (1967), it is shown that there is a linear relationship between tensile strength and hardness of aluminium alloys (Figure 2.8). This relationship was used in the second step.

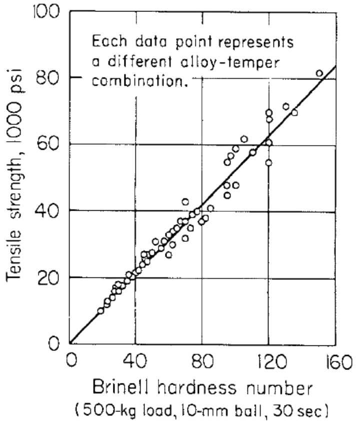

Figure 2.8.: Tensile strength versus hardness of aluminium alloys. Figure from Horn (1967).

The hardness of the parts was determined with the Vickers hardness test. In this test, a diamond of square-based pyramid shape is pressed into the material with a defined force. The applied force is divided by the surface area of the resulting indentation to give the Vickers hardness number. The resulting values were converted to Brinell hardness numbers according to EN ISO 18265. Tabulated hardness values allowed to identify the heat treatment of the PToF chamber as T651 with a tensile strength of 572 MPa and the heat treatment of the mass spectrometer as T66 with a tensile strength of 215 MPa.

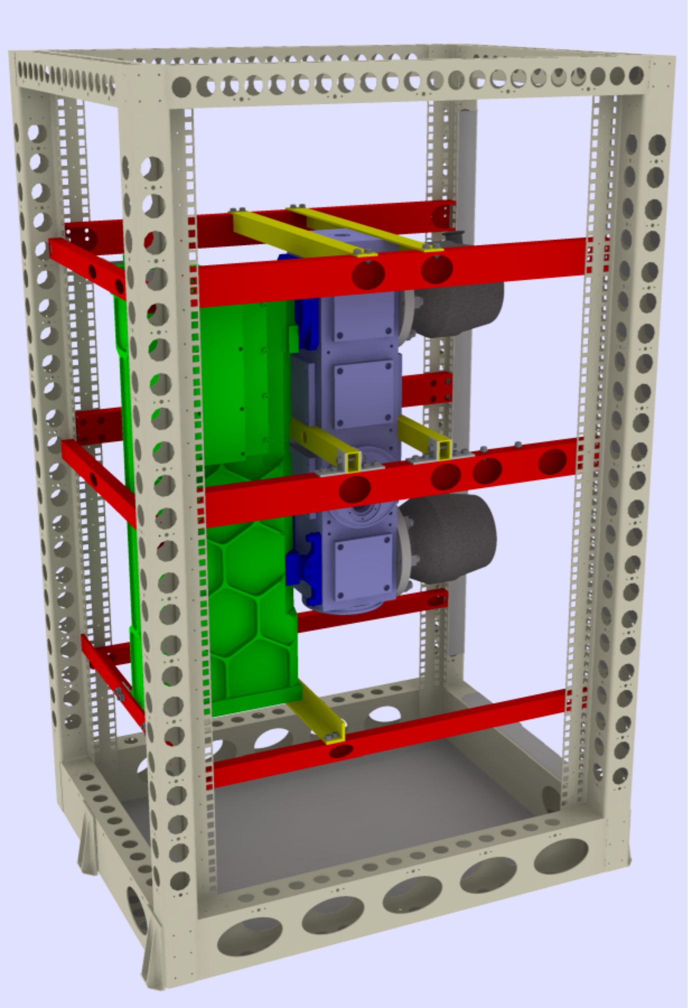

Figure 2.9.: 3D CAD drawing of the AMS core parts mounted in a 19 inch rack. The mass spectrometer is shown in green, the PToF chamber in light blue. Aluminium bars connected to the rack are shown in red, aluminium bars resting on these are coloured yellow. The parts connecting mass spectrometer and PToF chamber are shown in dark blue.

In commercial AMS systems, the instruments core parts are mounted horizontally. To fit into the rack used in the Zeppelin, the instrument developed in this work was mounted vertically, the instruments inlet pointing downwards. This arrangement is shown in Figure 2.9. In this figure, the mass spectrometer is coloured green and the PToF chamber light blue. Aluminium bars mounted to the rack are shown in red, aluminium bars resting on these are coloured yellow. The parts connecting PToF chamber and mass spectrometer are shown in dark blue. In downwards direction, the mass spectrometer is held by aluminium angles, one resting on a set of bars fixed to the rack, one directly fixed to the rack. Two aluminium bars are screwed to the PToF chamber, suspending its mass on bars fixed to the rack. These bars also provide a form closure in flight direction (left side of the graph) and against flight direction (right side of the graph). A set of aluminium angles resting on aluminium bars fixed to the rack is screwed to the top of the PToF chamber (screws not shown in Figure 2.9), also carrying its mass and providing form closure. In flight direction, the mass spectrometer is additionally held by two more aluminium bars equipped with stopping angles to the sides of the mass spectrometer, providing form closure in flight direction and to the sides. A statics calculation performed by ZLT validated the capability of this setup to withstand the emergency landing scenario.

2.5.2. Technical changes

2.5.2.1. Turbomolecular pumps

The turbomolecular pumps maintaining the vacuum in both PToF chamber and mass spectrometer are usually fixed to the instrument using four clamps and M 8 screws into threaded blind holes. A schematic cut through pump, clamp, and vacuum chamber is fixed is shown in Fig. 2.10a.

The pumps used in AMS systems are the Varian TV301 Navigator (250 l/s, 4 kg) and the Varian Turbo-V 81-M (77 l/s, 2 kg). These pumps can reach rotation speeds of over 80 000 min^{-1}. In case of sudden rotor blocking, a very high torque around the rotational axis can occur. To prevent the pump from tearing loose in such a scenario, it needs to be mounted correctly. The pump manuals do only specify that torques of 250 Nm and 1000 Nm, respectively, are required to be endurable. Upon request at the manufacturer, a manual amendment was issued, specifying that the lighter variant of the turbomolecular pump can indeed be fixed by four clamps and M 8 screws. The heavier variant of the pump has to be fixed with eight clamps and M 8 screws. The two heavier pumps used in the AMS are fixed to the PToF chamber, with not enough material around the pump for four more clamps. As a

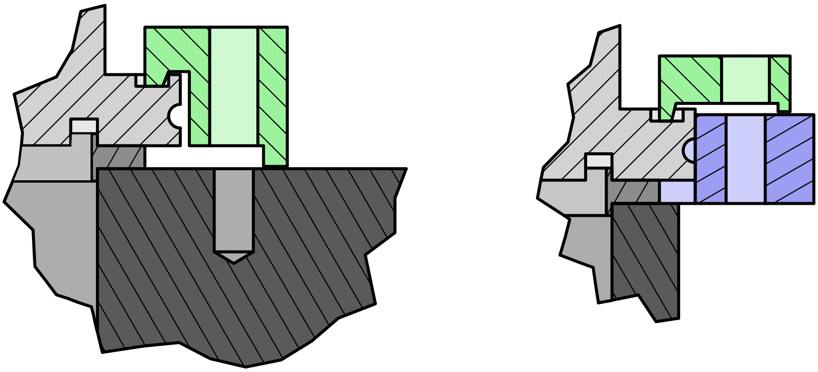
(a) (b)

Figure 2.10.: Schematic cut through AMS pump fixations. Fig. 2.10a shows the standard fixation, Fig. 2.10b a newly constructed setup. The pump is shown in light grey, a centring ring with seal in medium grey, the vacuum chamber in dark grey, and a clamp in light green. For the standards fixation, a screw (not shown) presses the clamp to the vacuum chamber, also pressing the pump down. For the new setup, a screw (not shown) presses the clamp to a ring around the pump (shown in light blue), also pressing the pump down. The ring is pressed to the vacuum chamber in other places, not shown here.

solution, a ring to place around the pump was constructed. This ring provides, together with redesigned clamps, more fixation points (illustrated in Fig. 2.10b).

Four screws are going through clamps and the ring into threaded blind holes in the PToF chamber, another four screws are fixing additional clamps to the ring. Compared to the original mounting, this setup does not offer increased resistance to shearing because the same four screws attach the pump to the chamber. However, using the material strength of the used screws, the force required to shear off a screw can be estimated to be an order of magnitude larger than the force acting on it, based on the torque mentioned in the manual and the screws distance to the rotational axis. The four added clamps instead increase the friction on the pump flange, ensuring the pump does not turn in the case of catastrophic failure. The new setup is shown in Figure 2.11.

2.5.2.2. Mass spectrometer

Upon request, the vacuum chamber of the mass analyzer was redesigned by Tofwerk AG, Thun, Switzerland in cooperation with Fachhochschule Nordwest-

Figure 2.11.: Photograph of a Varian TV301 Navigator turbomolecular pump and its mounting on the AMS PToF chamber. A ring around the base of the pump holds eight clamps pressing the pump down, of which four are fixed to the PToF chamber, the other four are fixed to the ring itself.

schweiz (FHNW) to reduce the total mass by 5 kg (40 %) compared to the regular mass analyzer, while maintaining the necessary stability for evacuation to high vacuum. Furthermore, Tofwerk AG reduced the depth of the 19 inch module containing the mass spectrometers power supply, enabling its placement within the space inside the rack that is not occupied by the AMS core parts.

2.5.2.3. Data acquisition

The AMS data acquisition operates with two analog-to-digital PCI cards and a timer PCI card. These cards are normally housed in a 19 inch mountable computer. The mass and size of this computer, together with the additionally required keyboard and monitor, make it infeasible for usage on the Zeppelin. As an alternative, a laptop computer was employed. The data acquisition cards were placed in an expansion board, which was connected to the laptop via its ExpressCard slot. A lightweight box made out of 1 mm thick aluminium sheet was constructed around the expansion board. The laptop was placed on top of the rack, making interaction with the instrument with closed off side walls possible. The data acquisition system has a total mass of 5.5 kg, making more than 75 % lighter than the standard system with 24.7 kg.

2.5.2.4. Valve control

The inlet line of the AMS can be closed off with a ball valve just after the critical orifice. For maintaining the a vacuum without running turbomolecular pumps, the forepump can be closed off with another valve. Both valves are not accessible from outside the rack with the side walls attached. To switch the valves without removing the side walls, the forepump valve was replaced by a solenoid valve and the inlet valve was replaced by a servo and gear driven variant. These electronic valves are controlled with switches on the rack front panel. The switch positions are processed by a microcontroller system developed by Aerodyne, Inc., sending appropriate signals to the valves. It is of high importance to maintain as high as possible vacuum in case of power failure to ease the automatic turning on of the turbomolecular pumps on reconnection to power, as well as to impair the instrument performance after restart as little as possible. Therefore, the system was adapted to Zeppelin requirements by generating a diagnostics voltage from the regular power supply and adding supercapacitors as energy storage. If a power failure occurs, the diagnostics voltage drops to zero, triggering the microcontroller to close the inlet valve, power for both microcontroller and closing operation coming from the supercapacitors.

2.5.3. Changes of measurement technology

2.5.3.1. Pressure controlled inlet

The performance of the aerodynamic lens and the relation between flow into the instrument and pressure inside the lens depend on ambient pressure. For measurements that are expected to experience a wide range of ambient pressures like airborne studies, this provides a problem. While the flow could be corrected for with ambient pressure data, the particle velocity parameters used to determine particle d_{va} would have to be determined as a function of pressure. Although Crosier et al. (2007) successfully included a first order pressure dependence in the respective calibration equation, this method requires a vastly increased calibration effort and does not take changing cut-off size due to pressure change into account.

Alternatively, Bahreini et al. (2008) described a pressure controlled inlet setup that overcomes these problems. In this setup, a second critical orifice is placed in the sampling line. The resulting volume between the two critical orifices is then evacuated by a pump with variable flow, to keep the pressure inside the volume constant, regardless of ambient pressure. This results in constant sampling conditions for the instrument.

For the AMS used in this work, the setup of Bahreini et al. (2008) was adapted. In detail, the pump flow was regulated by an adjustable electronic valve, which was regulated by a microcontroller. The microcontroller read the pressure inside the aerodynamic lens, which is proportional to the pressure between the critical orifices, and used a configurable proportional-integral-derivative algorithm to act on the valve, keeping the lens pressure constant.

The pressure in the volume between the critical orifices was set to 800 hPa, significantly lower than expected ambient pressure and therefore maintainable throughout all flight situations.

2.5.3.2. Omitted pump

To reduce the total mass of the Instrument, one of the usually three Varian Turbo-V 81-M turbomolecular pumps was omitted. Following along the particle beam, this pump is located after the chopper in the regular setup. By removing an orifice, the bigger TV301 Navigator pump located in the ionization region now takes over the gas load. A possible consequence of this change would have been a higher gas background leading to higher signal to noise ratios and therefore higher detection limits, which was not observed (see Table 2.5).

2.6. Performance of the new instrument

In comparison to the commercial instrument, the total mass of the AMS was reduced by 20 % to 134.5 kg. By integration into the 19 inch rack, the instrument occupies 25 % less space and has a 25 % reduced footprint. Effects of the adaptation on the measurement performance will be analysed in the subsections below.

2.6.1. Detection limits, precision, accuracy

Based on Equation 2.4 and the accuracies associated with its parameters, the total uncertainty of AMS mass quantification can be calculated by means of uncertainty propagation.

$$C = \frac{I \cdot MW_{NO_3}}{N_A \cdot Q \cdot CE \cdot RIE \cdot IE_{NO_3}} \qquad \text{(Equation 2.4)}$$

Assuming that I, MW_{NO_3}, and N_A are known precisely, the error in C can be expressed as

$$\frac{\delta C}{|C|} = \sqrt{\left(\frac{\delta Q}{Q}\right)^2 + \left(\frac{\delta CE}{CE}\right)^2 + \left(\frac{\delta RIE}{RIE}\right)^2 + \left(\frac{\delta IE_{NO_3}}{IE_{NO_3}}\right)^2} \qquad (2.10)$$

Using the common uncertainties for Q, CE, and IE_{NO_3} introduced in section 2.4 and the respective RIE uncertainties from subsubsection 2.4.3.4, the mass concentration uncertainties for the different species can be calculated (results summarized in Table 2.4).

Table 2.4.: Uncertainties associated with aerosol chemical species measured with the AMS.

Species	Relative uncertainty
Organics	37 %
Nitrate	33 %
Ammonium	33 %
Sulfate	35 %

An average of the standard deviation of blank measurements (performed by measuring with a HEPA filter in the inlet line) multiplied by a factor of three has been used to determine the precision of mass concentrations. Found values are tabulated in Table 2.5 below.

Table 2.5.: Average 3σ detection limits for the 2012 PEGASOS campaign.

Species	Detection limit (3σ)
Organics	$0.26\,\mu g/m^3$
Nitrate	$0.02\,\mu g/m^3$
Ammonium	$0.01\,\mu g/m^3$
Sulfate	$0.03\,\mu g/m^3$

2.6.2. Resolution

The International Union of Pure and Applied Chemistry defines the mass spectrometric resolution R as

$$R = \frac{m}{\Delta m} \tag{2.11}$$

Where m is the mass of the ion creating a signal and Δm the width of the peak at a defined height (Todd, 1991). Here, the full width of the peak at half height is used as Δm. The resolution of the mass spectrometer used in this work was determined using the ions N^+, O^+, OH^+, H_2O^+, O_2^+, Ar^+, and CO_2^+. At their position in the mass spectrum, Gaussian functions were fitted to the signal. The Gaussian function width at half height was used as Δm. As Figure 2.12 shows for 20 June, the resulting resolution was around 3050 for the instruments V-Mode and around 3900 for the instruments W-Mode. Data from other days (not shown) has similar resolution.

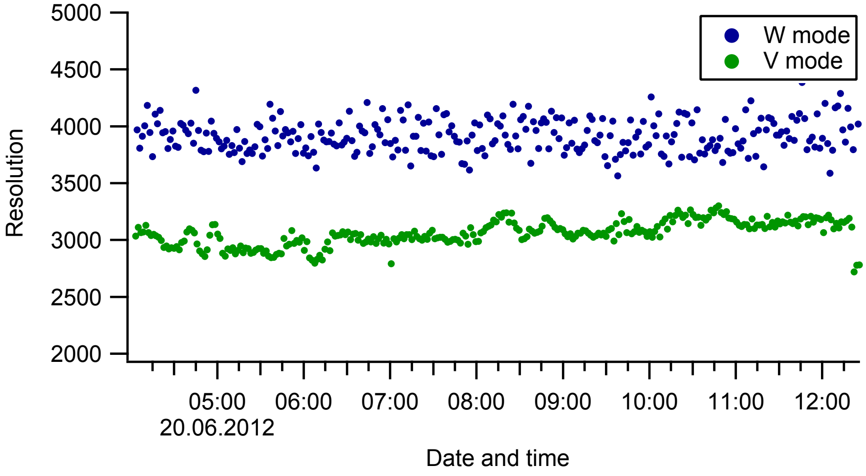

Figure 2.12.: Time series of V-Mode and W-Mode resolution on 20 June. The resolution was determined as an average of Gauss-fitted ion signal resolutions, using the width of the Gauss fits at half their height.

Due to the excellent resolution in V-Mode (regular AMS V-Mode resolution as advertised by Aerodyne, Inc. is around 2000) and the much lower sensitivity of the W-Mode (see section 1.3), the data analysis performed in this work relies on the V-Mode data.

2.6.3. Adaptation to changing pressures

The pressure controlled inlet described in subsubsection 2.5.3.1 proved to be reliable. A relatively slow response was chosen, in order to not introduce under- or overcorrection induced fluctuations in the lens pressure. With these settings, the lens pressure was stable with a standard deviation of below 0.4 % around the average on typical height profiling flight. Figure 2.13 shows the time series of lens pressure and ambient pressure in a two hour period of such height profiling. An ambient pressure change of $\sim$ 8 % within 5 min due to Zeppelin altitude change results in a temporary lens pressure change of $\sim$ 1 % due to the chosen slow response of the pressure controller.

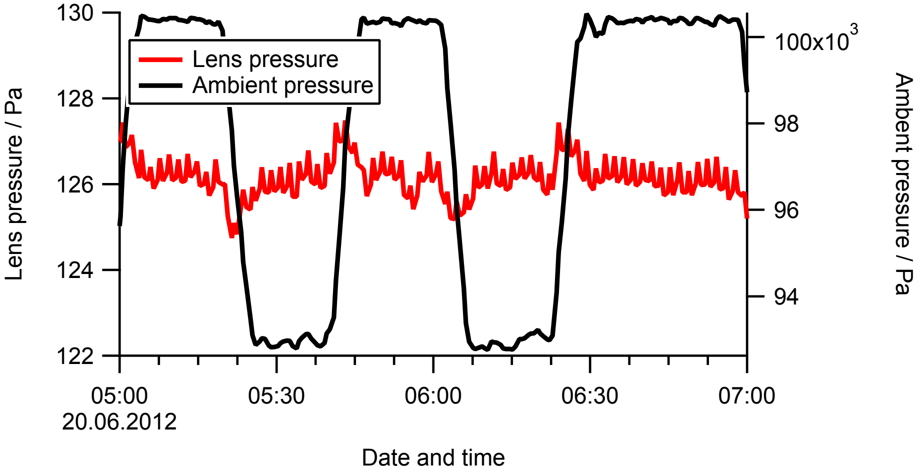

Figure 2.13.: Time series of the ambient pressure and the lens pressure for a typical height profiling flight. An ambient pressure change of $\sim$ 8 % within 5 min results in a temporary lens pressure change of $\sim$ 1 %.

2.7. Aerosol hygroscopicity

In section 4.3, the particle composition will be used to estimate the hygroscopicity of the particles and their CCN activity. The basis for these estimations is a theory established by Köhler (1936). It describes the relation between droplets of aqueous solutions and the gas phase surrounding them. The Köhler equation combines Raoult's law and the Kelvin effect and relates the water saturation ratio S with the diameter D_p of an aqueous droplet. The water saturation ratio is the ratio between water vapour pressure and water saturation vapour pressure at the same temperature and pressure conditions. The water activity a_w in the solution, the partial molar volume of water, and surface tension are parameters of the Köhler equation, as well as the universal gas constant R and the temperature T. Because water partial molar volume, surface tension and a_w are not known when probing atmospheric particles, assumptions and approximations have to be made for these parameters. Typically, the surface tension of the solution is assumed to be equal to that of pure water ($\sigma_w = 0.072\,\mathrm{N/m}$ at 298.15 K). This assumption is valid as long as there are no surfactants present in the particles of interest and they can be described as diluted solutions, e. g. at water saturation ratios near CCN activation. Furthermore, ideality is assumed, in this case volume additivity, enabling to express the partial molar volume of water as the ratio of molar mass M_w and density ρ_w of pure water. Applying these assumptions, the Köhler equation can be written as

$$S = a_w \cdot \exp\left(\frac{4M_w\sigma_w}{RT\rho_w D_p}\right) \tag{2.12}$$

Petters and Kreidenweis (2007) parametrized the water activity with the hygroscopicity parameter κ as

$$a_w = \left(1 + \kappa \cdot \frac{V_s}{V_w}\right)^{-1} \tag{2.13}$$

In Equation 2.13, V_s is the volume of solute, V_w the volume of water. Assuming that the considered particle is spherical, V_s and V_w can be expressed by D_p and the dry particle diameter D_{dry} (no water, exclusively solute):

$$a_w = \left(1 + \kappa \cdot \frac{D_{dry}^3}{D_p^3 - D_{dry}^3}\right)^{-1} \tag{2.14}$$

With Equation 2.14, Equation 2.12 can be rewritten as

$$S = \left(1 + \kappa \cdot \frac{D_{dry}^3}{D_p^3 - D_{dry}^3}\right)^{-1} \cdot \exp\left(\frac{4M_w\sigma_w}{RT\rho_w D_p}\right) \tag{2.15}$$

$$\ln(S) = \frac{4M_w\sigma_w}{RT\rho_w D_p} - \ln\left(1 + \kappa \cdot \frac{D_{dry}^3}{D_p^3 - D_{dry}^3}\right) \tag{2.16}$$

As typical values for κ of atmospheric particles are between 0.1 and 0.9 (Petters and Kreidenweis, 2007) and D_p^3 is typically much bigger than D_{dry}^3, the logarithmic term on the right side of Equation 2.16 can be well approximated by a Taylor series expansion terminated after the linear term. $D_p^3 \gg D_{dry}^3$ makes it possible to omit the D_{dry}^3 in the denominator of the logarithmic term, yielding Equation 2.17.

$$\begin{aligned} A &= \frac{4M_w\sigma_w}{RT\rho_w} \\ B &= \kappa \cdot D_{dry}^3 \\ \ln(S) &= \frac{A}{D_p} - \frac{B}{D_p^3} \end{aligned} \tag{2.17}$$

This equation shows a maximum at a critical $D_p = D_{crit}$ with $S = S_{crit}$, indicating that once S_{crit} is reached, the particle in question is activated and can grow dynamically. Due to the Kelvin term in the Köhler equation, S_{crit} is larger than 1. The term $(S - 1) \cdot 100\,\%$ is called supersaturation ss, and $(S_{crit} - 1) \cdot 100\,\%$ the critical supersaturation ss_{crit}. For cloud formation, it is relevant to know whether a particle of a given dry size can reach this activation point at atmospheric ss and grow into a cloud droplet. An analytical expression for D_{crit} can be found as a root of the derivative of S with respect to D_p.

$$D_{crit} = \sqrt{\frac{3B}{A}} \tag{2.18}$$

Inserting Equation 2.18 in Equation 2.17 yields

$$\ln(S_{crit}) = \frac{2}{3} \cdot \sqrt{\frac{A^3}{3B}} \tag{2.19}$$

Inserting A and B and solving for D_{dry} results in the critical dry diameter D_{crit}

$$D_{crit} = \frac{4 \cdot \sqrt[3]{4} \cdot M_w\sigma_w}{3 \cdot RT\rho_w \cdot \sqrt[3]{\kappa} \cdot (\ln(S_{crit}))^{\frac{2}{3}}} \tag{2.20}$$

For any given S and κ, D_{crit} is the minimal dry particle size necessary to reach the activation point. In combination with size distribution and particle number concentration information, it is possible to calculate the activated fraction a_f at S

from Equation 2.20. Herein, a_f is defined as the ratio of particles that are activated at a given S to all particles. For the purpose of this work, $S = 1.01$, i. e. $ss = 1\,\%$ has been used for these calculations, as this is a value typically reached in cumulus clouds (Politovich and Cooper, 1988).

Following Petters and Kreidenweis (2007), κ for a multicomponent aerosol can be calculated as a sum of pure aerosol component κ values, weighted by their respective volume fractions. This mixing rule is valid under the assumption that the aerosol particle composition is identical for all particle sizes, the aerosol composition is uniform for all particles of a given size (internally mixed) and the aerosol behaves ideally with respect to mixing of aerosol components.

3. Observations

The flights during the 2012 PEGASOS campaign can be categorized into transfer flights, height profiling flights and transect flights. Transfer flights will not be described in more detail here, as they have not been performed with the SOA package CL5. Height profiling flights are described in detail in section 3.1, transect flights in section 3.2.

The background of all flight track maps in this chapter corresponds to elevation data taken from publicly available Shuttle Radar Topography Mission (SRTM, Jarvis et al., 2008) data.

3.1. Height profiling

To explore the vertical variability of the lower atmosphere, the Zeppelin flew in different altitudes at the same geographical location. As a result, vertical profiles of the measured species were observed.

Height profiles were generally acquired by flying the airship in circles over a point of interest at two or three altitudes. These altitudes were maintained for at least 10 min to 15 min to allow all instruments to acquire a reasonable amount of data points. For the AMS, this usually meant 5 to 10 full cycles per altitude. The altitude changes where performed with typical ascend or descend rates of 3 m/s.

Usually, the lowest altitude was equal to the lowest flight altitude allowed by flight regulations. Depending on the exact location and obtained permissions, the actually used lowest altitudes varied between 80 m and 150 m. The highest used altitude was usually chosen as the highest level that was expected to be maintainable throughout the day (compare section 2.2), resulting in 400 m to 750 m.

The diameter of the flown circle was chosen to minimize perturbation of the measurements by Zeppelin exhaust gases while keeping the influence of local variability as small as possible. The resulting diameters were between 1000 m and 2000 m. As the pilots flew by sight and were also restricted by airspace regulations, the flown patterns were no real circles, but somewhat distorted.

3.1.1. Rotterdam: 2012-05-21, Flight No. 11

On 21 May, flight 11 was conducted from Rotterdam Airport to a forest in the municipality Putten, Gelderland, NL. There, the Zeppelin circled at three altitudes for a total of 57 min before continuing to Wageningen, NL, where another 3-level set of circles was flown within 43 min. On the way back to the airport, the third height profile was acquired for 57 min near the meteorological tower in Cabauw, NL. The flight started at 6:43 UTC and ended at 14:27 UTC. The flight track is depicted in Figure 3.1, the time series of the aerosol chemical species and black carbon concentration in Figure 3.2.

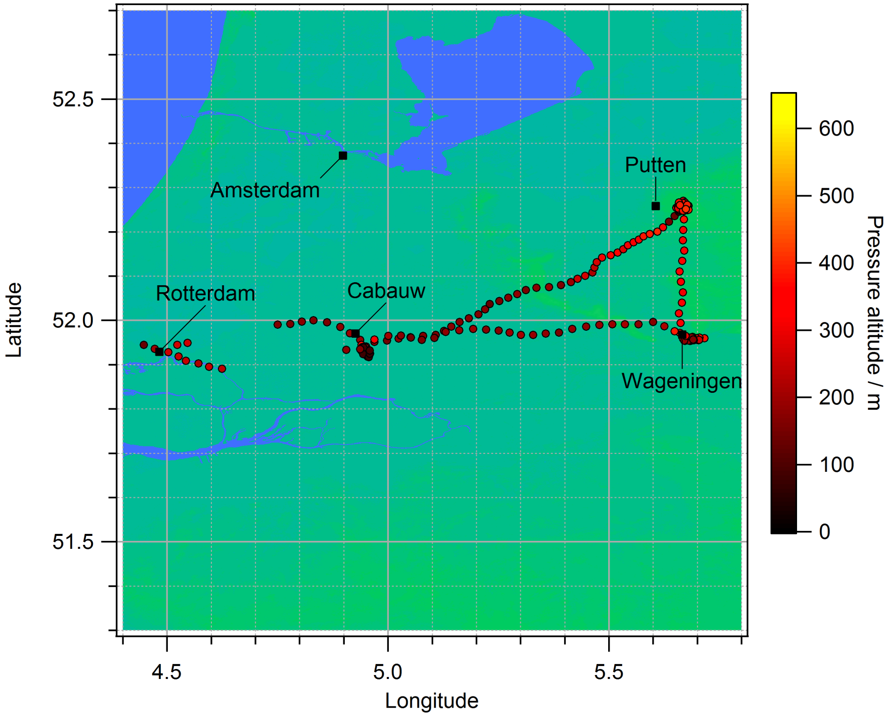

Figure 3.1.: Flight track for 21 May 2012. Data points are coloured by pressure altitude.

To visualize the periods in which the height profiles were acquired, the background for these periods is colour-coded by altitude. The resulting averaged height profiles for nitrate and organics are shown in Fig. 3.3a, Fig. 3.3b and Fig. 3.3c. In these figures, the vertical error bars represent the altitude range used for averaging the resulting data point. The horizontal error bars represent the standard deviation

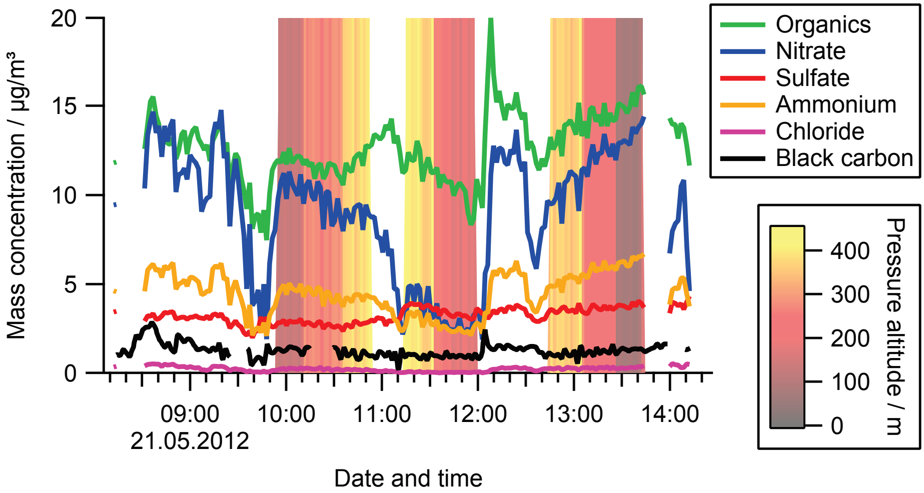

Figure 3.2.: Time series of the aerosol chemical species and black carbon concentration acquired during flight 11. Data gaps in the black carbon concentration originate from changing the Aethalometer filter spot (see subsection 2.3.2), gaps in all other time series are due to AMS measurements with a filter in the sampling line. For the time of height profiling, the background of the time series is shaded by flight altitude.

of the data points used for averaging. The number of underlying data points used for averaging is denoted next to the points in the graph. Note, that the height profiles have been acquired without repetition of altitude and over a time period. The variation of concentrations with height could thus also include diurnal changes to some degree.

In the Putten height profile in Fig. 3.3a, organics do not show a significant difference in altitude, whereas nitrate shows a decreasing trend with increasing altitude. The vertical profile in Wageningen (Fig. 3.3b) shows a clear increase with altitude for both organics and nitrate mass concentration. The level of nitrate concentration, however, is low compared to the average for 21 May. In Cabauw, the height profile (Fig. 3.3c) shows lower concentrations at higher altitudes for both organics and nitrate.

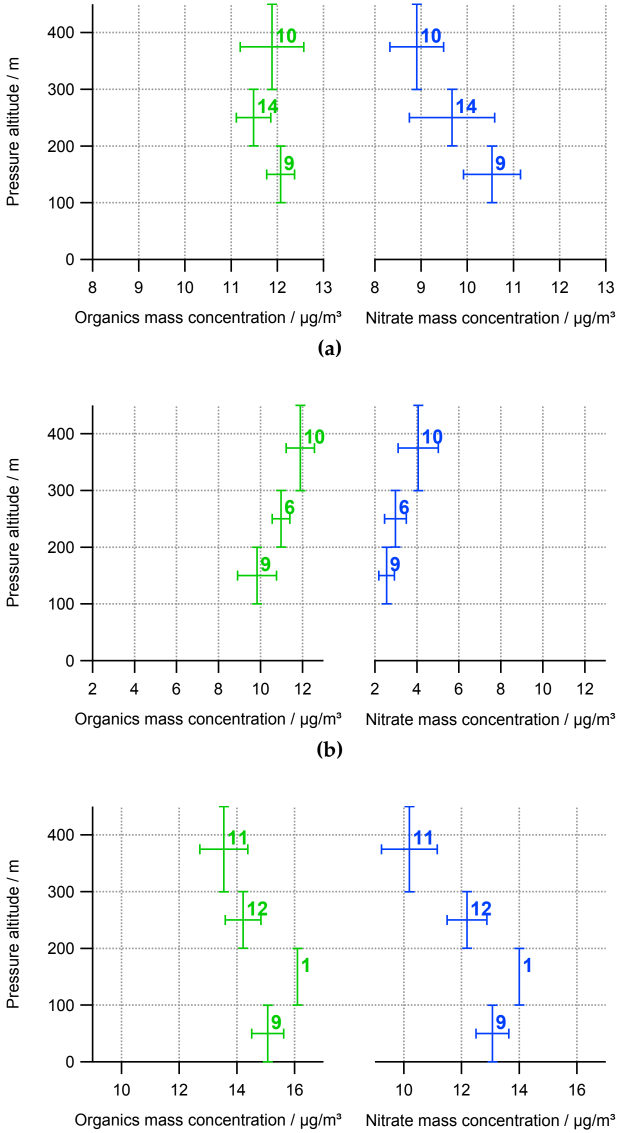

(a)

(b)

(c)

Figure 3.3.: Averaged height profiles over a forest in the municipality Putten, Gelderland, NL (Fig.3.3a), close to Wageningen, NL (Fig.3.3b), and close to the meteorological tower in Cabauw, NL (Fig.3.3c). The vertical error bars indicate the magnitude of the used altitude classes, whereas the horizontal error bars indicate the standard deviation of averaged points. The number of points averaged for each data point in this graph is indicated next to it.

3.1.2. Rotterdam: 2012-05-24, Flight No. 14

Flight 14 on 24 May was going to the meteorological tower at Cabauw, where height profiling circles were flown for the entire day. Unfortunately, a soot particle clogged the first critical orifice in the sampling system of the AMS (compare subsubsection 2.5.3.1) while the airship was on ground, being supplied with power by a diesel generator. This was not noticed and in consequence, the sampling efficiency of the instrument was drastically reduced. Efforts to calibrate for the soot particles effect proved ineffective because the influence seemed to be varying with time and particle concentration. Taking this all into consideration, the data from this day were excluded from further analysis.

3.1.3. Ozzano: 2012-06-20, Flights No. 27+28

On the first flight day with the SOA cabin layout on 20 June, two height profiling flights to a field near a ground site in San Pietro Capofiume (SPC), interrupted by a refuelling stop, were performed. The flight started at 4:37 UTC, reaching the height profiling site at 4:54 UTC. At 8:04 UTC, the site was left for refuelling, coming back at 9:07 UTC. At 11:56 UTC, the Zeppelin left the height profiling site again, landing at 12:04 UTC. The resulting time series of aerosol chemical species and black carbon concentration can be seen in Figure 3.4. For the time where the airship was at the height profiling site, the graphs background is shaded by airship altitude.

For nitrate, an increase in mass concentration at the low level was observed until the refuelling stop, thereafter the concentration was decreasing. At the high level, the nitrate concentration was below 1 $\mu g/m^3$ throughout both flights. For organics, the low altitude trend was similar to the nitrate trend, but peaking at 9:30 UTC, when the nitrate concentration was already declining. The high altitude organics concentration decreased to lower values than on low altitudes during the first high altitude circling period. It then slowly increased, the difference to the low altitude concentration becoming larger. In the very beginning of the height profiling, the concentration of sulfate in the high altitude was enhanced compared to the low altitude observations. Over the course of the second flight on 20 June, the differences between low and high altitude observations generally diminished.

In all species, there are altitude changes during which the concentration was greatly increased. This effect was most pronounced for nitrate during flight 27. Figure 3.5 shows the averaged height profile for flight 27. The elevated concentration was clearly located in the altitude between 200 m and 400 m. The averaged height profile of organics, sulfate and nitrate for flight 28 is shown in Figure 3.6.

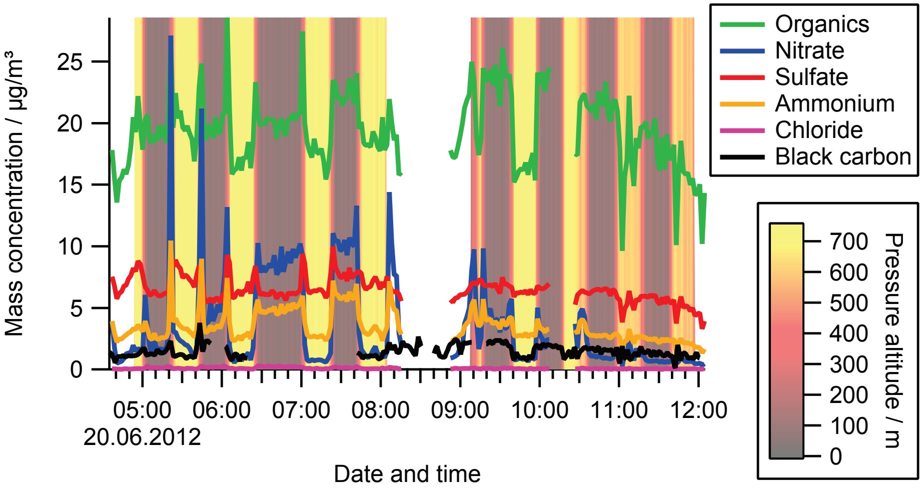

Figure 3.4.: Time series of the aerosol chemical species and black carbon concentration acquired during flight 27 and flight 28. Data gaps in the black carbon concentration originate from changing the Aethalometer filter spot (see subsection 2.3.2), gaps in all other time series are due to AMS measurements with a filter in the inlet line. For the time of height profiling, the background of the time series is shaded by flight altitude.

Compared to flight 27, the sulfate concentration had slightly decreased. The high altitude organics concentration had slightly decreased, whereas the low altitude concentration increased. The nitrate concentration decreased overall, most prominently at low altitudes.

A closer inspection of the nitrate concentration time series (Figure 3.7) reveals, that after 10:00 UTC, the high altitude nitrate concentration was actually higher than the low altitude concentration. Note, that due to higher outside temperatures, the altitude reached on the high level went down from roughly 725 m above sea level to about 625 m above sea level in this period.

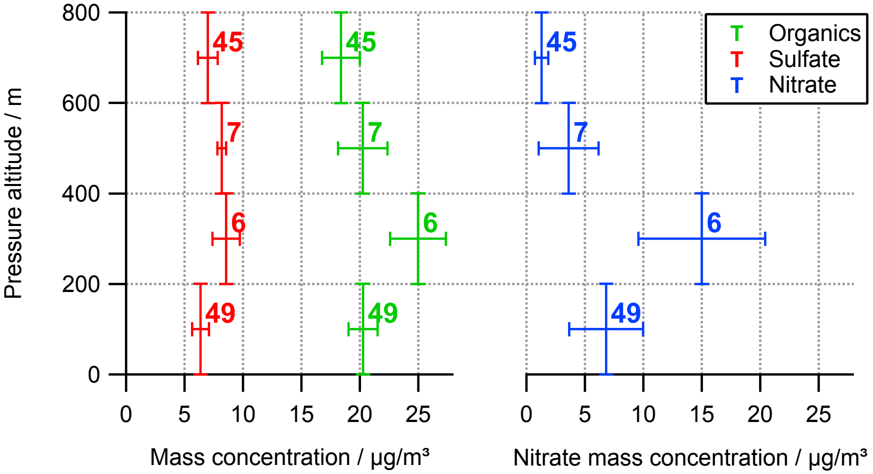

Figure 3.5.: Height profile for organics, sulfate and nitrate during flight 27. The vertical error bars show the magnitude of the used altitude classes, whereas the horizontal error bars indicate the standard deviation of the data points averaged for each point in the graph. The number of points used for averaging is denoted next to the points.

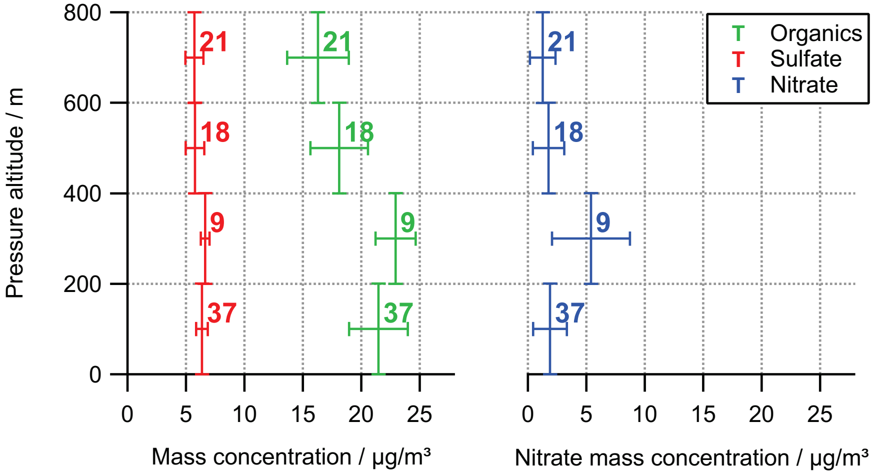

Figure 3.6.: Height profile for organics, sulfate and nitrate during flight 28. The vertical error bars show the magnitude of the used altitude classes, whereas the horizontal error bars indicate the standard deviation of the data points averaged for each point in the graph. The number of points used for averaging is denoted next to the points.

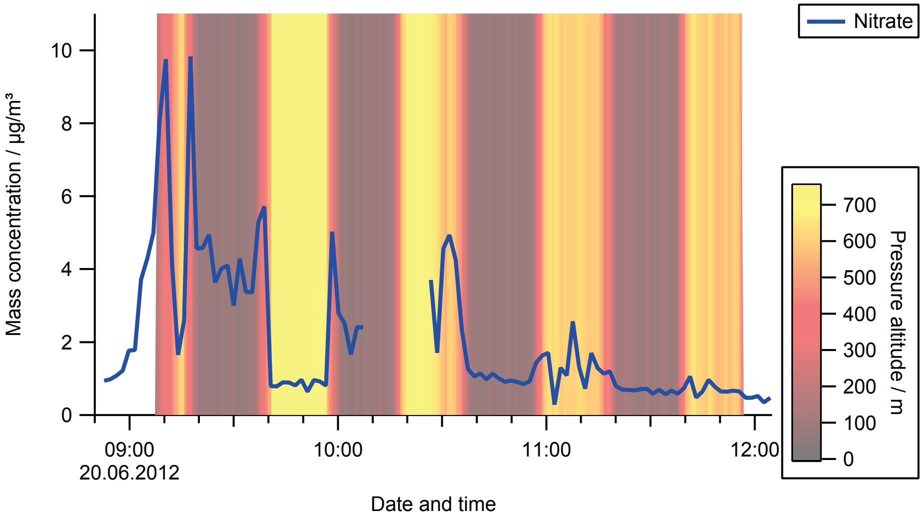

Figure 3.7.: Isolated time series of nitrate concentration as measured during flight 28. For the time when the airship was at the height profiling site, the background is shaded by altitude.

3.1.4. Ozzano: 2012-07-03, Flight No. 40

On 3 July, a flight to Bosco Fontana was performed (Figure 3.8). It started at 03:53 UTC, passing the SPC site at an altitude of 300 m at approx. 4:10 UTC. Afterwards, the flight continued towards Bosco Fontana, first staying at 300 m, changing to 600 m at 4:40 UTC. Bosco Fontana was reached at 6:03 UTC. Within 74 min, a three level height profile with two repetitions was acquired there. The flight back was conducted at an altitude of 350 m, arriving at the airport at 09:37 UTC. Bosco Fontana is a forest near Mantua, which served as a measurement site in the European project ÉCLAIRE. The time series of aerosol chemical species and black carbon concentration acquired during the flight is displayed in Figure 3.9.

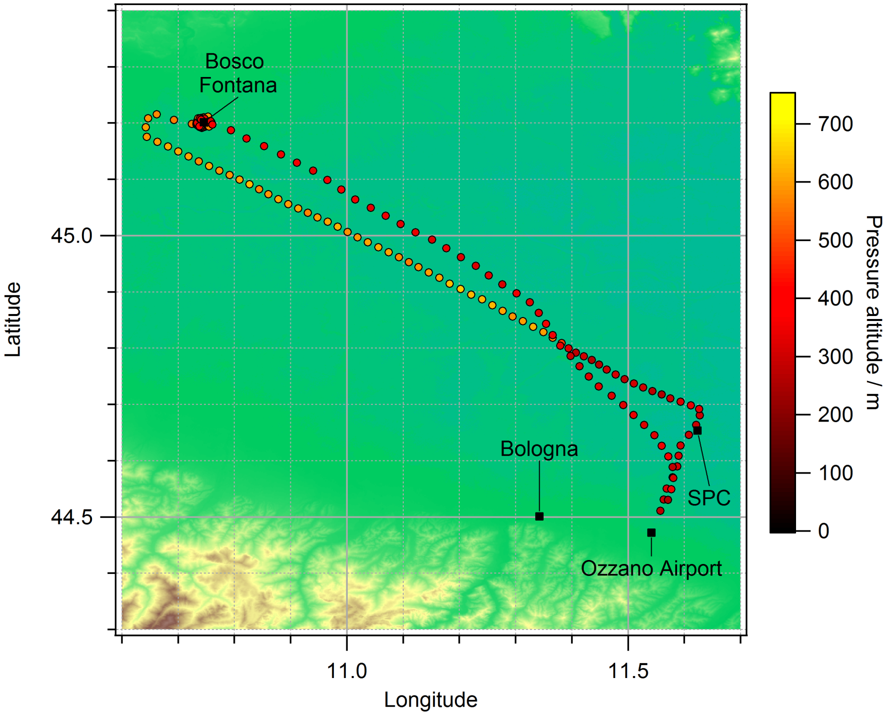

Figure 3.8.: Flight track for 3 July 2012. Data points are coloured by pressure altitude.

When averaging the data acquired in Bosco Fontana into altitude classes (Figure 3.10), it becomes apparent that all species had reduced concentrations above 500 m. On the intermediate altitude, nitrate concentration showed a clear evolution with time, with values of around 1 µg/m^3 at 6:35 UTC and around 2.5 µg/m^3 at 8:10 UTC.

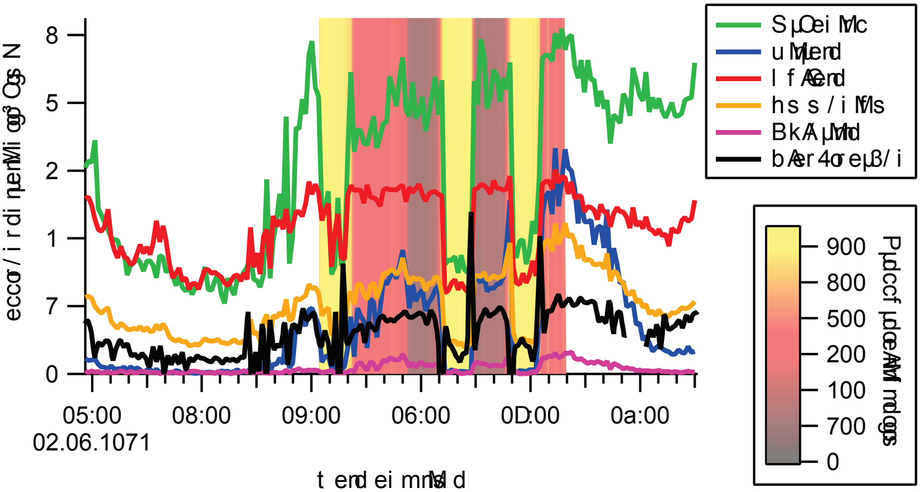

Figure 3.9.: Time series of the aerosol chemical species and black carbon concentration acquired during flight 40. Data gaps in the black carbon concentration originate from changing the Aethalometer filter spot (see subsection 2.3.2). For the time of height profiling, the background of the time series is shaded by flight altitude.

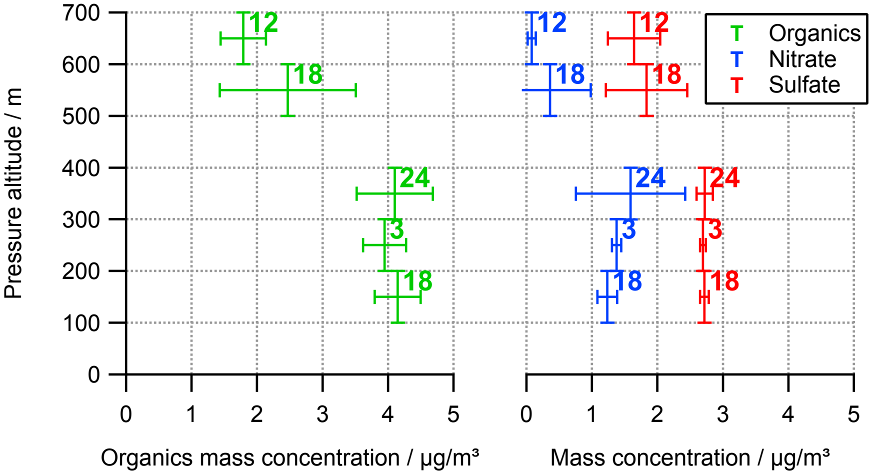

Figure 3.10.: Averaged height profile for organics, nitrate and sulfate between 6:04 UTC and 8:18 UTC in Bosco Fontana. The vertical error bars show the magnitude of the used altitude classes, the horizontal error bars correspond to the standard deviation of the underlying data points. The number of points used for averaging is noted next to the points in the graph.

3.2. Transects

In contrast to the height profiling flights, transect flights have generally been flown at a relatively constant altitude. The goal was to detect either the spatial distribution, the temporal evolution or sharp gradients of the concentration of trace species.

3.2.1. Rotterdam: 2012-05-22, Flight No. 12

On 22 May, flight 12 was going from Rotterdam Airport to Cabauw, from there via Rotterdam to the North Sea and back to the airport. The exact flight track is shown in Figure 3.11. Over the sea, the Zeppelin switched to a higher altitude and the flight back to the airport was continued on higher altitude than the flight to the sea.

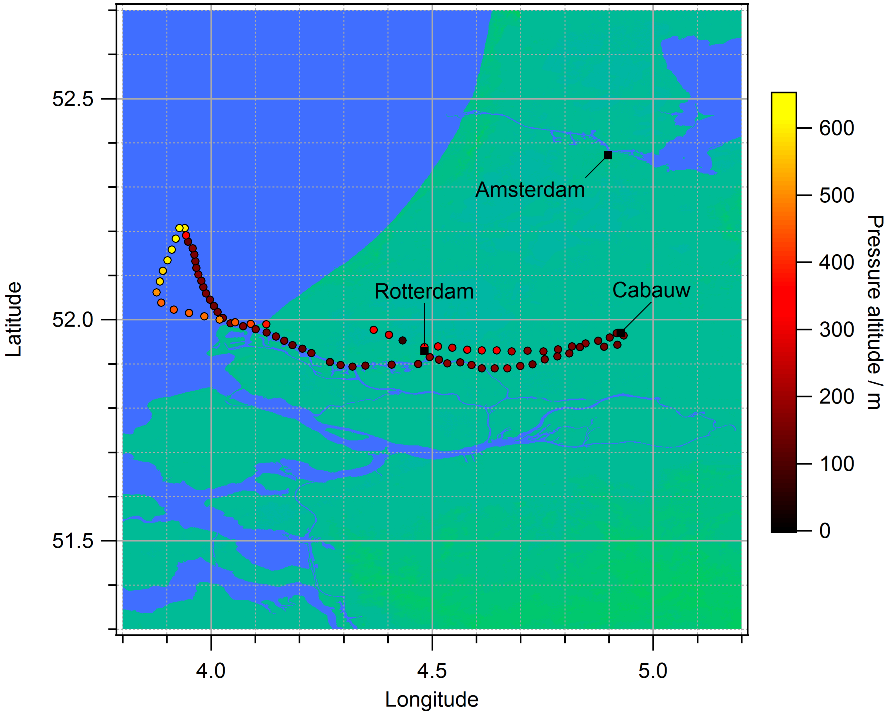

Figure 3.11.: Flight track for 22 May 2012. Data points are coloured by pressure altitude.

The time series of aerosol chemical species and black carbon concentration acquired during flight 12 is shown in Figure 3.12. The observed concentrations were relatively stable east of Rotterdam (approx. 15:00 UTC to 15:55 UTC, ±5 % to ±10 %, depending on the species) at a flight altitude between 150 m and 300 m, then decreased during the flight over the river Nieuwe Maas. The minimum (approx. 16:20 UTC) was reached above the Rotterdam district Hoek van Holland. Beginning at approx. 6 km past the shore, organics and nitrate concentrations rapidly increased. After surpassing the maximum concentration (approx. 9 km from the shore), the airship changed altitude from below 200 m to above 450 m and changed course. The observed organics and nitrate concentrations at first sharply decreased and then increased again, having their maximum over Hoek van Holland, where an hour earlier and 200 m lower, the lowest concentrations had been observed.

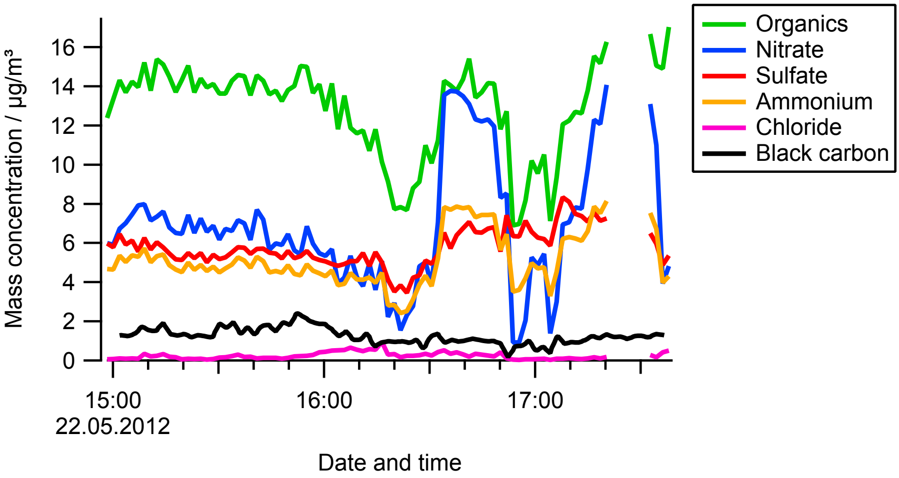

Figure 3.12.: Time series of the aerosol chemical species and black carbon concentration acquired during flight 12. The gap in AMS data is due to measurements with a filter in the inlet line.

3.2.2. Ozzano: 2012-06-21, Flights No. 29+30

On 21 June, flights 29 and 30 were performed as north-south transects between approx. 10 km north of the San Pietro Capofiume supersite in the north and the Apennines in the south. From there, a valley was followed in south-westerly direction. The exact flight track can be found in Figure A.2 on page 132. The time series in Figure 3.13 show, that in three of four northern turning points the concentration of the chemical species were at a maximum, indicating that the airship flew into a plume, but not passing it. The NO_x time series in Figure 3.13 shows similar behaviour at the first northern turn. Later, the maximum in NO_x concentration was further south of the turning point. It is also notable, that the rise of the NO_x level coincided with the increase of black carbon, organics and sulfate level, but the nitrate concentration began rising further north. Northern turn 2 showed almost no enhancement in aerosol chemical species and black carbon, whereas the NO_x shows a similar pattern to turn 3 and 4.

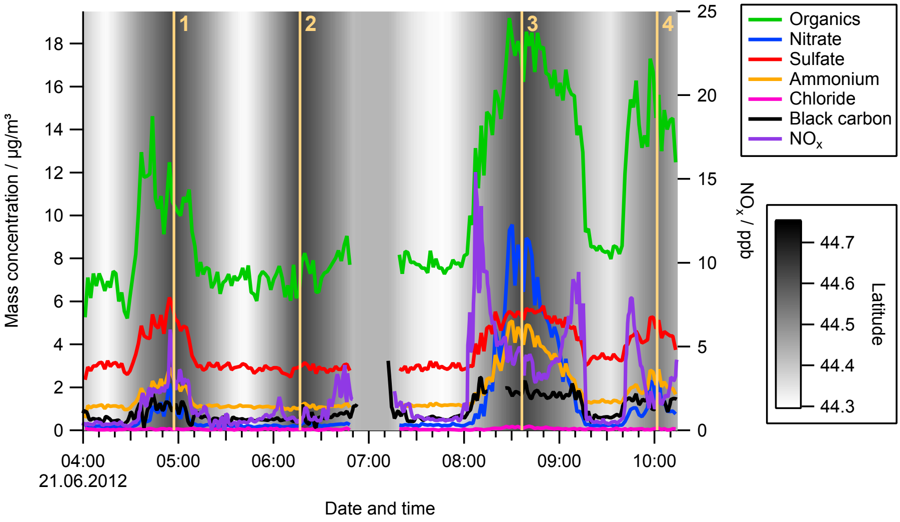

Figure 3.13.: Time series of aerosol chemical species, black carbon and NO_x concentration observed during flight 29 and 30. The data gap between 6:50 UTC and 7:15 UTC is due to a refuelling stop. The background is shaded by latitude to visualize the turning points (darkest and lightest shades). The northern turning points are indicated by lines of sandy colour and corresponding numbers.

The rise in organics mass concentration in the northern part of the flight was accompanied by a significant drop in averaged carbon oxidation state $\overline{OS}_C$, indicating a lower oxygen content and a less oxidized aerosol during these periods (Figure 3.14).

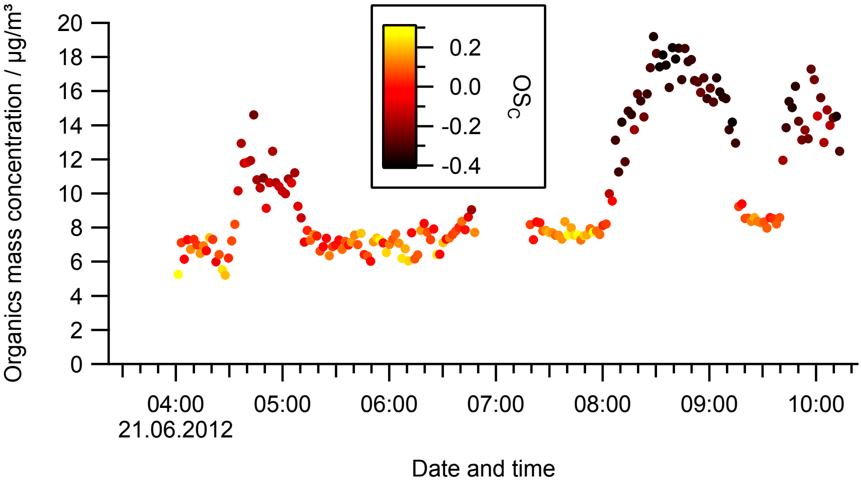

Figure 3.14.: Time series of organics mass concentration, coloured by the averaged carbon oxidation state. Elevated mass concentrations show a drop in oxidation state.

3.2.3. Ozzano: 2012-06-22, Flight No. 31

On 22 June, the airship flew from Ozzano Airport to SPC and from there eastwards until approx. 30 km past the shoreline of the municipality Cormacchio. Afterwards, approximately the same route was flown back. The exact flight track can be found in Figure A.3 on page 133.

The time series of organics, ammonium and black carbon in Figure 3.15 show a peak between approx. 05:10 UTC and 05:30 UTC, corresponding to a region downwind of a lagoon north of Cormacchio. Just before reaching the coast, the concentrations decreased and continued decreasing over the ocean. In the last half-hour over the sea (6:30 UTC – 7:00 UTC), a peak in organics, sulfate and ammonium was observable. Upon reaching land again, the concentrations reached higher levels again.

As Figure 3.16 shows, the averaged $\overline{OS}_C$ in the peak of the organic mass concentration at approx. 5:30 UTC was lower than in the beginning of the flight and over the sea. The organics peak before reaching land did not show a lowered carbon oxidation state. When the coastline was reached, $\overline{OS}_C$ dropped to lower levels.

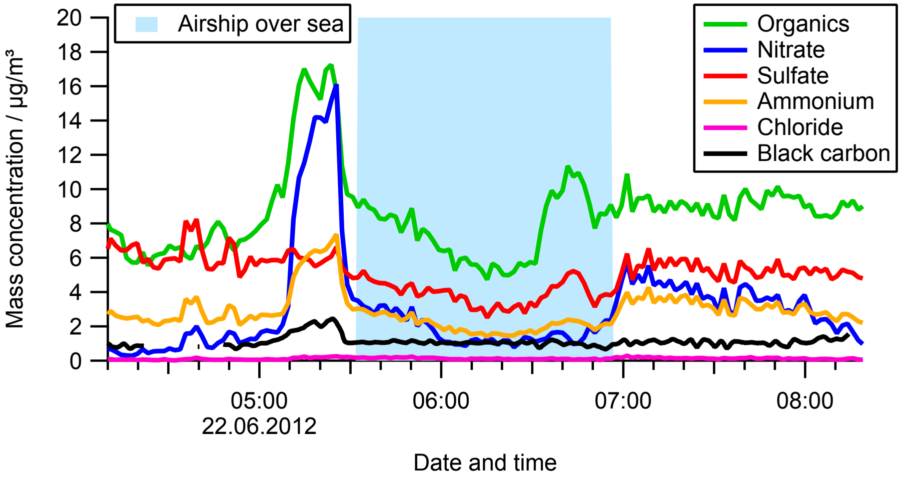

Figure 3.15.: Time series of aerosol chemical species and Black carbon on 22 June. The time in which the airship was over the Adriatic Sea is highlighted in light blue.

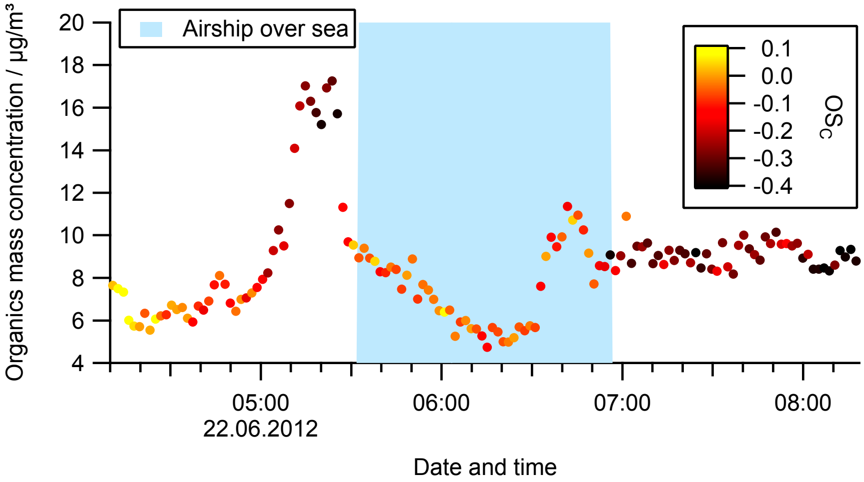

Figure 3.16.: Time series of organics mass concentration on 22 June, coloured by the averaged carbon oxidation state. The time in which the airship was over the Adriatic Sea is highlighted in light blue.

3.2.4. Ozzano: 2012-06-24, Flight No. 32

The flight track for flight 32 on 24 June was similar to flight 31 on 22 June and is shown in Figure A.4 on page 134. The the Zeppelin started in Ozzano at 06:54 UTC, passing SPC at approx. 7:20 UTC at an altitude of 300 m. From there, the flight went eastwards, reaching the coast at 8:17 UTC. Then, three back-and-forth flight elements approx. between 30 km inland and 15 km offshore were performed before returning to the airport and landing at 13:15 UTC.

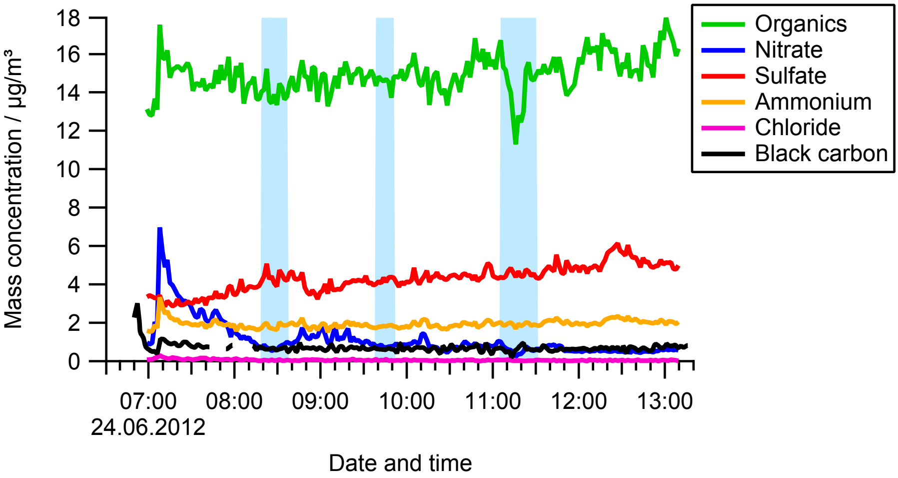

Figure 3.17.: Time series of aerosol chemical species and black carbon for flight 32. Periods in which the airship was over the Adriatic Sea are highlighted in light blue.

Organics, nitrate and ammonium showed an abrupt rise in concentration on the way to SPC, declining afterwards. In the case of nitrate, the concentration decreased until reaching the coastline for the first time. The concentrations of all measured species were relatively stable throughout the rest of the flight, with small upwards trends in organics, sulfate and ammonium and a small downwards trend in nitrate.

3.2.5. Ozzano: 2012-07-01, Flight No. 39

Flight 39 was performed on 1 July. First, a two-altitude height profile was acquired, then the flight went from Ozzano past Bologna to Vignola, from where the valley of the river Panaro was followed into the Apennines until the Zeppelin could not go any further. From there, the flight went back out of the valley in North-Easterly direction to San Giovanni in Persiceto, then into the valley again and back to Ozzano. The exact flight track is shown in Figure 3.18. The flight to the valley (approx 05:30 UTC to 06:10 UTC) was performed at a high altitude of 550 m to 600 m. The flight periods into the valley were done at low heights (< 200 m above ground), whereas the flight periods out of the valley were done at a relatively constant altitude of approx. 400 m above sea level.

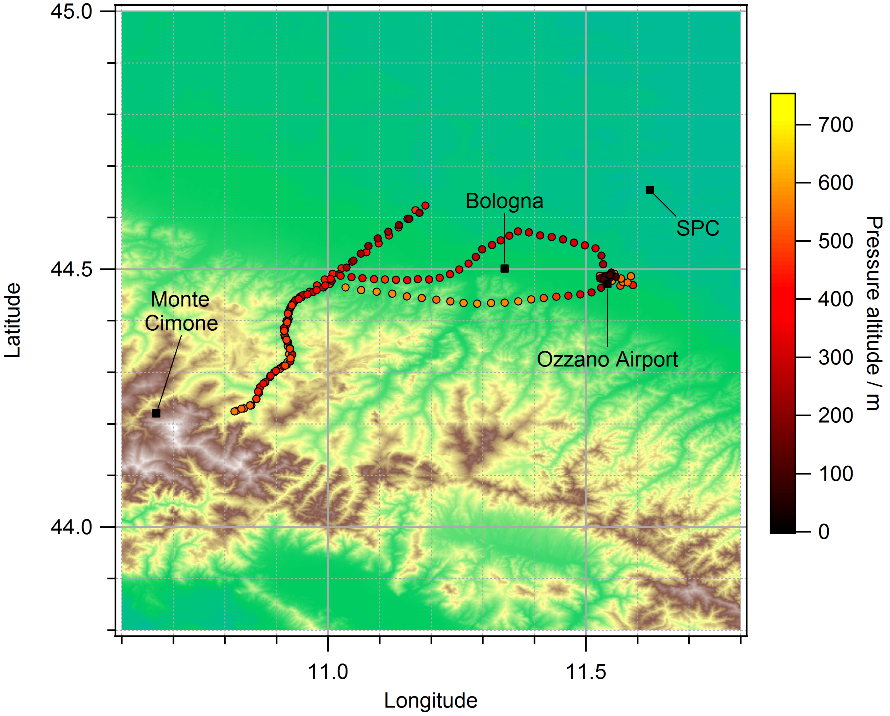

Figure 3.18.: Flight track for 1 July 2012.

The time series of aerosol chemical species and black carbon is shown in Figure 3.19. For the duration of the height profile, the background of the graph is shaded by altitude. All measured species showed significantly lower concentrations on the low altitude compared to the high altitude.

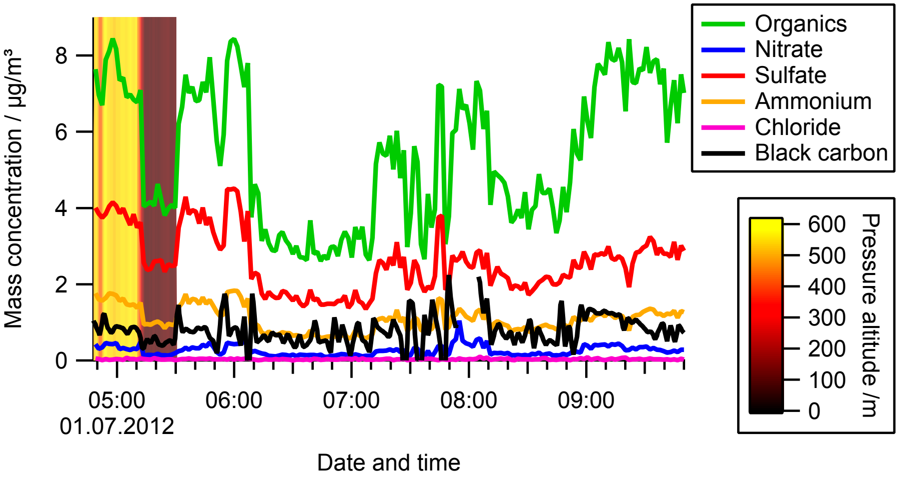

Figure 3.19.: Time series of aerosol chemical species and black carbon concentration as measured during flight 39. The background during a two-altitude height profile in Ozzano is shaded by altitude.

3.2.6. Ozzano: 2012-07-04, Flight No. 41

Flight 41 on 4 July went to the same valley as flight 39. The flight track can be found in Figure A.5 on page 135.

The time series of measured aerosol chemical species and black carbon concentration is shown in Figure 3.20, with the background coloured by latitude. Most species showed a peak in concentration just south of the northern turning point.

The nitrate time series is depicted in a different manner in Figure 3.21. Here, the latitude of the airship is shown as a function of time, with the data points coloured by nitrate concentration. It becomes apparent, that the position of the peak concentration was at a constant location and the concentration was higher when flying into the valley at a low height than when flying out of the valley at high altitude.

The equivalent plot for sulfate in Figure 3.22 does not show a height-dependence, but the maximum in sulfate concentration was moving southwards from pass to pass.

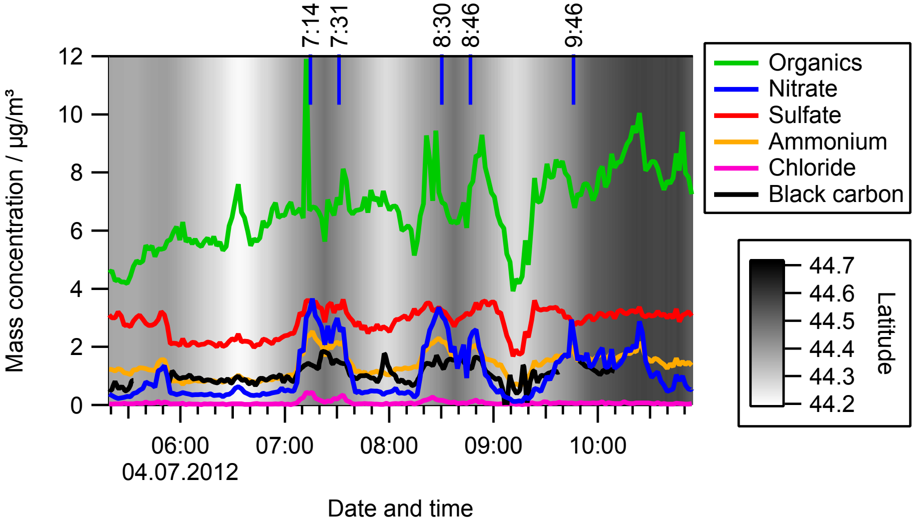

Figure 3.20.: Time series of aerosol chemical species and black carbon concentration acquired during flight 41. The background of the figure is shaded by latitude, making the turning points during the flight visible in darkest and lightest shade. The position of the maximum of nitrate concentration is indicated with vertical lines of blue colour.

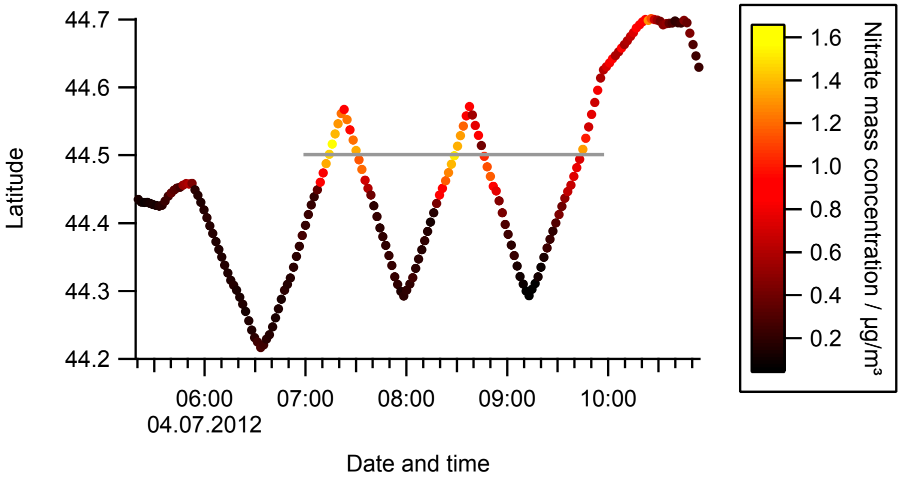

Figure 3.21.: Time series of the airship latitude, coloured by nitrate mass concentration. A maximum at 44.5° northern latitude is visible, marked by the grey line.

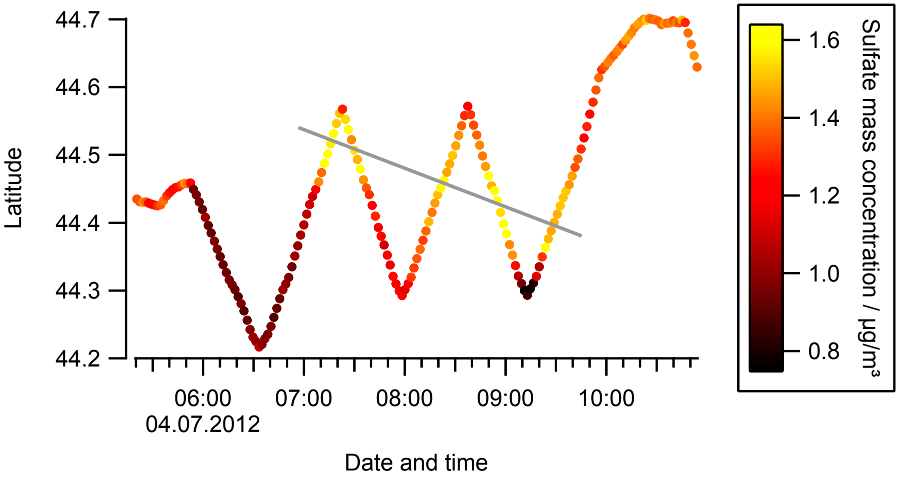

Figure 3.22.: Time series of the airship latitude, coloured by sulfate mass concentration. A maximum moving from 44.5° northern latitude to 44.4° northern latitude (marked by grey line) is visible.

4. Results and Discussion

4.1. Comparison with particle number based measurements

Particle number size distribution measured by the SMPS in the CPN rack are based on the aerosol number concentration. They can be converted into volume size distributions and then be integrated to yield the total aerosol volume concentration. If information about the density of sampled particles is available, the aerosol volume concentration can be converted to aerosol mass concentration. As the AMS measures the aerosol chemical composition, it is possible to express the aerosols density as a sum of bulk compound densities, weighted by the mass fraction of the respective compound. Following Cross et al. (2007), the inorganic species were merged, and a density of 1770 kg/m^3 was applied. For the organic material, a parametrization based on the elemental composition introduced Kuwata et al. (2012) was used to calculate the density. In Figure 4.1, the mass concentration as calculated from SMPS measurements is compared to the sum of mass concentrations measured by the AMS and the Aethalometer.

There is a strong correlation (Pearson $R^2 = 0.74$) between both mass concentrations. The slope of a linear regression through all data (the average ratio between the mass concentrations) is 0.50 instead of unity as expected for measurements in good agreement. Comparisons between instruments as used here lead to uncertainties in the range of 45 % (Middlebrook et al., 2012). The observed ratio is outside this uncertainty range. Potential reasons for this can originate in both the SMPS and the AMS.

The SMPS had limited sizing range, during the 2012 PEGASOS campaigns the cutoff diameter was 414 nm. Assuming a density of 1600 kg/m^3, this translates to a vacuum aerodynamic diameter of 662 nm. The AMS aerodynamic lens transmission declines the same range, but does so smoothly over a few hundred nm (Zhang et al., 2004; Liu et al., 2007). If the sampled aerosol would contain significant numbers of particles in the size range where they are detected by the AMS but not by the SMPS, an underestimation of the particle volume and therefore mass by the SMPS would arise. Small numbers of large particles can lead to

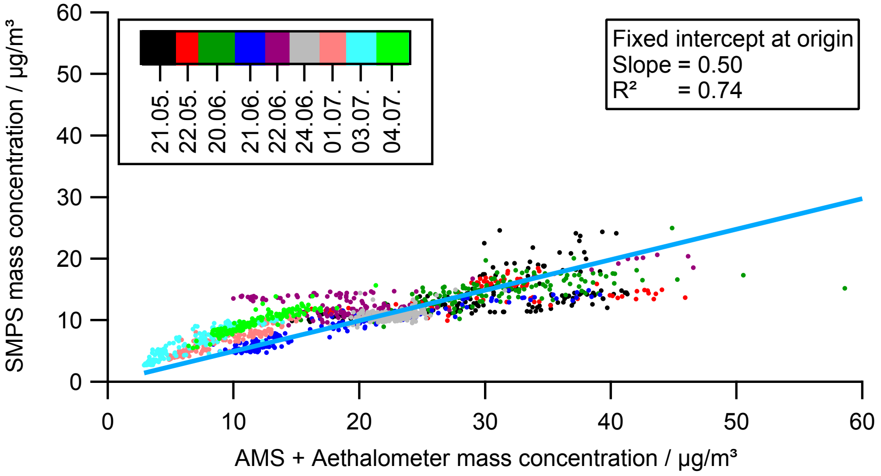

Figure 4.1.: Correlation of mass concentration calculated from SMPS measurements versus the sum of mass concentrations measured by AMS and Aethalometer. The data points are coloured according to the measurement day. The light blue line represents the result of a linear regression with a fixed intercept of zero.

significant contributions in particle mass. Another potential issue with the SMPS is the evaporation of particles within the instrument. The particle-laden air has a relatively long residence time within the instrument, and the high temperatures especially during the southbound campaign led to very high temperatures inside the Zeppelin gondola where the instruments were installed, favouring particle evaporation. Also, the SMPS relies on mass flow controllers for regulating the flows that determine the selection of particle sizes. Elevated temperatures could here lead to changes in volume flows, influencing the particle sizing.

An issue with the AMS could be errors in the ionization efficiency calibration. For the observed discrepancy, these errors would have had to occur consistently in every calibration. This is thought to be unlikely, but cannot be unambiguously excluded. Another potential source of error could be found in the collection efficiency. If the Zeppelin-AMS had a better collection efficiency than previous instruments, including those used for development of the elaborate collection efficiency calculation algorithm by Middlebrook et al. (2012), this would influence the total mass determined by the AMS. Because the collection efficiency calculated here after Middlebrook et al. (2012) was at 0.45 in most cases, a collection efficiency near one would lead to excellent agreement between the mass concentrations. For example, if the vaporizer of the Zeppelin-AMS would be coated with "sticky" material not evaporating at the normal operating temperature of 600 °C and during the velocity calibrations where the vaporizer is kept at 900 °C, the fraction of particles bouncing off the vaporizer could be reduced, thus increasing the collection efficiency. But because collection efficiencies consistently near unity have not been reported before for ambient measurements and cannot be experimentally supported in this work, the assumed collection efficiency was kept at the values calculated with the algorithm developed by Middlebrook et al. (2012).

The source of the systematic deviations between SMPS based and AMS based mass concentrations cannot be identified definitely here, and an uncertainty of the absolute mass of a factor of two to lower masses has to be assumed. The potential influences on the scientific conclusions made in this work, however, are small. Most of the detailed analyses rely on relative changes in the observations over time and between the different aerosol constituents, which are not influenced by the total mass concentration.

4.2. Chemical composition in the east- and southbound campaigns

A difference between mobile measurements on a platform like the Zeppelin NT airship and stationary ground-based measurements is, that stationary measurements can only observe variations in time, whereas mobile measurements can additionally cover variations in the three dimensions of space. While this feature enables additional insight into scientific questions unsolved by stationary measurements, measurements on flying platforms have a reduced density per point in time and space. This effect is further extended by the limited hours of operation for a mobile platform, in contrast to ground-based measurements that often run for months and years with only small interruptions. Consequentially, the measurements performed during the nine evaluated measurement days can only provide episodic insight into the general aerosol composition in the Netherlands and in the Po Valley.

By averaging all data points acquired during the eastbound campaign, an average PM_1 mass concentration of $31.4\,\mu g/m^3$ was observed. The distribution on the different aerosol compounds is shown in Figure 4.2. The highest contribution came from organics (40 %), followed by nitrate (27 %). In the southbound campaign, the average PM_1 mass concentration was only $18.7\,\mu g/m^3$. Apart from actual concentration differences between the Netherlands and the Po Valley, this could also be biased by the fact, that measurements were taking place mostly in the first half of the day during the southbound campaign and some measurements were

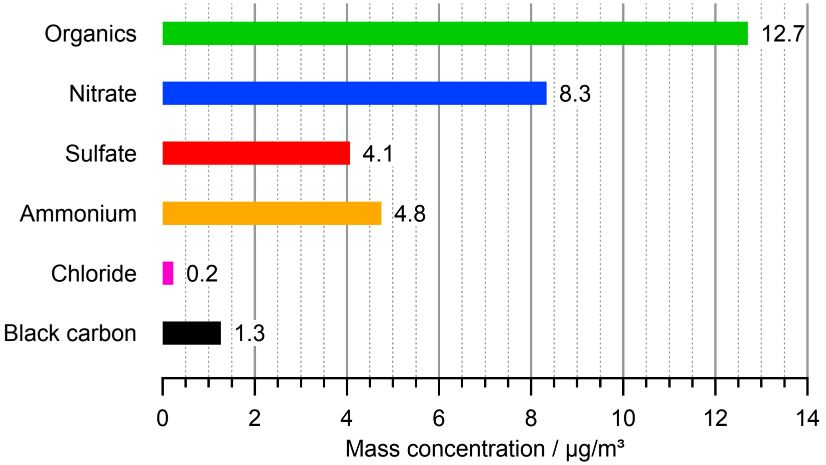

Figure 4.2.: Average mass concentrations observed during the eastbound 2012 PEGASOS campaign.

taken in cleaner layers of the PBL (compare section 4.4). The average southbound campaign aerosol composition is shown in Figure 4.3.

The highest contribution was again from organics (54 %), however it was followed by sulfate (21 %). In absolute numbers, nitrate aerosol mass concentration exhibited the biggest difference between the eastbound and the southbound campaign, followed by ammonium aerosol mass concentration. These differences are thought to originate in the different sources, e. g. by different types of industry and agriculture in the two regions.

For the organic aerosol, mass spectral markers and elemental ratios can provide more insight. Ng et al. (2010) initiated the use of the contribution of m/z 44 (predominantly CO_2^+, abbreviated as f_{44}) and m/z 43 (predominantly $C_2H_3O^+$, abbreviated as f_{43}) to the organic mass spectrum as diagnostic for following the ageing of organic aerosol. A graph of f_{44} versus f_{43} is shown in Figure 4.4.

This graph illustrates, that observations during the 2012 PEGASOS campaigns are in the range of previous observations of oxidised organic aerosol. The eastbound campaign (21 May and 22 May) data points are separate from the southbound campaign data points, in a different part of the triangle of previous observations. Comparing to Ng et al. (2010), f_{44} and f_{43} observed during the southbound campaign fall into the range of observations associated with low volatile oxidised organic aerosol. For the eastbound campaign, f_{44} and f_{43} fall on the border of observations associated with low volatile and semivolatile oxidised organic aer-

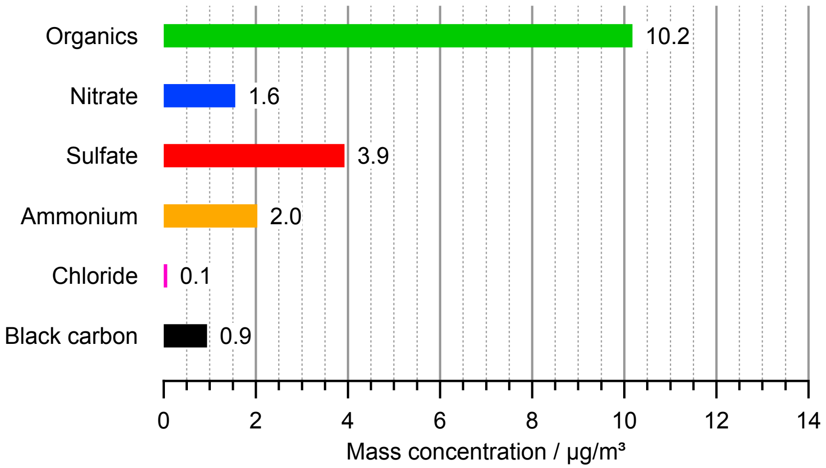

Figure 4.3.: Average mass concentrations observed during the southbound 2012 PEGASOS campaign.

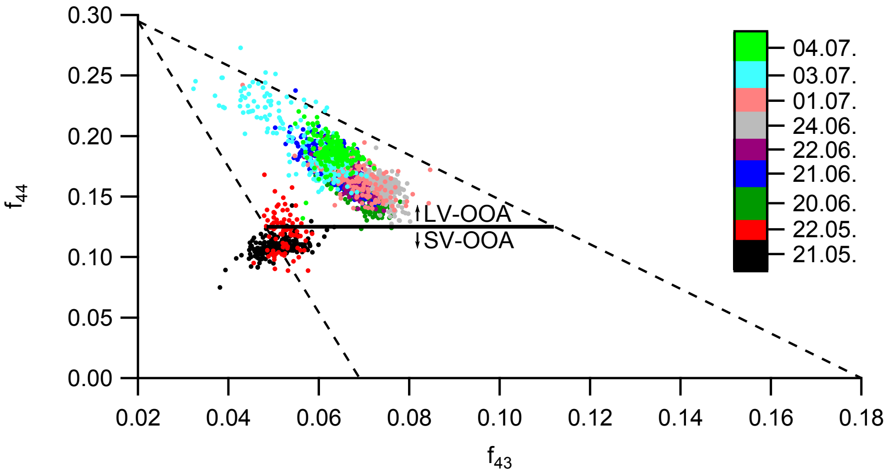

Figure 4.4.: f_{44} versus f_{43} for the 2012 PEGASOS campaign. The data points are coloured by date, with black (21 May) and red (22 May) representing the eastbound campaign. The dashed lines indicate the space of previous ambient observations (compare Ng et al., 2010). The solid black line indicates the border between low volatile oxidised organic aerosol (LV-OOA) and semivolatile oxidised organic aerosol (SV-OOA) as found by Ng et al. (2010).

osol. As f_{44} and f_{43} are defined relative to the total organic mass spectrum, the increased signal amount of less oxidised fragments in the eastbound campaign is one reason for f_{44} and f_{43} being lower for the eastbound campaign than for the southbound campaign. The difference between the two campaigns indicates a fresher, less aged organic aerosol in the Netherlands compared to the Po Valley.

Another diagnostic tool is the van Krevelen diagram (van Krevelen, 1950), introduced for organic aerosol characterization by Heald et al. (2010). In this diagram, the atomic H/C ratio is displayed as a function of atomic O/C ratio. In Figure 4.5, such a diagram is shown for PEGASOS 2012.

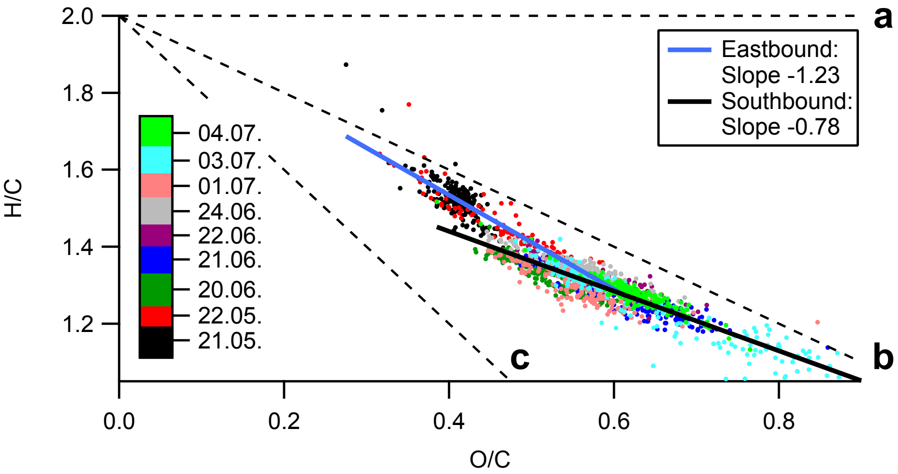

Figure 4.5.: Van Krevelen diagram for the 2012 PEGASOS campaign. The atomic H/C ratio of the organic aerosol is plotted against the atomic O/C ratio of the organic aerosol. The data points are coloured by date, with black (21 May) and red (22 May) representing the eastbound campaign. The slope for the measurements during the eastbound campaign (light blue line) is steeper than the slope for the measurements during the southbound campaign (black line).

The dashed lines **a**, **b**, and **c** in Figure 4.5 have a slope of 0, -1, and -2, respectively. Their origin is set at the point $H/C = 2$ and $O/C = 0$, representing an alkane of infinite chain length. Line **a** represents the change in H/C and O/C for a conversion of CH_2 groups to hydroxyl (or hydroperoxy) groups. A conversion to carboxyl groups would lead to atomic ratios along line **b**. Line **c** would be created by the successive conversion of CH_2 groups to carbonyl groups. Previous atmospheric and laboratory observations are reported to be falling close to line **b** (Heald et al., 2010). Observations during the PEGASOS 2012 campaigns show the same behaviour. However, when separating the data into the two campaigns, a difference in slopes is apparent. The data obtained in the Netherlands shows a slope of -1.23, while the data obtained in the Po Valley falls on a line with a slope of -0.78. A possible interpretation is, that the combination of SOA precursors and atmospheric oxidants in the Netherlands led to a higher amount of functionalization with carboxylic acid groups relative to the situation in the Po Valley, in agreement with the low f_{43} of observations made in the Netherlands (compare Figure 4.5).

4.3. Chemical composition and hygroscopicity

Atmospheric aerosol has an influence on climate via the formation of clouds. The potential of particles to be activated to cloud droplets depends on their hygroscopicity, thus on particle composition. Here, the hygroscopic properties of aerosols during the PEGASOS 2012 campaign will be quantified based on their composition as determined by the AMS.

To be able to apply mixing rules for predicting the hygroscopicity parameter κ, the concentrations of the pure components must be extracted from the AMS data. Gysel et al. (2007) suggested a simplified ion pairing scheme to calculate the concentrations of the inorganic substances ammonium nitrate NH_4NO_3, sulfuric acid H_2SO_4, ammonium bisulfate NH_4HSO_4 and ammonium sulfate $(NH_4)_2SO_4$, whose compound κ values are known. Here, a modified version of that ion pairing scheme is applied. The NH_4NO_3 molar concentration is assumed to be equal to the nitrate ion molar concentration. The remainder of ammonium ions is then distributed into the sulfate compounds according to the molar ratio of remaining ammonium ions to sulfate ions. For ratios between zero and one, the resulting species are H_2SO_4 and NH_4HSO_4. For ratios between one and two, the resulting species are NH_4HSO_4 and $(NH_4)_2SO_4$. For ratios above two, all available sulfate ions are assumed to be bound as $(NH_4)_2SO_4$. The excess ammonium ion concentration is ignored in this case.

In practice, κ is concentration dependent as it contains the water activity a_w by definition (Equation 2.13). Therefore, κ determined by hygroscopic growth measurements at 90 % relative humidity RH differs from κ determined by cloud activation measurements at varying values of supersaturation, leading to higher water contents. Since both κ_{90} and κ_{CCN} are discussed in the literature, both will be treated in the following. κ_{90} can for example be used for later comparisons with the hygroscopic growth factor derived measurements carried out on board the Zeppelin (see subsection 2.3.2). For κ_{90}, pure compound values suggested by Good et al. (2010) were used, tabulated in Table 4.1.

Table 4.1.: κ_{90} values and densities for pure compounds, used for prediction of growth factors at a relative humidity of 90 % and a dry diameter of 300 nm.

Compound	κ_{90} (90 % RH, D_{dry} = 300 nm)	Density / kg/m^3
NH_4NO_3	0.597	1725
H_2SO_4	0.870	1840
NH_4HSO_4	0.543	1780
$(NH_4)_2SO_4$	0.483	1769

For the inorganic compounds, bulk densities were assumed. For the organic material density, a parametrization based on O/C and H/C ratios, introduced by Kuwata et al. (2012) was used. A κ_{90} value of 0.085, as suggested by Good et al. (2010), was used for organics. Optionally, black carbon was taken into account, assuming a density of 2000 kg/m^3 and a κ_{90} of 0. This κ_{90} is lower than any other considered compounds κ_{90}, meaning that any amount of black carbon in the aerosol reduces the total κ_{90}.

For predicting aerosol activated fractions a_f, pure component κ_{CCN} values reported by Petters and Kreidenweis (2007) and Padró et al. (2010) were applied (see Table 4.2). The CCN concentration of an aerosol can be expressed as a_f times the total aerosol number concentration. However, as can be seen from section 4.2, the contribution of black carbon to the total particle mass is small.

Table 4.2.: κ values for pure compounds, determined with cloud droplet activation measurements, used for the prediction of aerosol activated fractions.

Compound	κ_{CCN}
NH_4NO_3	0.67
H_2SO_4	0.90
NH_4HSO_4	0.53
$(NH_4)_2SO_4$	0.61

For the organic material, a parametrization of κ_{CCN} based on the measured O/C ratio, introduced by Lambe et al. (2011), was used. The resulting organic κ_{CCN} values ranged between 0.079 and 0.205.

The differences between the κ values calculated for CCN activation and hygroscopic growth are of the order of 0.1 and much bigger than the differences between using and not using black carbon data and the organic density parametrization. Figure 4.6 exemplary shows data from 20 June to illustrate this.

Because the differences among the κ values for hygroscopic growth are smaller than the total variation and probably also smaller than the errors introduced by

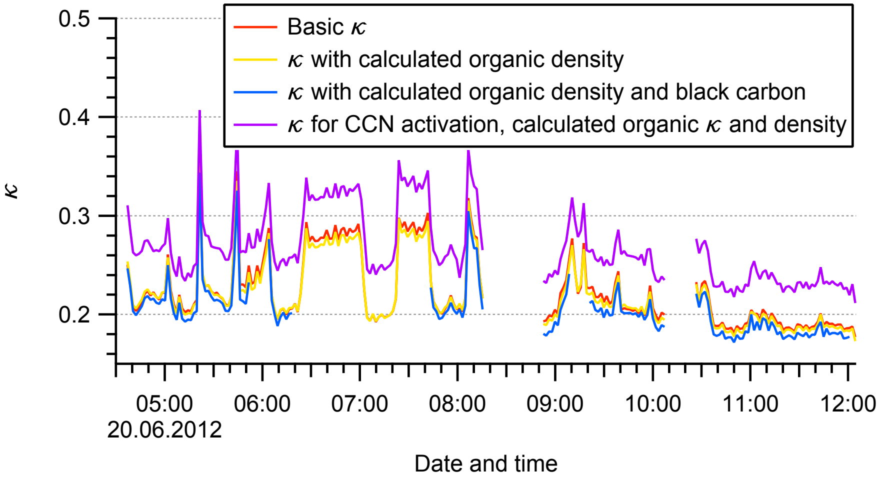

Figure 4.6.: κ calculated from AMS aerosol composition data and black carbon data on 20 June. A calculation with pure component κ values for hygroscopic growth, using a constant organic density of 1400 kg/m^3 yields the basic κ, shown in red. κ resulting from a calculation with parametrized organic density instead is shown in yellow. The κ shown in blue further includes black carbon data. The purple line shows κ for CCN activation instead of hygroscopic growth, including organic κ and density calculated from elemental composition data but excluding black carbon data.

the assumptions leading to the total κ calculation, κ including calculated organic density and omitting black carbon data is used from here on. This reduces the amount of data gaps.

4.3.1. Compound contributions to hygroscopicity

The calculated κ_{90} has an average of 0.25 with a standard deviation of 0.05 over the entire 2012 PEGASOS dataset. For the eastbound sub-campaign, the averaged κ is 0.30±0.03, whereas for the southbound sub-campaign it is 0.23±0.04. This significant difference can be explained by differences in the chemical composition shown in section 4.2. The higher concentration of nitrate in the eastbound campaign leads to a higher nitrate volume fraction. As all nitrate is assumed to be NH_4NO_3 with a κ_{90} value of 0.597, the average κ_{90} is expected to be higher.

The contributions of organics, the sulfates, and NH_4NO_3 to κ_{90} were calculated. Figure 4.7, Figure 4.9, and Figure 4.10 show the compound contributions to κ_{90}

for 21 May, 20 June, and 21 June, respectively.

For most of 21 May, a height profiling day in the eastbound campaign, the total κ_{90} was dominated by the contribution of nitrate. The total κ_{90} in the period of 11:00 UTC to 12:00 UTC is lowered, while the contribution of organics to κ_{90} is slightly raised and the sulfate contribution is significantly raised. The chemical composition on this day, shown in Figure 3.2 on page 51, exhibited a drop in nitrate concentration at this time. Because the organics concentration showed only a minor downward trend and the sulfate concentration was only slightly raised at this time, the consequence was a lowered nitrate mass fraction and an increased sulfate and organic mass fraction. The lowered nitrate mass fraction led to a lower volume fraction of NH_4NO_3. As this compound has a high κ_{90} value, the lack thereof led to a lowered total κ_{90}. The increased sulfate mass fraction however means that the volume fractions of sulfate-containing compounds increased. As these compounds have κ_{90} values almost as high as NH_4NO_3, this increase partially compensated the reduced the reduced NH_4NO_3 in the total κ_{90}. Because organics have a low κ_{90} value, the increase in organic mass fraction did not increase the total κ_{90} much.

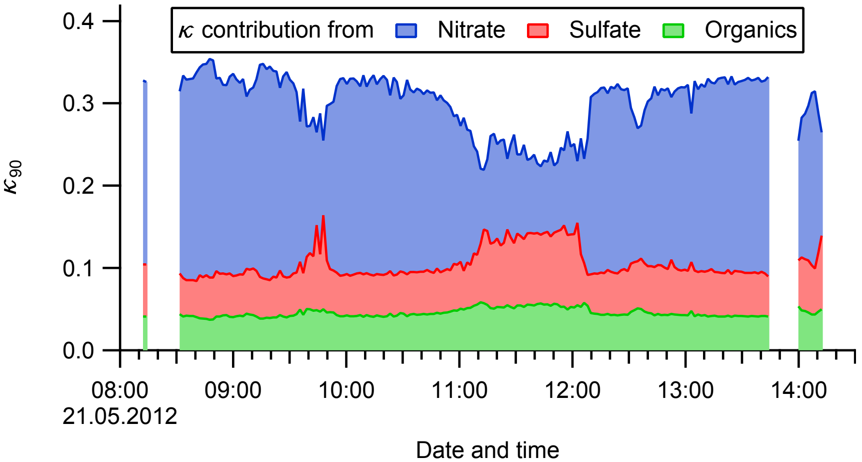

Figure 4.7.: Stacked display of nitrate, sulfate, and organics contribution to κ_{90} for 21 May.

To visualize the consequences of the variations in κ_{90}, the resulting variation in wet diameter particles of 300 nm dry diameter, exposed to 90 % relative humidity is shown in Figure 4.8 for 21 May. The wet diameter varied between 470 nm and 520 nm, equivalent to growth factors of 1.57 to 1.73. There is no directly apparent height dependence.

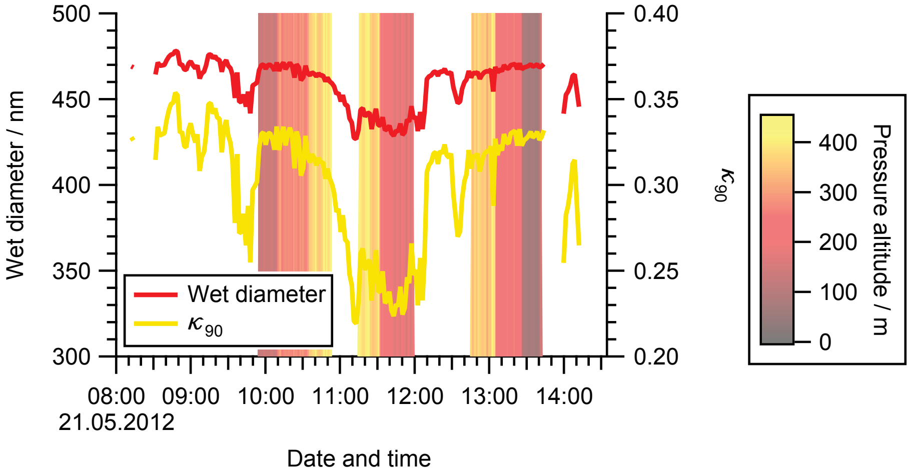

Figure 4.8.: Time series of calculated κ_{90} values and the corresponding wet diameter of a particle of 300 nm dry diameter exposed to 90 % relative humidity for 21 May. The background of the graph is shaded by altitude.

On 20 June, a height profiling day in the southbound campaign , the total κ_{90} (Figure 4.9) was most of the times lower than on 21 May. The variation was relatively large, particles measured in high altitude partly having a κ_{90} of more than 0.1 lower than on low altitude. On average, the highest contribution to total κ_{90} came from sulfate. As stated earlier and shown in Figure 3.4 on page 54, the height dependence of κ_{90} can be explained by lower nitrate mass concentrations at high altitudes. The drop in κ_{90} for high altitudes can thus be explained analog to the observed drop on 20 May, since the nitrate mass concentration again showed the highest variability, with organics and sulfate mass concentrations largely constant.

On 21 June, the calculated κ_{90} (Figure 4.10) was relatively constant except for three periods around 5:00 UTC, 8:30 UTC, and 10:00 UTC. These periods coincide with a rise in organics, nitrate, and sulfate concentrations, described in detail in subsection 3.2.2 starting on page 61. As nitrate was rising most, the mass fraction of organics and sulfate was effectively sinking, decreasing their contribution to the total κ_{90}. The total κ_{90} was elevated because of the rise in NH_4NO_3 volume fraction with its high pure compound κ_{90} value. As will be seen from section 4.5, the increased nitrate content is related to a longer residence time of the particles in the Po Valley. It is thus concluded, that processing of particles in an anthropogenically dominated environment leads to more hygroscopic particles.

Overall, the calculated κ_{90} seem to agree well with observations from previous

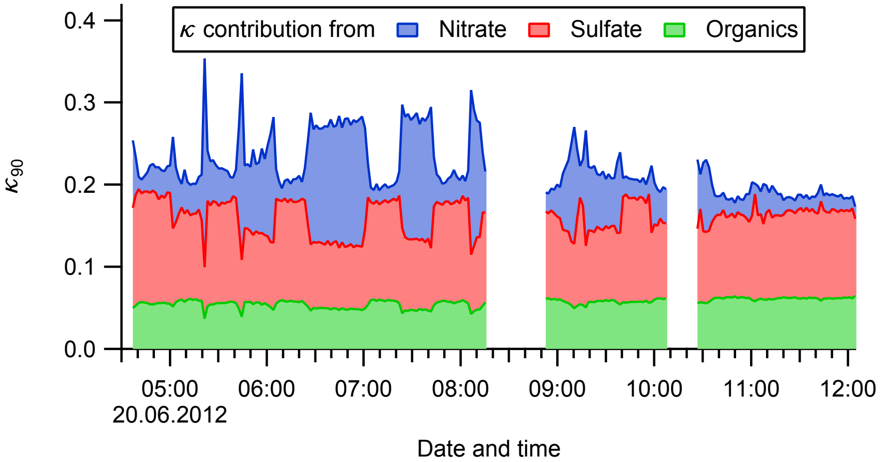

Figure 4.9.: Stacked display of nitrate, sulfate, and organics contribution to κ_{90} for 20 June.

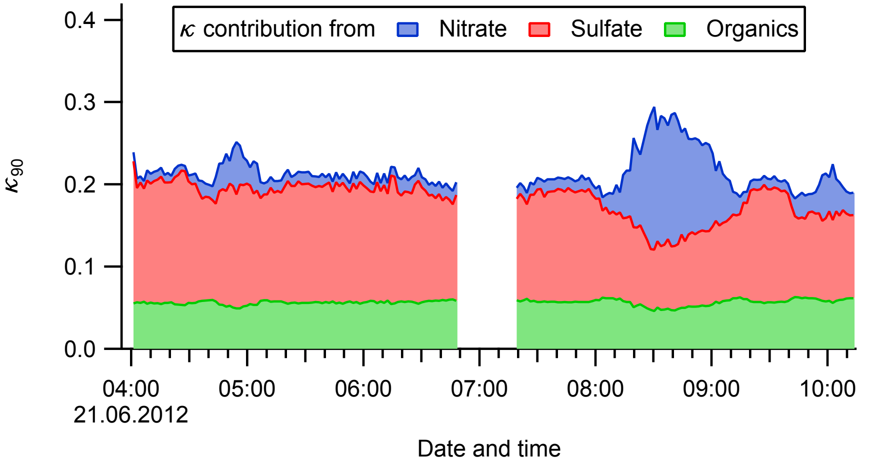

Figure 4.10.: Stacked display of nitrate, sulfate, and organics contribution to κ_{90} for 21 June.

field campaigns (Kammermann et al., 2010; Fors et al., 2011; Liu et al., 2011; Adam et al., 2012).

In conclusion, NH_4NO_3 is identified to be the component which controls the variability of the hygroscopic properties of sub-micron particles in the Netherlands as well as in the Po Valley. In the Po Valley, this dependency also leads to a lowered aerosol hygroscopicity in the upper layers of the PBL.

4.3.2. Predicted CCN activities of encountered aerosol

With κ calculated for CCN activation and a given saturation ratio, one can calculate the minimum dry diameter of a particle necessary to activate into a cloud droplet – equal to the critical dry diameter D_{crit} – from Equation 2.20.

$$D_{crit} = \frac{4 \cdot \sqrt[3]{4} \cdot M_w \sigma_w}{3 \cdot RT\rho_w \cdot \sqrt[3]{\kappa} \cdot (\ln(S_{crit}))^{\frac{2}{3}}} \qquad \text{(Equation 2.20)}$$

Applying D_{crit} to size distributions measured with the SMPS (subsection 2.3.1), the activated fraction a_f of particles was calculated as the ratio of particles bigger than D_{crit} to all measured particles.

For 22 May, a transect flight day in the eastbound campaign, a_f is shown together with D_{crit} in Figure 4.11.

On this day, a_f ranged between 0 and 0.21. Between 16:20 UTC and 16:40 UTC, the calculated D_{crit} dropped from approx. 162 nm to approx. 149 nm, while a_f rose from approx. 0.10 to approx. 0.20. This behaviour is expected, because with D_{crit} as threshold, a lower value means that for an unchanged particle size distribution, more particles are above the threshold and will be activated.

The data for 20 June, a height profiling day in the southbound campaign, is shown in Figure 4.12.

Both a_f and D_{crit} showed significant changes between low and high altitude. Exemplary, at 6:45 UTC, at low altitude, a_f was at 0.19 and D_{crit} at 160 nm. Half an hour later, on high altitude, a_f was at 0.31 and D_{crit} at 177 nm. On first sight, this observation contradicts the expectation of finding a lower a_f for a higher D_{crit}. An explanation can be found when looking at the particle number size distributions at these times (Figure 4.13).

At 6:45 UTC, there is a high concentration of small particles (Fig. 4.13a), effectively reducing a_f. At at 7:15 UTC however, the small particle concentration was significantly lower, therefore increasing a_f. Also, the reduced small particle concentration

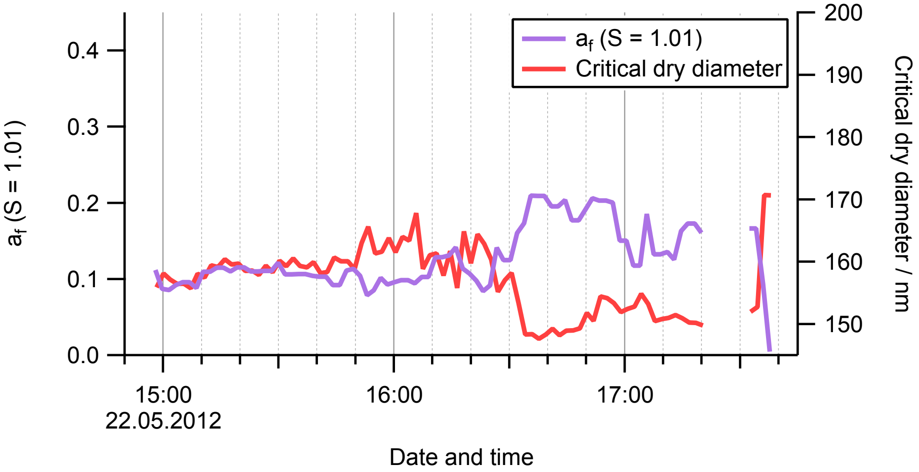

Figure 4.11.: Time series of activated fraction a_f and critical dry diameter for $S = 1.01$ on 22 May, a transect flight day in the Netherlands.

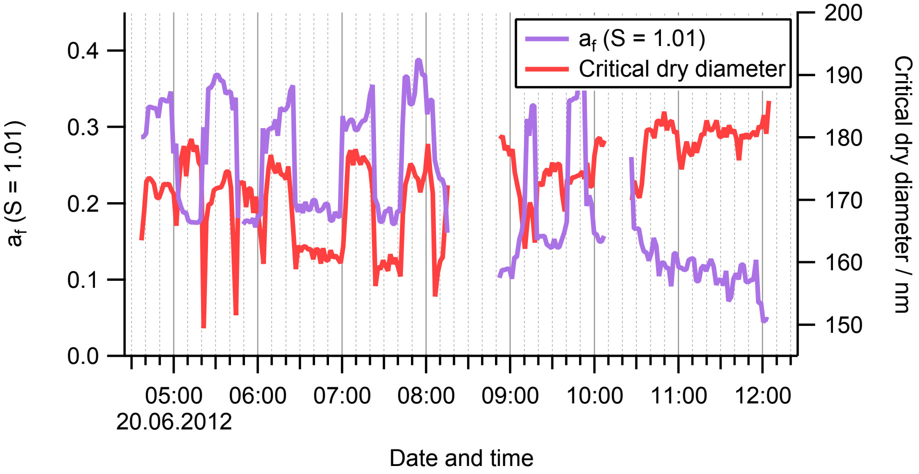

Figure 4.12.: Time series of activated fraction a_f and critical dry diameter for $S = 1.01$ on 20 June, a height profiling flight day in Italy.

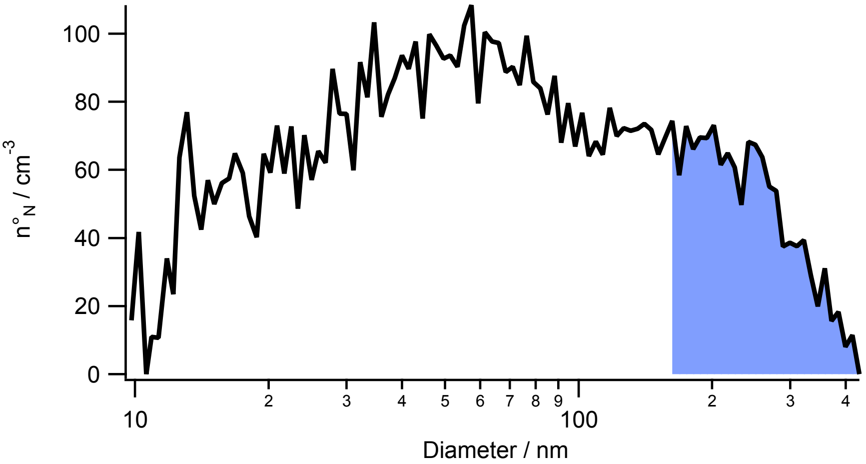

(a) 6:45 UTC: At this point, a_f is 0.19.

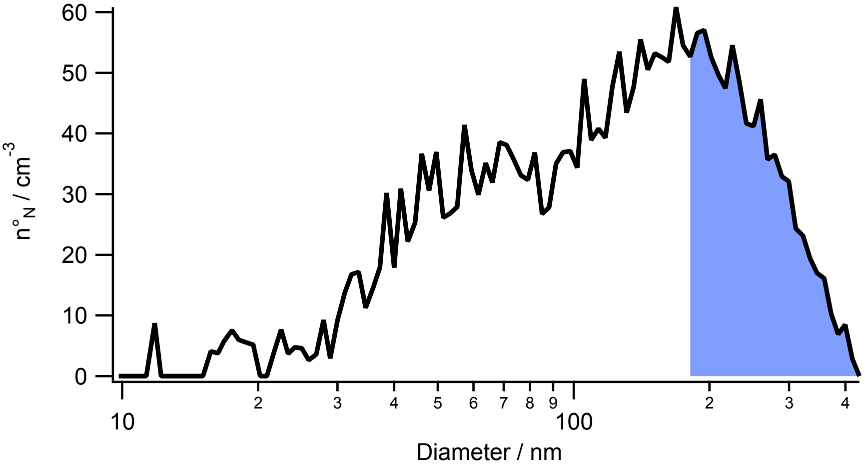

(b) 7:15 UTC: At this point, a_f is 0.31.

Figure 4.13.: Number-based aerosol size distributions at two times on 20 June. The part of the distribution with a diameter larger than D_{crit} is shaded in blue. The activated fraction a_f is the ratio between the blue area and the total area under the curve. Data for this graph was acquired with the SMPS in the CPN-Rack (subsection 2.3.1).

effected a reduced total number concentration. This in turn led to an overall drop in CCN concentration from 6:45 UTC to 7:15 UTC (see Figure 4.14). To summarize, the lower nitrate mass concentration on high altitude led to a reduced particle hygroscopicity, but the lowered total particle number concentration resulted in a net reduced CCN concentration on high altitude.

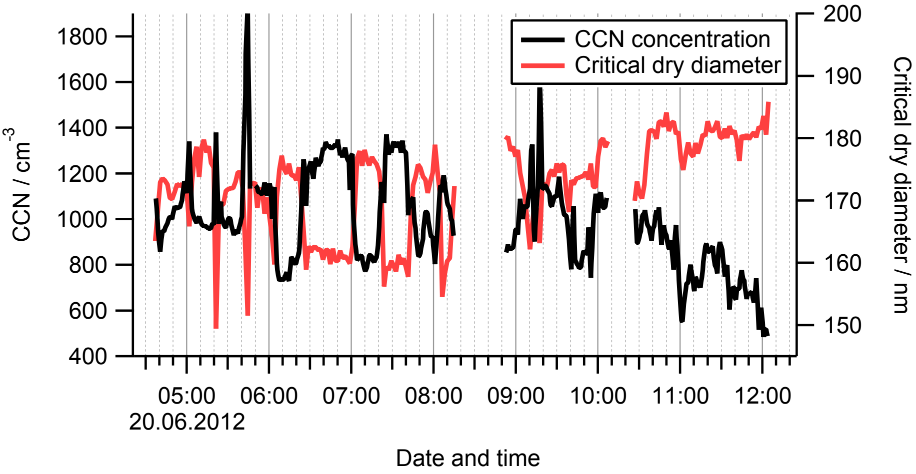

Figure 4.14.: Calculated CCN concentration and critical dry diameter for $S = 1.01$ on 20 June.

The data for 21 June, a transect flight day in the southbound campaign, is shown in Figure 4.15. Between 8:00 UTC and 9:30 UTC, the airship flew into an airmass with elevated aerosol concentrations. Because the contributions from organics and sulfate showed a different pattern than the contribution from nitrate, the shape of the time series of D_{crit} during this period resembles the letter M. The corresponding a_f time series is similar to the letter W, as would be expected for a situation with unchanged particle size distribution. The mean and median diameter of the particle size distribution (not shown) follow the shape of a_f, indicating that the trend in a_f originates in both the changes in D_{crit} and particle size distribution. The observations made between 4:30 UTC and 5:30 UTC, a first flight into the airmass with elevated aerosol concentrations, show a similar but less pronounced behaviour. Again, section 4.5 will show, that the changed CCN activity can be related to the aerosol residence time in the Po Valley.

In conclusion, the hygroscopicity parameter calculated from the chemical composition can be used to help separate the effects of a changing size distribution and a changing chemical composition on the CCN activity of an aerosol.

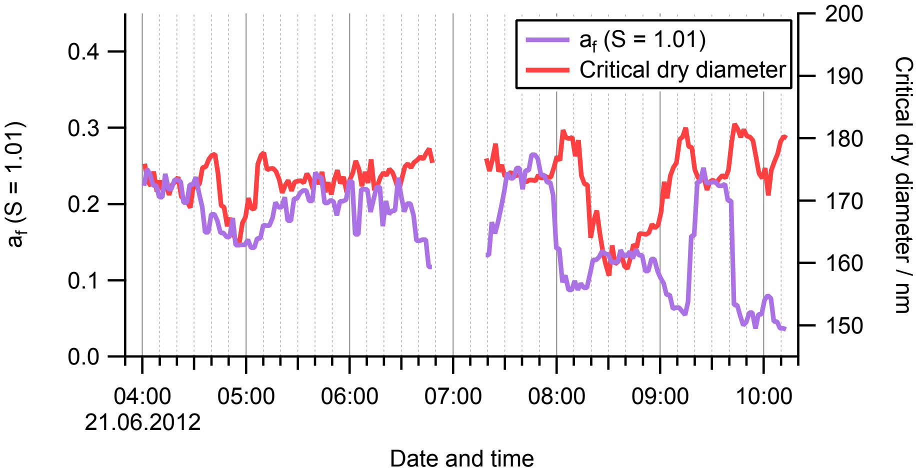

Figure 4.15.: Time series of activated fraction a_f and critical dry diameter for $S = 1.01$ on 21 June, a transect flight day in Italy.

4.4. Aerosol composition differences inside and outside of the mixing layer

During the eastbound and southbound PEGASOS campaigns, height profiles were achieved during three flights (section 3.1). On one more day (subsection 3.2.5), a two-level height profile was obtained.

On 21 May in the Netherlands, the airship reached maximum altitudes of around 400 m. The height profiling began at 10:00 UTC. Both particle composition (see Figure 3.2, Figure 3.3) and equivalent potential temperature θ_e (Figure 4.16) indicate, that the mixing layer was not left at that time. Diurnal cycles of monthly averaged mixing layer height measurements between 2000 and 2005 (De Haij et al., 2007, p. 51) show a typical mixing layer height of over 750 m for the time of day and year, in agreement with the current observations.

The three other height profile measurements were performed during the southbound PEGASOS campaign. Here, variable layered structures of the lower atmosphere were found. On 20 June, the height profiling was performed between 5:00 UTC and 12:00 UTC. In the early stages, θ_e observations indicate three distinctive layers in the covered altitude range. A lower unstable layer above the ground was followed by a relatively shallow stable layer, above which another unstable layer was located (see Figure 4.17).

In the course of the day, the stable layer lifted to higher altitudes and diminished

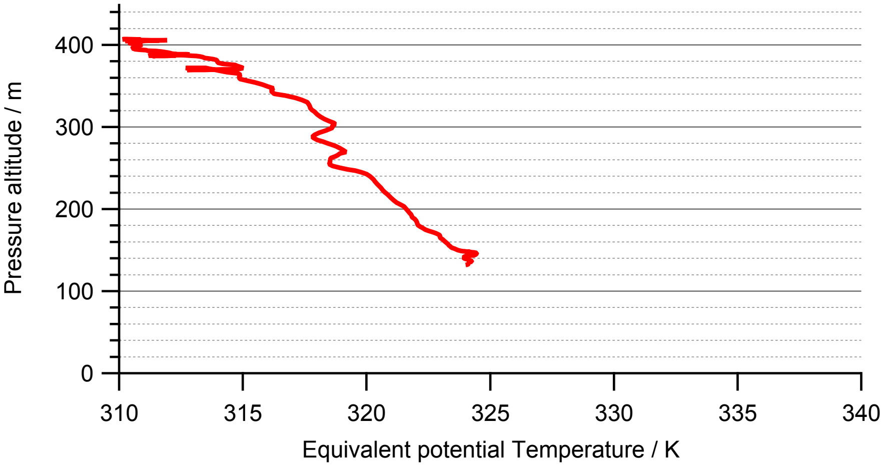

Figure 4.16.: Exemplary height profile of the equivalent potential temperature θ_e for **21 May**, obtained between 9:46 UTC and 9:51 UTC. No layering is apparent in the crossed altitude range.

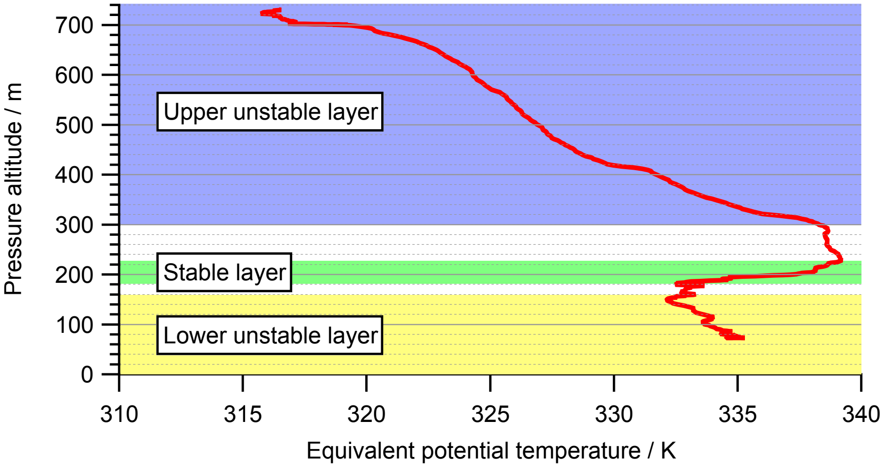

Figure 4.17.: Height profile of the equivalent potential temperature θ_e for **20 June**, obtained between 5:38 UTC and 5:46 UTC. The lower unstable layer (yellow shade) ranged up to 160 m. The stable layer above (green shade) was approximately 50 m deep. The upper unstable layer (blue shade) started at 300 m. Altitude ranges with white background can not unambiguously be attributed to one of the layers.

in depth (see Figure 4.18 and Figure 4.19).

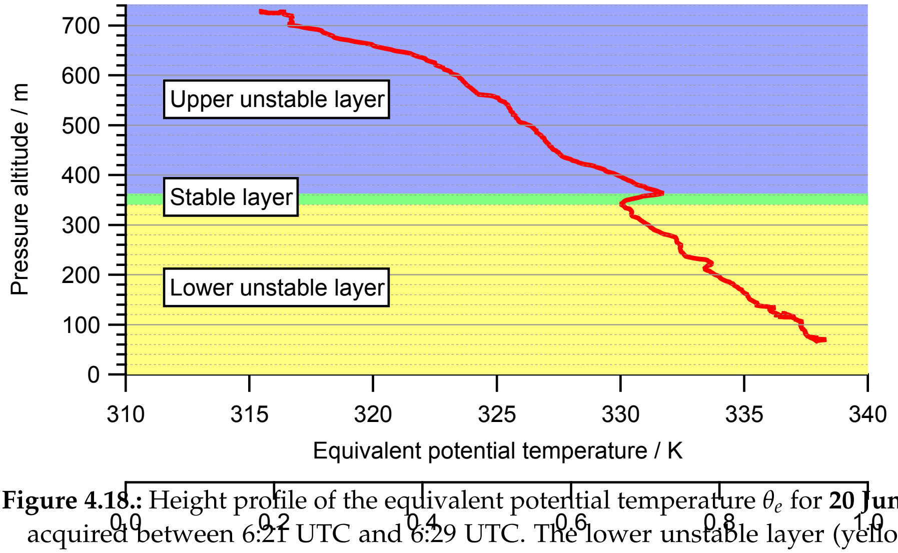

Figure 4.18.: Height profile of the equivalent potential temperature θ_e for **20 June**, acquired between 6:21 UTC and 6:29 UTC. The lower unstable layer (yellow shade) ranged up to 340 m. The stable layer above (green shade) was approximately 20 m deep. The upper unstable layer (blue shade) started at 360 m.

The distinction between the layers became less clear with progressing time of day. At the end of the flight day, the stable layer disappeared, leaving a single mixed layer over the whole altitude range. The lower unstable layer is interpreted as the newly evolving mixed layer. This layer grows during the morning until it is the only layer within the altitude range attained by the Zeppelin. The stable layer is likely the remainder of the nocturnal boundary layer. Data from the altitude range of this layer showed greatly increased aerosol concentrations (see subsection 3.1.3), supporting the interpretation as nocturnal boundary layer. The upper unstable layer is interpreted as residual layer, containing the constituents of the previous days mixed layer, further processed by night time chemistry.

The θ_e height profiles on 3 July (Figure 4.20) show a situation similar to 20 June, but without the stable layer.

The two layers found on 3 July are both unstable and are interpreted as mixed layer (1st unstable layer) and residual layer (2nd unstable layer). The altitude of sudden change in θ_e gradient is interpreted as border between the layers. Throughout the height profiling, the altitude of that border varied, but was surpassed whenever the airship flew on high altitude.

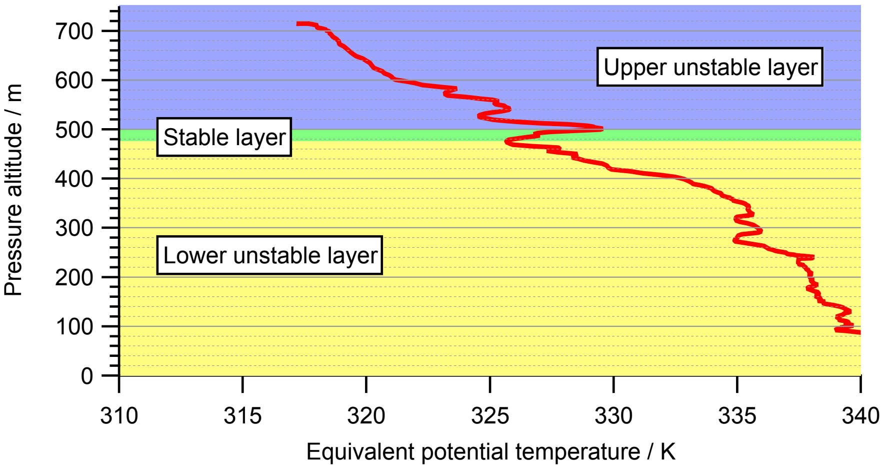

Figure 4.19.: Height profile of the equivalent potential temperature θ_e for **20 June**, acquired between 9:55 UTC and 10:00 UTC. The lower unstable layer (yellow shade) ranged up to 480 m. The stable layer above (green shade) was approximately 20 m deep. The upper unstable layer (blue shade) started at 500 m.

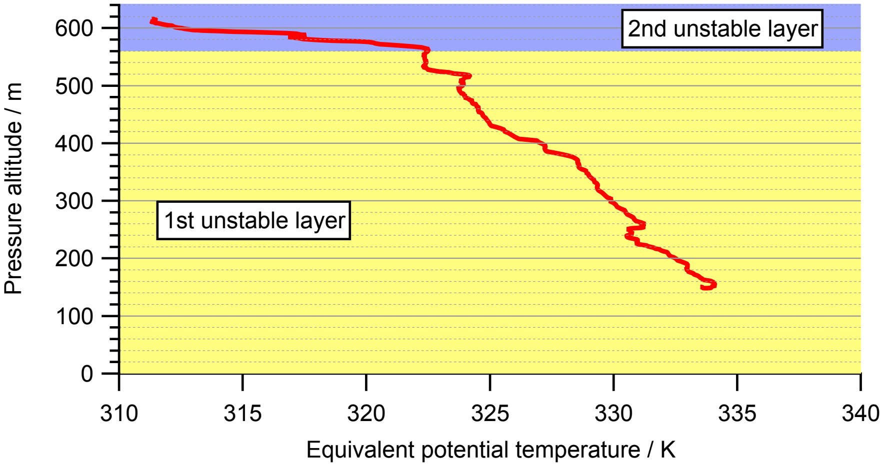

Figure 4.20.: Representative height profile of the equivalent potential temperature θ_e for **3 July**, acquired between 7:08 UTC and 7:12 UTC. Two different unstable layers were found, with the lower ranging to 560 m.

Comparing the observations in both layers, it becomes apparent that the overall aerosol concentration is reduced in the residual layer (see high altitude measurements shown in Figure 3.4 on page 54 and Figure 3.9 on page 58). Moreover, the relative composition is systematically different in the residual layer and in the mixed layer.

As shown in Figure 4.21, on both 20 June (Fig. 4.21a) and 3 July (Fig. 4.21b) the fraction of chloride and nitrate were lower in the residual layer than in the mixed layer near ground. The sulfate fractions were clearly elevated and the organics fractions were also increased.

The nitrate mass concentration was highly variably in the mixing layer and ranged between $0.5\,\mu g/m^3$ and $10\,\mu g/m^3$ on 20 June and between $0.2\,\mu g/m^3$ and $3\,\mu g/m^3$ on 3 July. The nitrate mass concentration was always low in the residual layer ($< 1\,\mu g/m^3$ for 20 June and $< 0.1\,\mu g/m^3$ for 3 July). The high variability in the mixed layer may be explained by the fact, that in addition to the typical aerosol loss processes, evaporation and dry deposition of NH_3 and HNO_3 play a role for ammonium nitrate (Larson and Taylor, 1983). Because the residual layer is disconnected from the ground level as soon as the nocturnal boundary layer is formed, thus isolated from sources of secondary aerosols, aerosol found here can be considered to be more aged due to a longer exposure time to the atmosphere. It reflects the photochemical processing during the previous day and potentially night time processing, especially of VOCs by ozonolysis. The low nitrate concentration in the residual layer is probably also related to low NO_x concentrations in these altitudes (see Figure 4.22).

The contributions of sulfate and organics to the total aerosol mass become clearer, when the highly variable nitrate and ammonium are taken out by forming the ratio of organics mass concentration to sulfate mass concentration (Org/SO_4). Org/SO_4 is shown in Figure 4.23.

Overall, Org/SO_4 was higher for 20 June than for 3 July. On both days, Org/SO_4 was systematically lower in the residual layer than near ground. A reason for this could be, that ammonium sulfate aerosol does not significantly evaporate (Drisdell et al., 2009), whereas organic aerosol is partly composed of semivolatile compounds that could evaporate, providing an additional loss path. A higher aerosol age inside the residual layer could lead to a further developed effect of evaporation (leaving the low volatile organics in the aerosol particles) and explain the lowered organics to sulfate ratio in high altitudes.

A higher aerosol age would also lead to a more oxidised organic aerosol. As discussed earlier, the the oxidation level of an organic aerosol can be expressed by the averaged carbon oxidation state $\overline{OS}_C$. Height profiles for 20 June and 3 July are shown in Figure 4.24.

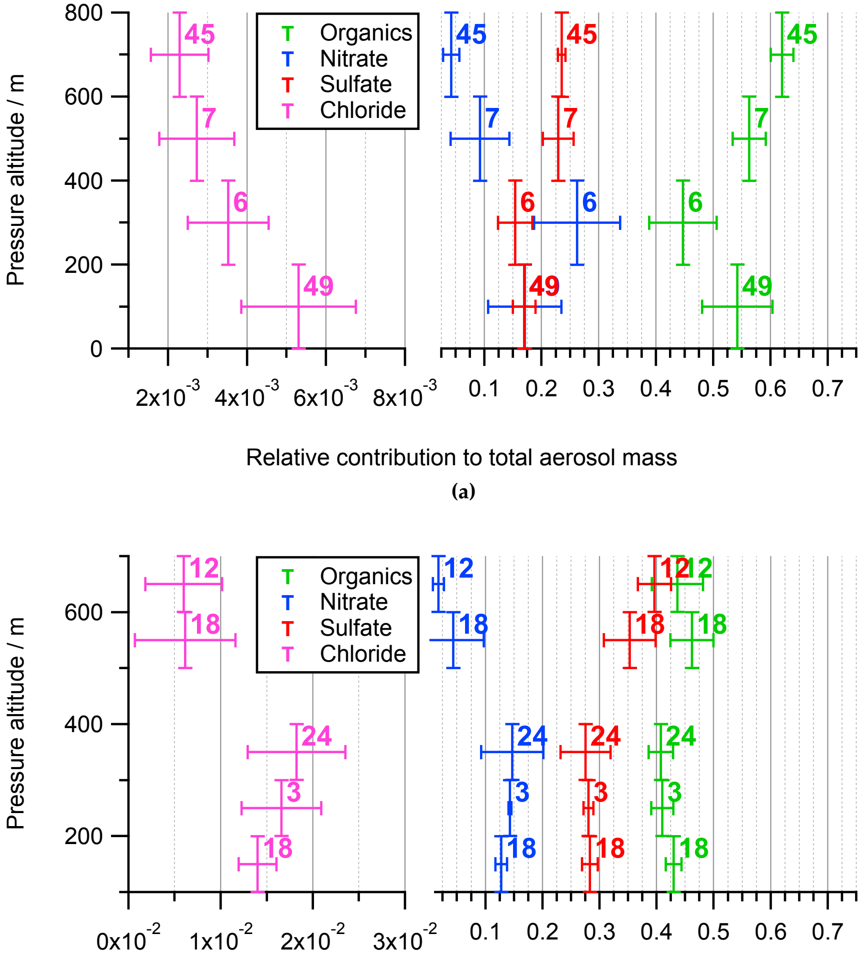

(a)

(b)

Figure 4.21.: Averaged height profiles of aerosol species relative concentration acquired on 20 June (Fig.4.21a) and 3 July (Fig.4.21b). The vertical error bars indicate the magnitude of the used altitude classes, whereas the horizontal error bars indicate the standard deviation of averaged points. The number of points averaged for each data point in this graph is indicated next to it.

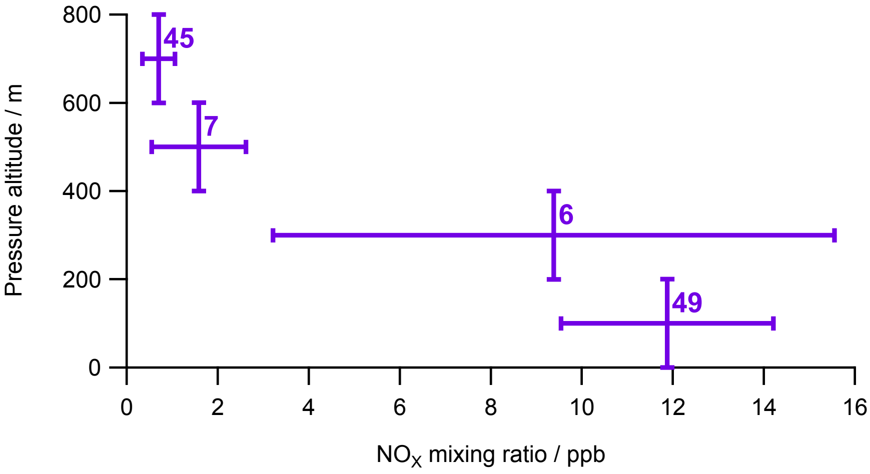

Figure 4.22.: Averaged height profile for NO_x on 20 June. Error bars and numbers as explained in the caption of Figure 4.21.

The $\overline{OS_C}$ values differ between the two days, but systematically higher values in the residual layer are discernible on both days. An increased $\overline{OS_C}$ corresponds to a higher oxidation level of the organic aerosol, confirming the postulated higher aerosol age.

The situation is different on 1 July. On this day, at least two unstable and two stable layers were found. A height profile of θ_e is shown in Figure 4.25. In analogy to the situations on 20 June and 3 July, the unstable layer at the ground ranging up to 120 m can be interpreted as the newly forming mixed layer evolving shortly after sunrise (3:34 UTC). Above that, a complex folding of the atmosphere is observed and no further attempts are made here to explain the origin of the respective layers. Note, that the layering in the altitude range labelled "1st stable layer" in Figure 4.25 could also be interpreted as two stable and one unstable layer. The uppermost layer however was stable, indicating a meteorologically different situation than on 20 June and 3 July.

The different meteorological situation was also reflected in the observed aerosol composition (see Figure 4.26). Instead of lowered nitrate relative concentrations and raised sulfate relative concentrations on high altitude, the opposite was observed. While the organic relative concentration was increased in high altitudes, as on the other days, Org/SO_4 was higher instead of lower compared to the low altitude observations. Also, the carbon oxidation state (not shown) indicated a less aged aerosol for high altitudes than for low altitudes.

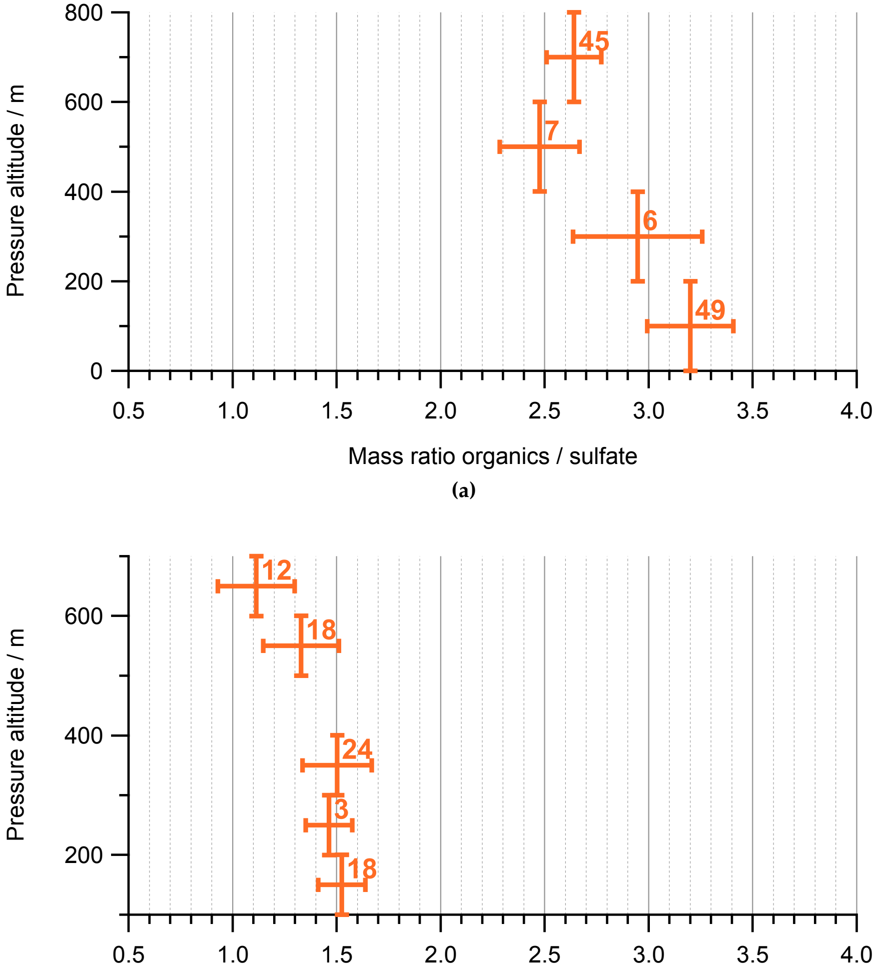

(a)

(b)

Figure 4.23.: Averaged height profiles of the organic to sulfate mass ratio as measured on 20 June (Fig. 4.23a) and 3 July (Fig. 4.23b). Error bars and numbers as explained in the caption of Figure 4.21.

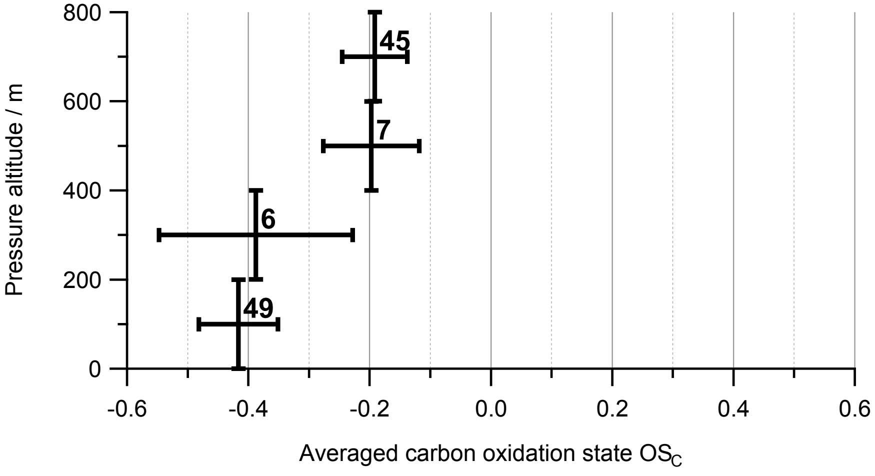

(a)

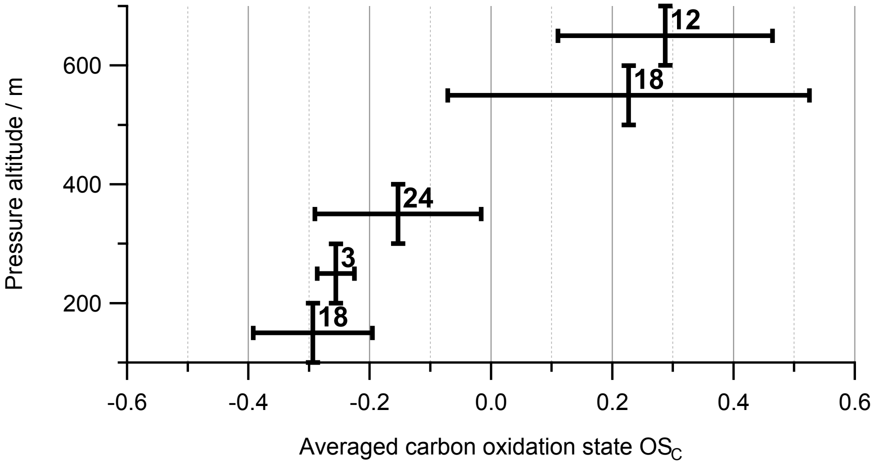

(b)

Figure 4.24.: Averaged height profiles of the averaged carbon oxidation state $\overline{OS_C}$ as measured on 20 June (Fig.4.23a) and 3 July (Fig.4.23b). Error bars and numbers are explained in the caption of Figure 4.21.

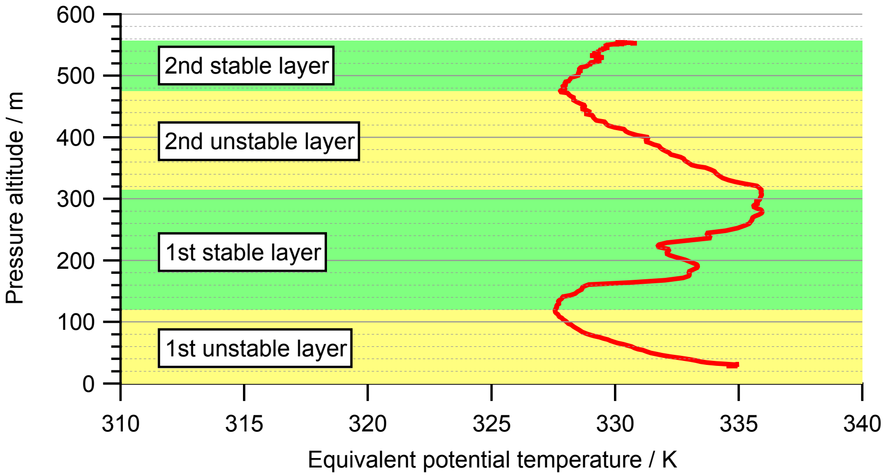

Figure 4.25.: Height profile of the equivalent potential temperature θ_e for **1 July**, acquired between 4:44 UTC and 4:49 UTC. An alternating pattern of unstable (yellow shade) and stable (green shade) layers was found in the crossed altitude range. The highest observed layer was stable.

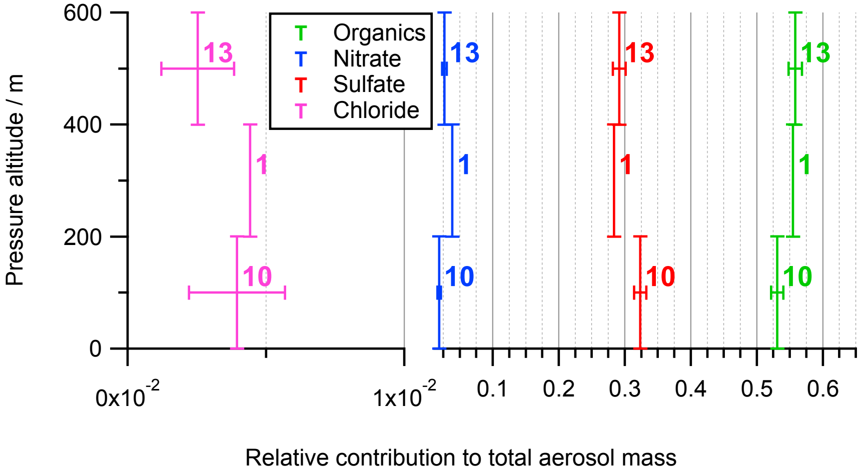

Figure 4.26.: Averaged height profiles of aerosol species relative concentration acquired on 1 July. Error bars and numbers as explained in the caption of Figure 4.21.

4.5. Local production vs. Transport

Due to the dynamic nature of the atmosphere and the lifetime of aerosol of the order of days, determining how much aerosol was formed in a given period of time at a specific location is difficult. A change of composition can arise from local production, or from pre-existing material that has been transported to the sampling site.

The Zeppelin based measurements on 21 June provide an opportunity to assess the local production of aerosol in the Po Valley. As described in subsection 3.2.2, north-south transects were performed on this day. In the northern part of the transects, elevated concentrations of particulate matter and gas phase constituents were found. Representatively, observations in the period from 7:25 UTC to 9:35 UTC are summarized in Figure 4.27.

Coincidental with the observed increase in particle mass concentration, the wind direction changed from southwest (~225°) to west by south (~260°). Also, the relative humidity increased from approximately 30 % to up to 55 %. The mean particle diameter measured by the SMPS in the CPN rack went down from 120 nm to below 80 nm. The averaged carbon oxidation state $\overline{OS}_C$ decreased from approximately 0.2 to approximately -0.3. All these changes indicate, that air masses of different history were sampled in the northern and the southern part of the flight track. Both the small median diameter and the low $\overline{OS}_C$ indicate, that the particles sampled in the region of higher concentration consist of more fresh particles than elsewhere.

The different shape of the NO_x profile compared to the aerosol profiles (Figure 4.27) originates in a discrete local NO_x source, the highway Autostrada A14, crossing the flight track near the turning point in the south, with prevailing wind from west by south. The aerosol however is thought to originate from secondary processes with extended sources westerly from the flight track.

The southwest wind direction in the southern part of the flight means, that the air sampled in this region was directly coming across the Apennines, whereas the more westerly wind direction in the northern part of the flight means, that the sampled air spent some time in the Po Valley. To get a more detailed analysis of the sampled air masses origins, backward trajectories trajectories were calculated using the HYSPLIT web-interface (Draxler and Hess, 1997) with meteorological data from GDAS (Parrish and Derber, 1992).

The south-north transect between 8:05 UTC and 8:35 UTC was used for the analysis. The backward trajectories were calculated for 24 h and chosen to end at 8:00 UTC. The trajectories are visualized in Figure 4.28. Regardless of the position of the

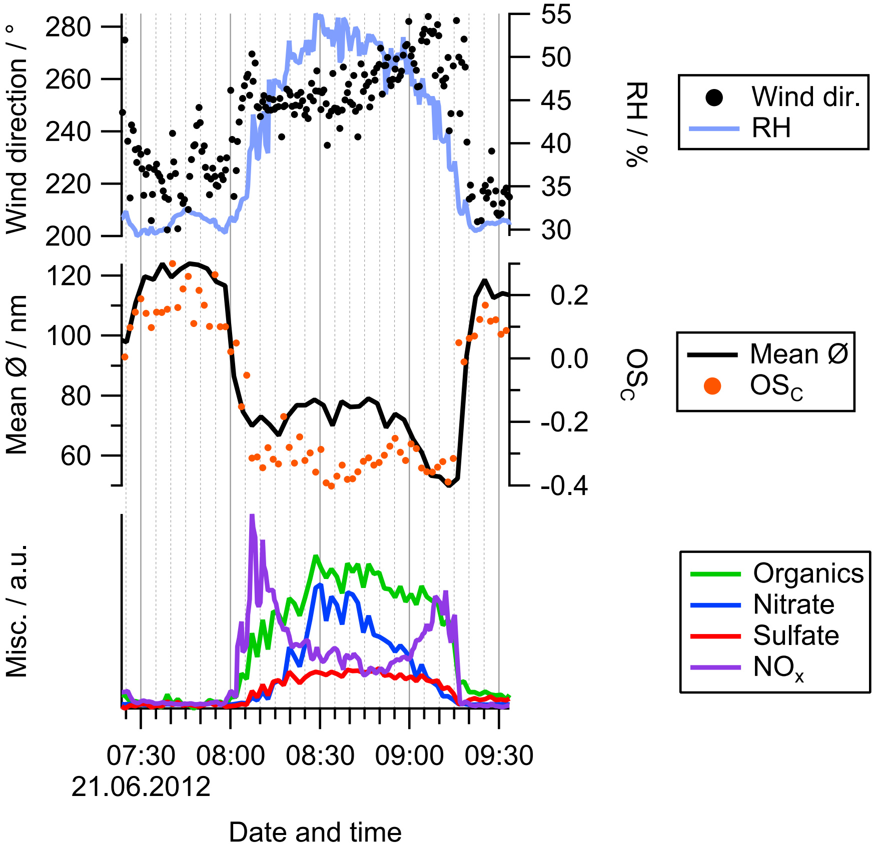

Figure 4.27.: Representative overview of the changes between south and north part of the flight on 21 June. At 8:00 UTC, the Zeppelin reached an airmass with higher aerosol concentration, turning to retrace its route at 8:35 UTC. The uppermost panel of the graph shows the wind angle as black dots and the relative humidity as light blue line. The middle panel shows the mean particle diameter as measured by the SMPS in the CPN rack in a black line and the averaged carbon oxidation state $\overline{OS}_C$ in orange dots. The lower panel shows the changes of selected aerosol components mass concentration and NO_x mixing ratio. The aerosol component mass concentrations are offset so their concentrations before 8:00 UTC fall on the same line. The NO_x mixing ratio is offset and scaled to allow display on the same axis.

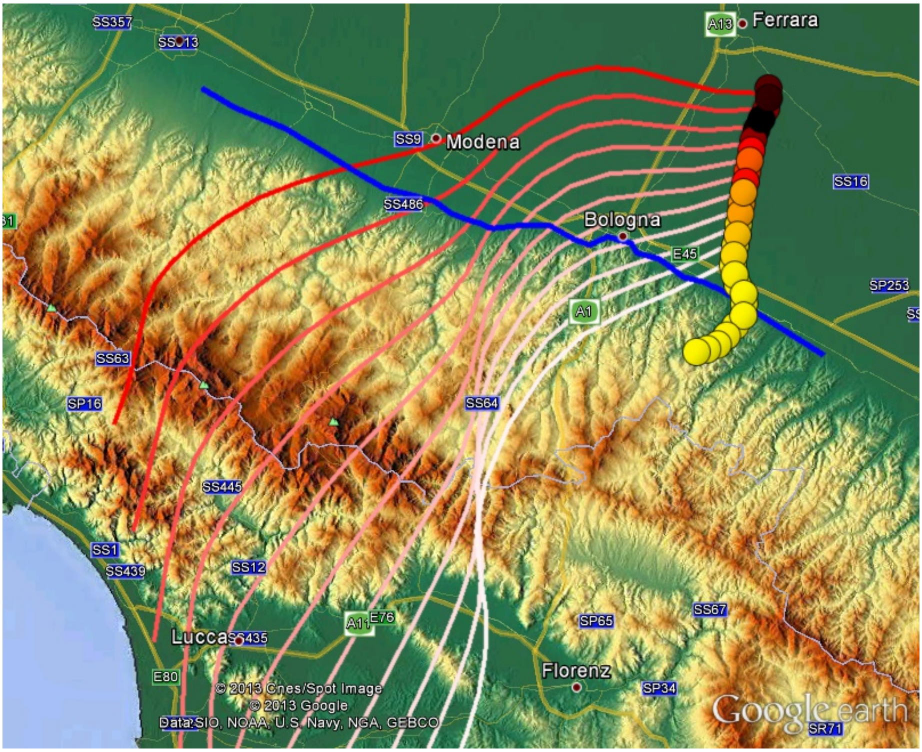

Figure 4.28.: Backward trajectories and measured data on a map detail of northern Italy. The blue line denotes the northern end of the Apennines, interpreted here as the 100 m contour line. The coloured circles represent the nitrate mass concentration measured on 21 June (7:45 UTC to 8:35 UTC), where lighter colours stand for lower concentration and darker colours for higher concentration. The lines in shades of red are 24 h backward trajectories ending at 8:00 UTC. The colour of the backward trajectories indicate the residence time of the respective air mass in the Po valley, with the lightest shade representing the shortest residence time and pure red representing the longest residence time.

Zeppelin along its flight track, the sampled air was coming from the Apennines within the previous 24 h.

The time the sampled air mass had spent in the Po Valley can be determined from the trajectories. For doing so, the border between Apennines and Po Valley is defined as the 100 m contour line here. The air mass residence time in the Po valley is then given by the time difference between the first trajectory data point within the Po valley and the trajectories ending time. Linear interpolation was used where the Apennines border lay between two data points. The resulting residence times span from approx. 0.6 h at the southern part of the flight track (8:05 UTC) to approx. 12.6 h at the northern tip of the flight track (8:35 UTC).

The observed mass concentrations of organic, nitrate, and sulfate aerosol are displayed as a function of the residence time in Figure 4.29.

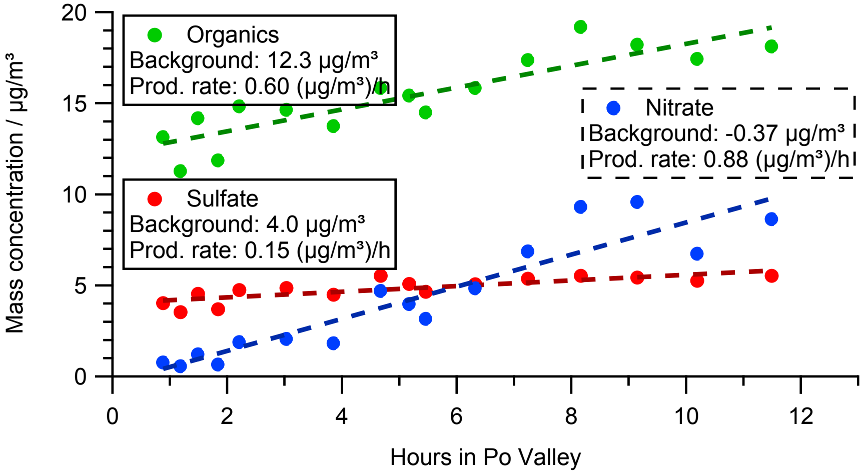

Figure 4.29.: Display of aerosol mass concentrations of organics (green), nitrate (blue) and sulfate (red) versus the time the sampled air mass had spent in the Po Valley according to HYSPLIT backward trajectories. Dashed lines represent a linear fit to the data. The intercept of the line fits represents the background mass concentration, the slope is equivalent to the aerosol production rate of the respective compound.

On first sight, linear relations with good Pearson R^2 values (organics 0.78, nitrate 0.87, sulfate 0.64) indicate, that there is a linear relation between mass concentration and Po Valley residence time. Assuming equal background concentrations for all sampled air masses when leaving the Apennines, the Po Valleys aerosol mass production rate can be calculated from the slope of aerosol mass concentrations as a function of air mass residence time. This approach implies on average uniform aerosol sources and sinks across the area and time span of the calculated trajectories within the Po Valley. The average aerosol formation rates are 0.60 (µg/m^3)/h for organic aerosol, 0.88 (µg/m^3)/h for nitrate aerosol, and 0.15 (µg/m^3)/h for sulfate aerosol.

Note that the sunrise was at approx. 3:30 UTC on this day and the measurements were performed around 8:30 UTC. Every change in aerosol concentration past the 5 h mark thus originates from night time chemistry. If night time chemistry would have a significantly different aerosol production rate than photochemistry, a significant change in slope from this point on would be observed. The good correlations for nitrate and organics speak against such a change in slope, and the data points in Figure 4.29 do not provide evidence either. For nitrate aerosol, a reason can be found in the night time production of its precursor nitric acid HNO_3 by the heterogeneous hydrolysis of N_2O_5. Vrekoussis et al. (2006) found, that 50 % to 65 % of the total HNO_3 formation can be assigned to night time production initiated by NO_3 radicals, giving night time chemistry a similar HNO_3 and nitrate aerosol production rate as daytime chemistry. For organic aerosol, an enhanced night time production by O_3 initiated VOC oxidation could be an explanation for the observed nearly constant aerosol production rate.

It has to be noted, that due to the specifics of the flight track, the calculated backward trajectories, and the Apennines border, anything with a linear gradient along the flight track would have a good correlation with the calculated residence time. Therefore, the scenario described here may not be the only cause for the observations. Nevertheless, the transport of pre-existing material as dominant source for change in the aerosol composition seems unlikely, as there is no apparent reason for transport processes along the calculated trajectories yielding the observed gradient along the flight track.

Focusing on the daytime aerosol production, comparisons of observed production rates and gas phase reactions as the source for secondary aerosol will be presented below.

For the formation of nitrate aerosol, nitric acid HNO_3 is needed. The HNO_3 formation rate $\frac{\mathrm{d}[\mathrm{HNO_3}]}{\mathrm{d}t}$ can be calculated from the concentrations of OH and NO_2 (measured by instruments in the Top-Platform and in the NOX-Rack, respectively), using the rate constant $k_{\mathrm{OH+NO_2}}$.

$$\mathrm{NO_2} + \mathrm{OH} \xrightarrow{k_{\mathrm{OH+NO_2}}} \mathrm{HNO_3} \tag{4.1}$$

$$\frac{\mathrm{d}\left[\mathrm{HNO_3}\right]}{\mathrm{d}t} = k_{\mathrm{OH+NO_2}} \cdot [\mathrm{NO_2}] \cdot [\mathrm{OH}] \tag{4.2}$$

The temperature and pressure dependent $k_{\mathrm{OH+NO_2}}$ was taken from the Master Chemical Mechanism, MCM v3.2 (Jenkin et al., 1997; Saunders et al., 2003), via website: `http://mcm.leeds.ac.uk/MCM`, based on Hippler et al. (2006), Troe (2001), and D'Ottone et al. (2001).

The reaction of VOCs with OH to oxidised volatile organic compounds OVOC is a daytime source of SOA. A generalised reaction can be formulated as shown in Equation 4.3.

$$\mathrm{VOC} + \mathrm{OH} \xrightarrow{k_{\mathrm{OH+VOC}}} \mathrm{OVOC} \tag{4.3}$$

The OVOC formation rate is then given by Equation 4.4.

$$\frac{\mathrm{d}\,[\mathrm{OVOC}]}{\mathrm{d}t} = k_{\mathrm{OH+VOC}} \cdot [\mathrm{OH}] \cdot [\mathrm{VOC}] \tag{4.4}$$

The OH reactivity due to VOCs k_{VOC}, which is the inverse of the lifetime of OH in the presence of the given amount of VOC, can be expressed as in Equation 4.5.

$$k_{\mathrm{VOC}} = k_{\mathrm{OH+VOC}} \cdot [\mathrm{VOC}] \tag{4.5}$$

Inserting Equation 4.5 in Equation 4.4 yields Equation 4.6.

$$\frac{\mathrm{d}\,[\mathrm{OVOC}]}{\mathrm{d}t} = k_{\mathrm{VOC}} \cdot [\mathrm{OH}] \tag{4.6}$$

Top-Platform measurements of total OH reactivity k_{OH} can be understood as sum of the reactivities from CO, $\mathrm{NO_2}$, NO, and VOCs (k_{CO}, $k_{\mathrm{NO_2}}$, k_{NO}, and k_{VOC}, respectively).

$$k_{\mathrm{OH}} \approx k_{\mathrm{CO}} + k_{\mathrm{NO_2}} + k_{\mathrm{NO}} + k_{\mathrm{VOC}} \tag{4.7}$$

Because k_{OH} is measured and k_{CO}, k_{NO_2}, and k_{NO} can be calculated from measured concentrations of the respective compounds and known rate constants for their reaction with OH (taken from the Master Chemical Mechanism, MCM v3.2 (Jenkin et al., 1997; Saunders et al., 2003), values based on Forster et al. (1995) and Fulle et al. (1998)), k_{VOC} can be calculated. This enables the calculation of the total OVOC production rate $\frac{\mathrm{d[OVOC]}}{\mathrm{d}t}$ according to Equation 4.6. Another source of SOA during day and night is the ozonolosys.

To compare to mass based aerosol production rates, the molecule-based rates $\frac{\mathrm{d}[\mathrm{HNO_3}]}{\mathrm{d}t}$ and $\frac{\mathrm{d[OVOC]}}{\mathrm{d}t}$ need to be converted into mass based rates using molecular masses. For the OVOCs, a molecular mass MW of 150 g/mol is assumed. The values calculated in this manner represent the total amount of material produced. A fraction Y of this total material is transferred into the particulate phase. When a $Y_{\mathrm{HNO_3}}$ of 14 % is assumed for HNO_3 and a Y_{OVOC} of 1.4 % is assumed for OVOC, the calculated production rates matched the observed rates within the air mass coming from the Po Valley. This is illustrated in Figure 4.30.

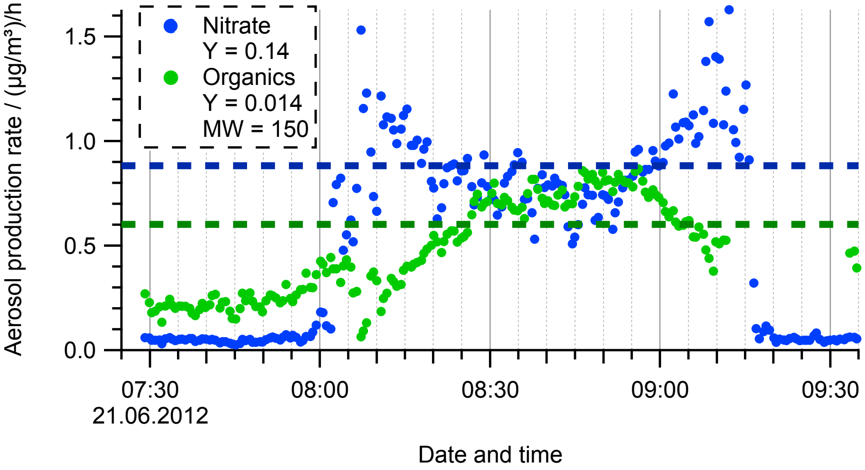

Figure 4.30.: Theoretical aerosol production rates for nitrate (blue dots), assuming a HNO_3 particle yield of 14 %, and for organics (green dots), assuming a VOC molecular mass of 150 g/mol and a particle yield of 1.4 %. The dashed lines indicate the aerosol production rates found in Figure 4.29.

The transfer of HNO_3 to the particle phase is determined by the availability of NH_3, which limits the formation of NH_4NO_3, the most likely form of nitrates found in the aerosol. The temperature plays another role, because an NH_4NO_3 aerosol can evaporate via the decay to NH_3 and HNO_3 (Tang, 1980). These contributions could lead to a $Y_{\mathrm{HNO_3}}$ lower than one.

For the oxidation of VOCs, a particle yield comparable to Y_{OVOC} can be determined as a function of aerosol concentration. Using the dependency Emanuelsson et al. (2013) determined in a study of various aromatic VOCs, an expected yield of approximately 15 % results for the observed particle mass concentration. Although the VOC mixture found in the Po Valley is not consisting solely of aromatic compounds and the ambient temperature was significantly higher than in the study of Emanuelsson et al. (2013), this value serves as an orientation point. To explain the much lower Y_{OVOC} calculated for 21 June, the VOC reactivity would have to originate mostly from compounds which do not act as SOA precursors. Preliminary results of gas chromatographic measurements performed with the HGC rack (Wegener and Jäger, 2013) do indicate, that the reactivity of the VOC mixture was dominated by short-chained OVOCs fulfilling this criterion and only small amounts of classical SOA precursors like monoterpenes and longer-chained OVOCs were found.

4.6. Aerosol ion balance

The inorganic species detected by the AMS can be classified into anions ($\mathrm{NO_3^-}$, $\mathrm{SO_4^{2-}}$, $\mathrm{Cl^-}$) and cations ($\mathrm{NH_4^+}$). Substances containing alkali metal or alkaline earth metal cations typically have a too high evaporation temperature to be vaporized at the vaporizer temperature of 600 °C. The contribution of $\mathrm{H^+}$ to the ion balance cannot be directly quantified with the AMS. Assuming a neutral aerosol , the molar concentration of $\mathrm{NH_4^+}$ should be at most the amount required to form $\mathrm{NH_4NO_3}$, $\mathrm{(NH_4)_2SO_4}$ and ammonium chloride $\mathrm{NH_4Cl}$ from the available anionic species. Any lower concentration of $\mathrm{NH_4^+}$ indicates an acidic aerosol, charge neutralized by $\mathrm{H^+}$. However, measurements performed in the Netherlands showed significantly more $\mathrm{NH_4^+}$ than the measured negative ions can accommodate.

In the following equation, the excess $\mathrm{NH_4^+}$ mass concentration is expressed as $e_{\mathrm{NH_4^+}}$.

$$e_{\mathrm{NH_4^+}} = MW_{\mathrm{NH_4^+}} \cdot \left[n_{\mathrm{NH_4^+}} - \left(n_{\mathrm{NO_3^-}} + n_{\mathrm{Cl^-}} + 2 \cdot n_{\mathrm{SO_4^{2-}}} \right) \right] \tag{4.8}$$

In Equation 4.8, n_i stands for the molar concentration of species i and $MW_{\mathrm{NH_4^+}}$ for the molar mass of $\mathrm{NH_4^+}$.

For the 2012 PEGASOS campaign, $e_{\mathrm{NH_4^+}}$ is displayed on a day by day basis in Figure 4.31. Measurements in the Netherlands (21 May and 22 May) show an

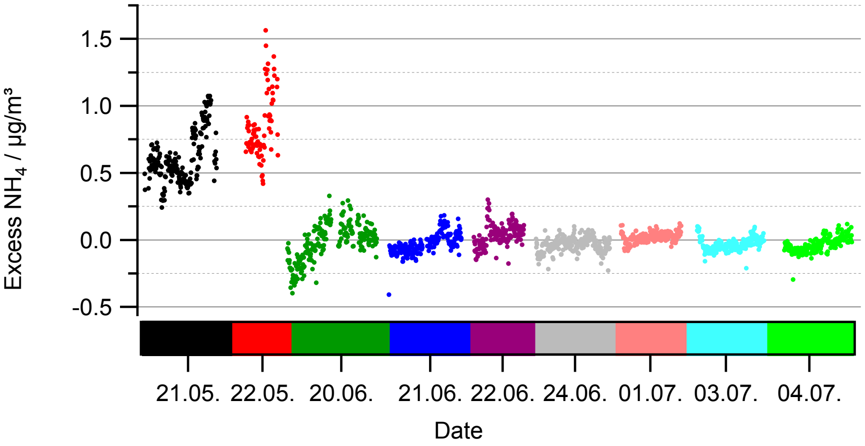

Figure 4.31.: Mass concentration of ammonium in excess to all measured anionic inorganic species. Measurements in the Netherlands (21 May and 22 May) show up to 1.5 µg/m^3 excess ammonium, whereas measurements in Italy (20 June to 4 July) mainly show values around zero, between -0.25 µg/m^3 and 0.25 µg/m^3.

average of 0.68 µg/m^3 excess ammonium, equivalent to 14 % of the amount necessary to neutralize nitrate, sulfate and chloride. The absolute maximum lies at 1.5 µg/m^3, the relative maximum at 20 %. These findings are in qualitative agreement with ground based long term observations made in Cabauw, NL (Mensah et al., 2012). In contrast to that, measurements in Italy (20 June to 4 July) show $e_{\mathrm{NH}_4^+}$ values around zero. Negative values in this period indicate aerosol neutralization by H^+, thus an acidic aerosol.

Measurements of ammonia NH_3 in the Netherlands have shown mean annual gas phase concentrations in a range of 2 µg/m^3 to 23 µg/m^3 in the past (Eerden et al., 1998), almost exclusively originating from agriculture, of which emissions from animal faeces contribute the largest portion (Hoek, 1998). The NH_3 emission rates in the Netherlands are among the highest in the world (Bouwman et al., 1997). However, to end up as ammonium in particulate matter, NH_3 has to form a salt like compound with sufficiently low saturation vapour pressure. All inorganic negative ions of mineral acids are by definition already accounted for in the calculation of $e_{\mathrm{NH}_4^+}$. This leaves the organic material as possible reaction partner.

A binding of NH_3 by organics could be possible via an acid-base reaction with carboxyl groups. This is supported by a good correlation between the molar concentration of excess ammonia $n_{e_{\mathrm{NH}_4^+}}$ and the organic CO_2 molar concentration during the measurements in the Netherlands. The correlation has a Pearson R^2 coefficient of 0.59 (see Figure 4.32).

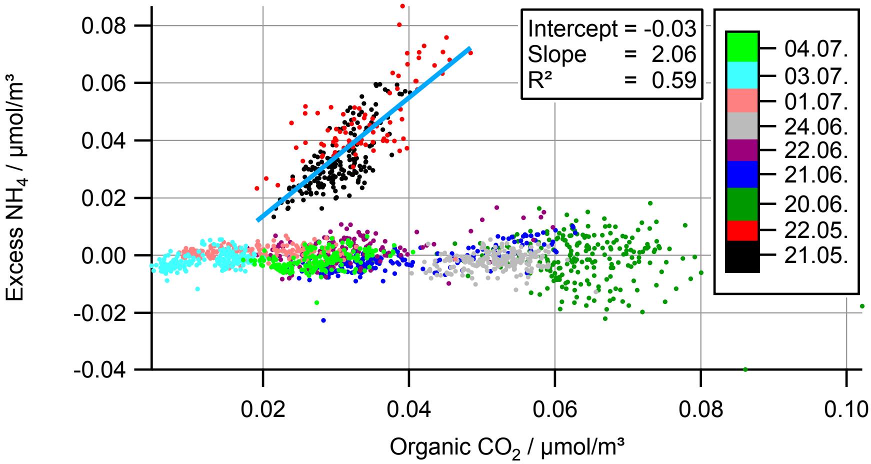

Figure 4.32.: Molar concentration of excess ammonia $n_{e_{\mathrm{NH}_4^+}}$ versus organic CO_2 molar concentration as measured during the 2012 PEGASOS campaign. For measurements in the Netherlands, a correlation was observed. Measurements in Italy showed no significant $n_{e_{\mathrm{NH}_4^+}}$ over a wide range of organic CO_2 concentrations.

A simple variation in gas-phase NH_3 concentrations could explain the varying $e_{\mathrm{NH}_4^+}$, but not its correlation with measured organic CO_2. A strong variation in gas-phase CO_2 simultaneous with the NH_3 variation could explain the good correlation, conceivable as a source region with co-located combustion and NH_3 emissions. Because there was no independent CO_2 measurement aboard the airship, the correction for gas-phase CO_2 had to be done with a constant apparent CO_2 concentration derived from measurements with a particle filter in the sampling line before, during, and after the flights. Although the individual filter measurements point to no variation in gas-phase CO_2 concentrations and gas phase CO do not suggest combustion influence, effects by gaseous CO_2 cannot be unambiguously excluded. For the remainder of this section, the $e_{\mathrm{NH}_4^+}$ is assumed to be exclusively originating from variations in the organic aerosol carboxylic acid content.

Assuming that each NH_4^+ is bound by one carboxyl group in the deprotonated form, the mass concentration of carboxyl groups m_{COO^-} can be calculated from

$n_{e_{\mathrm{NH}_4^+}}$ and the molecular weight of the carboxyl anion MW_{COO^-}.

$$m_{\mathrm{COO}^-} = n_{e_{\mathrm{NH}_4^+}} \cdot MW_{\mathrm{COO}^-} \tag{4.9}$$

Because the thermal processes in the aerosol mass spectrometer are thought to yield equal amounts of CO_2 and CO from carboxylic acid groups (Aiken et al., 2008), equimolar amounts of excess ammonium ions and carboxylic acid groups will lead to a slope of 2 for the organic CO_2 molar concentration expressed as function of $n_{e_{\mathrm{NH}_4^+}}$. The observed slope of 2.06 (Figure 4.32) agrees with the theoretical value. However, an error compensation leading to this slope cannot be excluded. If more than one carboxyl group has to be available to bind one NH_3 (because of a low acid strength of the organic acids in question), m_{COO^-} would be underestimated. Possible interference by a significant portion of acidic hydroxyl groups also binding NH_3 is unlikely, but would lead to an overestimation of m_{COO^-}.

The good agreement of the slope found for the dependency of $n_{e_{\mathrm{NH}_4^+}}$ on organic CO_2 with the theoretical value encouraged taking the analysis one step further. Based on a molar ratio of one between NH_4^+ an COO^-, the functional group composition in addition to carboxylic acid groups can be analysed. For that, it is assumed here, that the only heteroatom present in the organic aerosol is oxygen. The mass concentration of organic aerosol m_{Org} can then be expressed as in the sum of m_{COO^-} and contributions from unknown molar amounts of oxygen (n_{O}), carbon (n_{C}), and hydrogen (n_{H}).

$$m_{Org} = m_{\mathrm{COO}^-} + n_{\mathrm{O}} \cdot MW_{\mathrm{O}} + n_{\mathrm{C}} \cdot MW_{\mathrm{C}} + n_{\mathrm{H}} \cdot MW_{\mathrm{H}} \tag{4.10}$$

In Equation 4.10, the molecular masses of oxygen, carbon, and hydrogen are written as MW_{O}, MW_{C}, and MW_{H}, respectively.

The measured elemental composition of the organic aerosol can serve as additional constraint for n_{O}, n_{C}, and n_{H}. To match the atomic O/C and H/C ratios, n_{O}, n_{C}, and n_{H} are to be added to the contribution from the carboxylic acid groups (molar concentration n_{COO^-}).

$$O/C = \frac{2 \cdot n_{\mathrm{COO}^-} + n_{\mathrm{O}}}{n_{\mathrm{COO}^-} + n_{\mathrm{C}}} \tag{4.11}$$

$$H/C = \frac{n_{\mathrm{H}}}{n_{\mathrm{COO}^-} + n_{\mathrm{C}}} \tag{4.12}$$

Using the equations Equation 4.10, Equation 4.11, and Equation 4.12, analytical expressions for n_O, n_C, and n_H can be found in Equation 4.13, Equation 4.14, and Equation 4.15, respectively.

$$\begin{aligned} n_\mathrm{O} = {} & (O/C-2)\cdot n_{\mathrm{COO}^-} + O/C\cdot \\ & \frac{m_{Org} - m_{\mathrm{COO}^-} - (O/C-2)\cdot MW_\mathrm{O}\cdot n_{\mathrm{COO}^-} - H/C\cdot MW_\mathrm{H}\cdot n_{\mathrm{COO}^-}}{O/C\cdot MW_\mathrm{O} + MW_\mathrm{C} + H/C\cdot MW_\mathrm{H}} \end{aligned} \tag{4.13}$$

$$n_\mathrm{C} = \frac{m_{Org} - m_{\mathrm{COO}^-} - (O/C-2)\cdot MW_\mathrm{O}\cdot n_{\mathrm{COO}^-} - H/C\cdot MW_\mathrm{H}\cdot n_{\mathrm{COO}^-}}{O/C\cdot MW_\mathrm{O} + MW_\mathrm{C} + H/C\cdot MW_\mathrm{H}} \tag{4.14}$$

$$\begin{aligned} n_\mathrm{H} = {} & H/C\cdot n_{\mathrm{COO}^-} + H/C\cdot \\ & \frac{m_{Org} - m_{\mathrm{COO}^-} - (O/C-2)\cdot MW_\mathrm{O}\cdot n_{\mathrm{COO}^-} - H/C\cdot MW_\mathrm{H}\cdot n_{\mathrm{COO}^-}}{O/C\cdot MW_\mathrm{O} + MW_\mathrm{C} + H/C\cdot MW_\mathrm{H}} \end{aligned} \tag{4.15}$$

The resulting values can be visualized by a hypothetical average molecular unit, containing one carboxylic acid group. Dividing n_O, n_C, and n_H by n_{COO^-} yields the elemental composition of such units, disregarding the carboxylic acid group itself. For 21 May, the calculated values are shown in Figure 4.33.

For example at 9:00 UTC, the molecular formula of each unit was approximately $C_{19}H_{30}O_6$ (plus COO^-). This would mean, that per carboxylic acid group, there were 19 additional carbon atoms, of which 6 bore an oxygen containing functional group. At 13:30 UTC, it was approximately $C_{12}H_{20}O_3$ (plus COO^-). The latter can be interpreted as a more acidic organic aerosol compared to the former. If the units would be interpreted as representative molecules, the more acidic aerosol would be consisting of shorter chained carboxylic acids. As organic aerosol consists of many different compounds, other possibilities can also explain the changed unit composition, e. g. a higher content of molecules containing one or more carboxylic acid groups. In any case, the higher organic aerosol acidity in the afternoon agrees with the higher photochemical age of the measured aerosol.

The calculated unit composition for 22 May is shown in Figure 4.34. At 15:30 UTC, the unit molecular formula was $C_{17}H_{27}O_5$ (plus COO^-). Within the uncertainties of the method developed here, this composition is probably identical to the composition found at 9:00 UTC of 21 May. At 16:45 UTC on 22 May, the unit molecular formula was $C_8H_{13}O_3$ (plus COO^-), one of the smallest units found in the analysed data. At the time of observation, the airship was over the sea, with

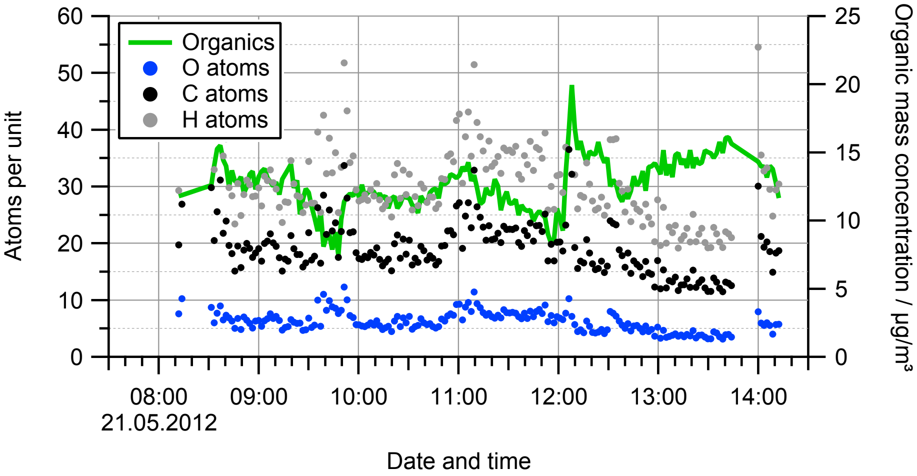

Figure 4.33.: Time series of organic aerosol mass concentration and calculated elemental composition for units containing one carboxylic acid group for 21 May.

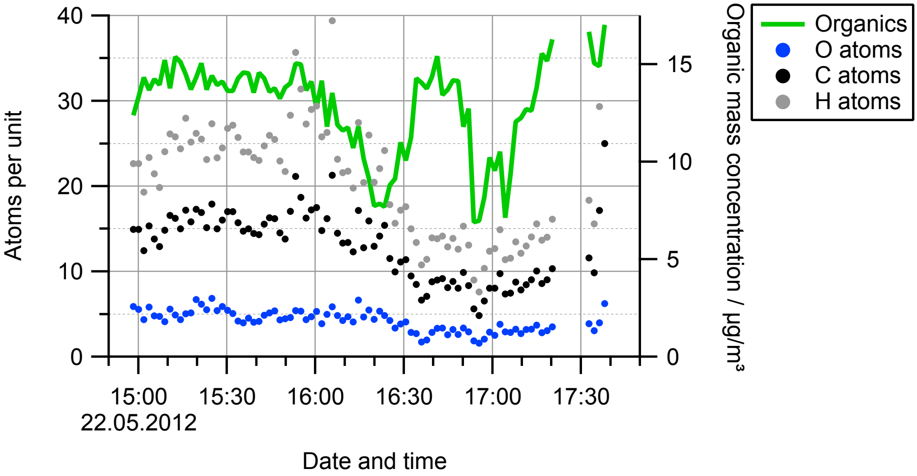

Figure 4.34.: Time series of organic aerosol mass concentration and calculated elemental composition for units containing one carboxylic acid group for 22 May. A relatively sharp drop in total unit atom number is discernible between 16:00 UTC and 16:45 UTC, coincident with the airship flying out on the sea.

wind from north to north-west and wind speeds of around 10 m/s, practically excluding local sources for the measured aerosol. Backward trajectory calculations (see Figure 4.35) suggest a possible transport of the sampled airmass from the northern part of the Netherlands, with approximately 6 h of time over the sea. This time of ageing without addition of fresh material could be an explanation for the high acidity of the aerosol measured at 16:45 UTC and also the relatively high organic mass concentration.

The elemental composition of the organic aerosol after the COO^- is subtracted can be viewed in terms of the van Krevelen diagram (Figure 4.36, also compare section 4.2). It is assumed here, that no C=C double bonds are left in a photochemically processed aerosol, and the amount of quaternary carbon atoms and peroxides can be neglected. The diagram in Figure 4.36 can be interpreted as follows. Organic molecules containing no oxygen would be found on the left side. Molecules with only CH_2 groups would be found in the top left corner. Any addition of tertiary carbon in the form of a branched alkyl chain would move the molecule further down on the left side of the diagram. The addition of hydroxyl groups to methylene groups would move the molecule straight to the right, because of the unchanged hydrogen content and the addition of oxygen. A replacement of methylene groups with ketone groups would move the molecule towards the bottom right, because the addition of oxygen would be accompanied by a loss of hydrogen.

The measured data points fall into the range between chains of methylene groups, chains of methylene groups functionalized with either hydroxyl or ketone groups, and branched alkyl chains with tertiary carbon atoms. While the observations are most likely explained by a mix of all four, two extreme cases of the functionalization can illustrate the functionalization somewhat closer. Case I is described only by contributions from methylene, hydroxyl groups, and ketone groups. Case II is described by contributions from hydroxyl groups and secondary as well as tertiary carbon as the alkyl chain. The observations lie in the intersection of case I and case II. Other available permutations of three contributors would fail to describe the observed data.

Simple vector algebraic considerations including including H/C and O/C of the contributors allow to calculate the degree of functionalization for case I ($\delta^{\mathrm{I}}_{\mathrm{C=O}}$ in Equation 4.16 for carbonyl groups, $\delta^{\mathrm{I}}_{\mathrm{HC-OH}}$ in Equation 4.17 for hydroxyl groups) and case II ($\delta^{\mathrm{II}}_{\mathrm{HC-OH}}$ in Equation 4.18 for hydroxyl groups, $\delta^{\mathrm{II}}_{\mathrm{CH}}$ in Equation 4.19 for tertiary carbon atoms).

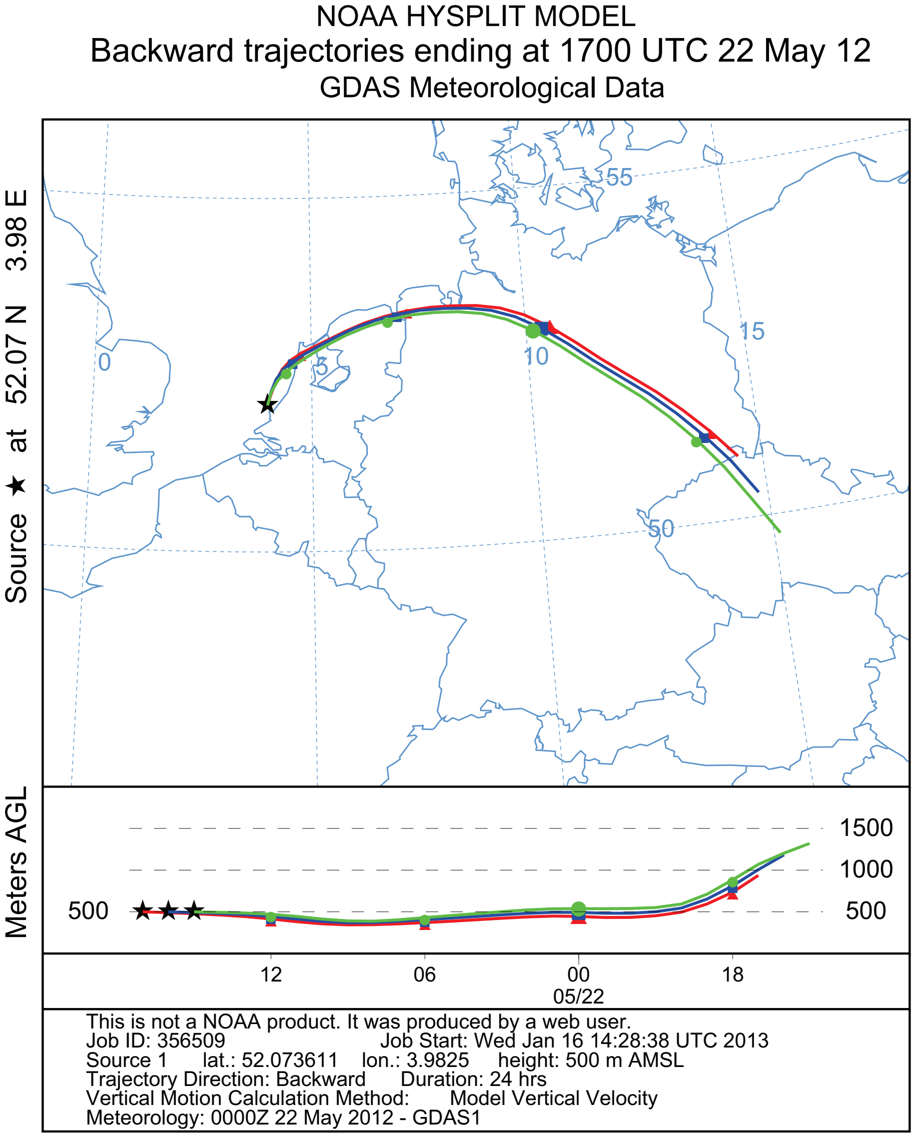

Figure 4.35.: Particle trajectories ending at the 16:45 UTC airship position at 17:00 UTC, 16:00 UTC, and 15:00 UTC. Calculated using the HYSPLIT web interface (Draxler and Hess, 1997) with GDAS meteorological data (Parrish and Derber, 1992).

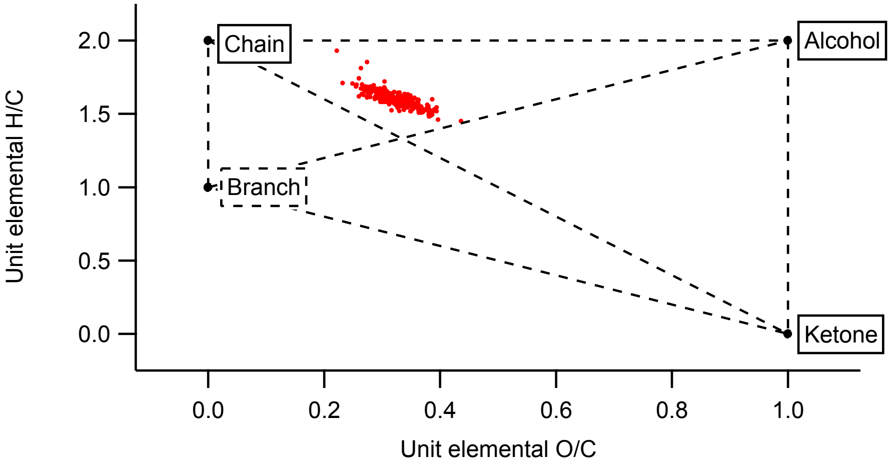

Figure 4.36.: Van Krevelen diagram for 21 May and 22 May, with contributions from carboxylic acid groups removed. The positions of CH_2, HCHO, C=O, and CH groups in this diagram are labelled "Chain", "Alcohol", "Ketone", and "Branch", respectively. Dashed lines between these groups are added to guide the eye.

$$\delta^{\mathrm{I}}_{\mathrm{C=O}} = 1 - \frac{H/C}{2} \tag{4.16}$$

$$\delta^{\mathrm{I}}_{\mathrm{HC-OH}} = O/C + \frac{H/C}{2} - 1 \tag{4.17}$$

$$\delta^{\mathrm{II}}_{\mathrm{HC-OH}} = O/C \tag{4.18}$$

$$\delta^{\mathrm{II}}_{\mathrm{CH}} = 2 - H/C \tag{4.19}$$

The degree of functionalization with carboxylic acid groups $\delta_{\mathrm{COO^-}}$ can be written as in Equation 4.20.

$$\delta_{\mathrm{COO^-}} = \frac{n_{\mathrm{COO^-}}}{n_{\mathrm{COO^-}} + n_{\mathrm{C}}} \tag{4.20}$$

As Equation 4.16, Equation 4.17, Equation 4.18, and Equation 4.19 express the functionalization in the side chain per carboxylic acid group, these values need to be scaled by $1 - \delta_{\mathrm{COO^-}}$ to represent the functionalization degree of the organic aerosol. The calculated functionalization degrees for 21 May and 22 May are shown in Fig. 4.37a and Fig. 4.37b, respectively.

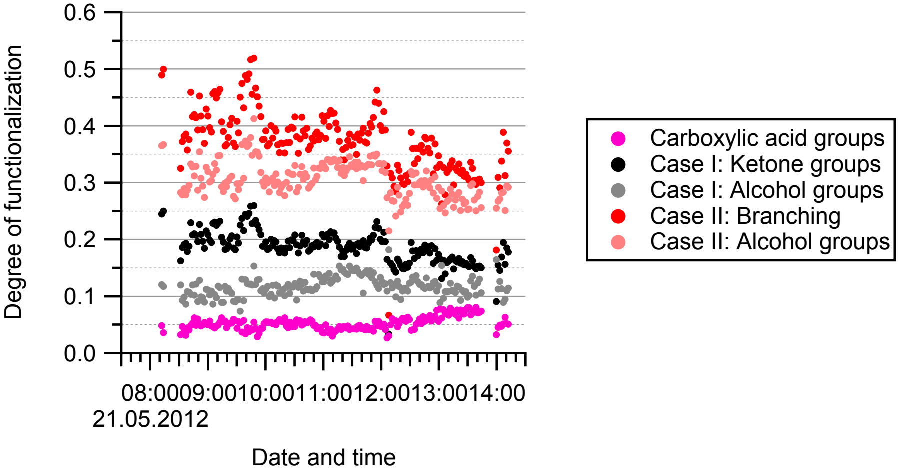

(a)

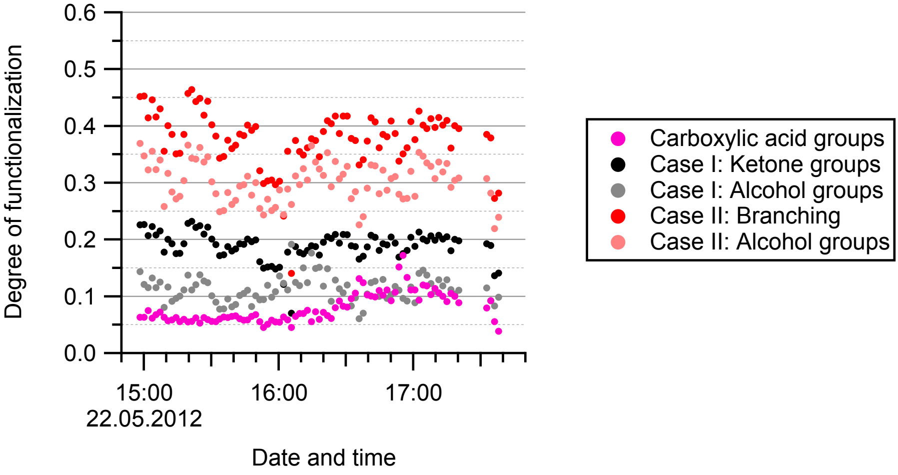

(b)

Figure 4.37.: Degree of functionalization with carboxylic acid and other groups, according to case I and II as described in the text. Fig. 4.37a shows data for 21 May, Fig. 4.37b for 22 May.

The graphs show, that case II leads to unrealistically high total functionalization degrees in the range of 60 % to 90 %. Case I leads to total functionalization degrees in the range of 30 % to 45 %. In this case, approximately 5 % to 10 % of the carbon atoms would be found in carboxylic acid groups, approximately 10 % to 15 % would bear a hydroxyl group, and approximately 15 % to 25 % would be found in carbonyl groups. To summarize, the analysis performed here exploits the special situation of finding excess ammonium in the particulate matter to yield organic aerosol functionalization degrees in a simple manner. An increased carboxylic acid content can be associated with a higher aerosol age. The functionalization degrees found for case II are realistic. For a more detailed analysis, more constraints on at least one other functional group would be desirable to reduce the ambiguity of the results. Also, a comparison to offline techniques capable of identifying individual organic aerosol compounds would help to judge the applicability of the developed method.

5. Conclusions

This work enabled spatially highly resolved aerosol composition measurements in all layers of the PBL by adapting an aerosol mass spectrometer to the requirements posed by an airship as measurement platform. These requirements included the certification of structural integrity with forces of up to 4 kN acting upon the instrument, the reduction of mass, and the integration into an upright 19 inch rack. The mass of the instrument was, compared to the commercial version of the AMS, reduced by 20 % to 134.5 kg. Space occupation and footprint were each reduced by 25 %. Furthermore, the instruments inlet system is now kept at a regulated pressure and can be closed off electronically.

The developed instrument was successfully operated on a Zeppelin NT airship in the frame of the multinational European project PEGASOS. Within a measurement campaign spanning seven weeks and two countries, the instrument performed well on nine out of ten measurement days. The robustness of the new instrument becomes even more clear, when the low failure rate is seen in the background of harsh operating conditions with temperatures of up to 40 °C and relative humidities of up to 90 %.

The obtained data has been presented and specific aspects have been analysed in detail.

Comparing the average aerosol composition, major differences between the countries were found in the high relative abundance of nitrates in the Netherlands and a higher relative abundance of sulfates in Italy. The organic aerosol has been found to be less aged in the Netherlands and there are indications for a more pronounced functionalization with carboxylic acid groups.

Changes in aerosol chemical composition have been analysed for their influence on the aerosol hygroscopicity parameter κ. The prediction of κ values allowed a prediction of CCN concentration in conjunction with SMPS measurements performed on board the airship. κ and the CCN concentration gave insight into the influence of aerosol chemical composition and size distribution changes on aerosol cloud formation potential. In some situations, changes in CCN concentrations were dominated by changes in chemical composition, in other situations changes in the size distribution had the major contribution. When the chemical composition was of importance, NH_4NO_3 played an important role because of its high hygroscopicity and the high variability in its mass concentration.

The aerosol chemical composition has been characterized in all layers of the evolving PBL. Enhanced concentrations of aerosol containing nitrate and organic material were found in the lifted nocturnal boundary layer. The residual layer was found to contain enhanced sulfate aerosol concentrations and organic aerosol of high age. The nitrate aerosol concentration was drastically decreased in the residual layer, also leading to a lowered aerosol hygroscopicity there. The mixed layer was found to have a high regional variation in aerosol chemical composition and mass concentration.

In a case study, backward trajectory calculations were used to estimate the Po valley aerosol formation rate to 0.60 $(\mu g/m^3)/h$ for organic aerosol, 0.88 $(\mu g/m^3)/h$ for nitrate aerosol, and 0.15 $(\mu g/m^3)/h$ for sulfate aerosol. Comparing these estimations to HNO_3 and OVOC production rates calculated from auxiliary gas phase data lead to reasonable particle yields.

Ammonium concentrations in excess to ammonia salts with mineral acids found in the Netherlands were associated with carboxylic acid functionalities in the organic aerosol, evening out the ion balance. The added constraint allowed to calculate the degree of carbon functionalization with hydroxyl and keto groups in the organic aerosol.

Future work will include a more detailed analysis of the relationship between AMS data and SMPS data. As presented, the aerosol mass concentrations determined from both instruments showed a good correlation, but the absolute values were not consistent within the uncertainty of the comparison.

The aerosol composition measurements are planned to be set into frame by ground based measurements performed at the meteorological tower in Cabauw, NL; ground sites in Bologna and San Pietro Capofiume, IT; and mobile measurements performed in a car laboratory during the southbound PEGASOS campaign.

To relate the predicted aerosol hygroscopicity to actual measurements, a comparison to measurements with the WHOPS instrument is aspired.

The cycle of measurements over rural and urban areas of Europe is going to be complemented by a six week campaign over the remote areas of Finland.

Nomenclature

CE	Collection efficiency
IE	Ionization efficiency
MW	Molecular weight
RIE	Relative ionization efficiency
ADC	Analog-to-digital converter
AMS	Aerosol Mass Spectrometer (Aerodyne Research, Inc.)
CCN	Cloud condensation nuclei
CL5	Cabin layout five, focused on secondary organic aerosol observations
CPC	Condensation particle counter
D_a	Particle aerodynamic diameter
DMA	Differential Mobility Analyzer
D_{me}	Particle electrical mobility diameter
DMS	Dimethyl sulfide
D_p	Particle physical diameter (also called geometric diameter)
$\mathrm{NO_x}$	Nitrous oxides
D_{va}	Particle vacuum aerodynamic diameter
D_{ve}	Particle equivalent volume diameter
EC	Elemental carbon
EI	Electron ionization

f_{43}	Contribution of m/z 43 to the organic mass spectrum
f_{44}	Contribution of m/z 44 to the organic mass spectrum
HOA	Hydocarbon-like organic aerosol
HR-ToF-AMS	High Resolution Time of Flight Aerosol Mass Spectrometer
MCP	Microchannel plate
ML	Mixed layer
MS	Mass spectrum
NBL	Stable nocturnal boundary layer
OC	Organic carbon
OOA	Oxidised organic aerosol
OPC	Optical particle counter
OVOC	Oxidised volatile organic compound
PBL	Planetary boundary layer
PEGASOS	Pan-European gas-aerosols-climate interaction study, funded by the European Commission under the Framework Programme 7 (FP7-ENV-2010-265148)
PMF	Positive matrix factorization
PSL	Polystyrene latex sphere
PSM	Particle size magnifier
PToF	Particle time of flight
RL	Residual layer
SOA	Secondary organic aerosol
SPC	San Pietro Capofiume (ground measurement site near Bologna, IT)
VOC	Volatile organic compound
WHOPS	White-light humidified optical particle spectrometer

Bibliography

Adam, M., Putaud, J. P., Martins dos Santos, S., Dell'Acqua, A., and Gruening, C.: Aerosol hygroscopicity at a regional background site (Ispra) in Northern Italy, Atmospheric Chemistry and Physics, 12, 5703–5717, doi:10.5194/acp-12-5703-2012, 2012.

Agarwal, J. K. and Sem, G. J.: Continuous flow, single-particle-counting condensation nucleus counter, Journal of Aerosol Science, 11, 343–357, doi:10.1016/0021-8502(80)90042-7, 1980.

Aiken, A. C., DeCarlo, P. F., and Jimenez, J. L.: Elemental Analysis of Organic Species with Electron Ionization High-Resolution Mass Spectrometry, Analytical Chemistry, 79, 8350–8358, doi:10.1021/ac071150w, 2007.

Aiken, A. C., DeCarlo, P. F., Kroll, J. H., Worsnop, D. R., Huffman, J. A., Docherty, K. S., Ulbrich, I. M., Mohr, C., Kimmel, J. R., Sueper, D., Sun, Y., Zhang, Q., Trimborn, A., Northway, M., Ziemann, P. J., Canagaratna, M. R., Onasch, T. B., Alfarra, M. R., Prevot, A. S. H., Dommen, J., Duplissy, J., Metzger, A., Baltensperger, U., and Jimenez, J. L.: O/C and OM/OC Ratios of Primary, Secondary, and Ambient Organic Aerosols with High-Resolution Time-of-Flight Aerosol Mass Spectrometry, Environmental Science & Technology, 42, 4478–4485, doi:10.1021/es703009q, pMID: 18605574, 2008.

Albrecht, B. A.: Aerosols, Cloud Microphysics, and Fractional Cloudiness, Science, 245, 1227–1230, doi:10.1126/science.245.4923.1227, 1989.

Alfarra, M. R., Coe, H., Allan, J. D., Bower, K. N., Boudries, H., Canagaratna, M. R., Jimenez, J. L., Jayne, J. T., Garforth, A. A., Li, S.-M., and Worsnop, D. R.: Characterization of urban and rural organic particulate in the Lower Fraser Valley using two Aerodyne Aerosol Mass Spectrometers, Atmospheric Environment, 38, 5745–5758, doi:10.1016/j.atmosenv.2004.01.054, 2004.

Allan, J. D., Jimenez, J. L., Williams, P. I., Alfarra, M. R., Bower, K. N., Jayne, J. T., Coe, H., and Worsnop, D. R.: Quantitative sampling using an Aerodyne aerosol mass spectrometer 1. Techniques of data interpretation and error analysis, Journal of Geophysical Research, 108, 4090–4099, doi:10.1029/2002JD002358, 2003.

Allan, J. D., Delia, A. E., Coe, H., Bower, K. N., Alfarra, M., Jimenez, J. L., Middlebrook, A. M., Drewnick, F., Onasch, T. B., Canagaratna, M. R., Jayne, J. T., and Worsnop, D. R.: A generalised method for the extraction of chemically resolved mass spectra from Aerodyne aerosol mass spectrometer data, Journal of Aerosol Science, 35, 909–922, doi:10.1016/j.jaerosci.2004.02.007, 2004.

Bahreini, R., Jimenez, J. L., Wang, J., Flagan, R. C., Seinfeld, J. H., Jayne, J. T., and Worsnop, D. R.: Aircraft-based aerosol size and composition measurements during ACE-Asia using an Aerodyne aerosol mass spectrometer, Journal of Geophysical Research: Atmospheres, 108, doi:10.1029/2002JD003226, 2003.

Bahreini, R., Dunlea, E. J., Matthew, B. M., Simons, C., Docherty, K. S., DeCarlo, P. F., Jimenez, J. L., Brock, C. A., and Middlebrook, A. M.: Design and Operation of a Pressure-Controlled Inlet for Airborne Sampling with an Aerodynamic Aerosol Lens, Aerosol Science and Technology, 42, 465–471, doi:10.1080/02786820802178514, 2008.

Beauford, W., Barber, J., and Barringer, A. R.: Heavy metal release from plants into the atmosphere, Nature, 256, 35–37, doi:10.1038/256035a0, 1975.

Bolton, D.: The computation of equivalent potential temperature, Monthly Weather Review, 108, 1046–1053, doi:10.1175/1520-0493(1980)108<1046:TCOEPT>2.0.CO;2, 1980.

Bouwman, A. F., Lee, D. S., Asman, W. A. H., Dentener, F. J., Van Der Hoek, K. W., and Olivier, J. G. J.: A global high-resolution emission inventory for ammonia, Global Biogeochemical Cycles, 11, 561–587, doi:10.1029/97GB02266, 1997.

Canagaratna, M., Jayne, J., Jimenez, J., Allan, J., Alfarra, M., Zhang, Q., Onasch, T., Drewnick, F., Coe, H., Middlebrook, A., Delia, A., Williams, L., Trimborn, A., Northway, M., DeCarlo, P., Kolb, C., Davidovits, P., and Worsnop, D.: Chemical and microphysical characterization of ambient aerosols with the aerodyne aerosol mass spectrometer, Mass Spectrometry Reviews, 26, 185–222, doi:10.1002/mas.20115, 2007.

Crosier, J., Allan, J. D., Coe, H., Bower, K. N., Formenti, P., and Williams, P. I.: Chemical composition of summertime aerosol in the Po Valley (Italy), northern Adriatic and Black Sea, Quarterly Journal of the Royal Meteorological Society, 133, 61–75, doi:10.1002/qj.88, 2007.

Cross, E. S., Slowik, J. G., Davidovits, P., Allan, J. D., Worsnop, D. R., Jayne, J. T., Lewis, D. K., Canagaratna, M., and Onasch, T. B.: Laboratory and Ambient Particle Density Determinations using Light Scattering in Conjunction with Aerosol Mass Spectrometry, Aerosol Science and Technology, 41, 343–359, doi:10.1080/02786820701199736, 2007.

DeCarlo, P. F., Slowik, J. G., Worsnop, D. R., Davidovits, P., and Jimenez, J. L.: Particle Morphology and Density Characterization by Combined Mobility and Aerodynamic Diameter Measurements. Part 1: Theory, Aerosol Science and Technology, 38, 1185–1205, doi:10.1080/027868290903907, 2004.

DeCarlo, P. F., Kimmel, J. R., Trimborn, A., Northway, M. J., Jayne, J. T., Aiken, A. C., Gonin, M., Fuhrer, K., Horvath, T., Docherty, K. S., Worsnop, D. R., and Jimenez, J. L.: Field-Deployable, High-Resolution, Time-of-Flight Aerosol Mass Spectrometer, Analytical Chemistry, 78, 8281–8289, doi:10.1021/ac061249n, 2006.

D'Ottone, L., Campuzano-Jost, P., Bauer, D., and Hynes, A. J.: A Pulsed Laser Photolysis Pulsed Laser Induced Fluorescence Study of the Kinetics of the Gas-Phase Reaction of OH with NO2, The Journal of Physical Chemistry A, 105, 10 538–10 543, doi:10.1021/jp012250n, 2001.

Draxler, R. R. and Hess, G.: Description of the HYSPLIT_4 modeling system, NOAA Technical Memorandum ERL ARL-224, NOAA Air Resources Laboratory, Silver Spring, Maryland, 1997.

Drewnick, F., Hings, S. S., DeCarlo, P., Jayne, J. T., Gonin, M., Fuhrer, K., Weimer, S., Jimenez, J. L., Demerjian, K. L., Borrmann, S., and Worsnop, D. R.: A New Time-of-Flight Aerosol Mass Spectrometer (TOF-AMS) – Instrument Description and First Field Deployment, Aerosol Science and Technology, 39, 637–658, doi:10.1080/02786820500182040, 2005.

Drisdell, W. S., Saykally, R. J., and Cohen, R. C.: On the evaporation of ammonium sulfate solution, Proceedings of the National Academy of Sciences, 106, 18 897–18 901, doi:10.1073/pnas.0907988106, 2009.

Eerden, L. V. D., Vries, W. D., and Dobben, H. V.: Effects of ammonia deposition on forests in the Netherlands, Atmospheric Environment, 32, 525–532, doi:10.1016/S1352-2310(97)00009-5, nH3 annual mean 2-23 mug/m3, 1998.

Emanuelsson, E. U., Hallquist, M., Kristensen, K., Glasius, M., Bohn, B., Fuchs, H., Kammer, B., Kiendler-Scharr, A., Nehr, S., Rubach, F., Tillmann, R., Wahner, A., Wu, H.-C., and Mentel, T. F.: Formation of anthropogenic secondary organic aerosol (SOA) and its influence on biogenic SOA properties, Atmospheric Chemistry and Physics, 13, 2837–2855, doi:10.5194/acp-13-2837-2013, 2013.

Fehsenfeld, F., Calvert, J., Fall, R., Goldan, P., Guenther, A. B., Hewitt, C. N., Lamb, B., Liu, S., Trainer, M., Westberg, H., and Zimmerman, P.: Emissions of volatile organic compounds from vegetation and the implications for atmospheric chemistry, Global Biogeochemical Cycles, 6, 389–430, doi:10.1029/92GB02125, 1992.

Finlayson-Pitts, B. and Pitts, J.: Chemistry of the Upper and Lower Atmosphere: Theory, Experiments, and Applications, Academic Press, 2000.

Fors, E. O., Swietlicki, E., Svenningsson, B., Kristensson, A., Frank, G. P., and Sporre, M.: Hygroscopic properties of the ambient aerosol in southern Sweden: a two year study, Atmospheric Chemistry and Physics, 11, 8343–8361, doi:10.5194/acp-11-8343-2011, 2011.

Forster, R., Frost, M., Fulle, D., Hamann, H. F., Hippler, H., Schlepegrell, A., and Troe, J.: High pressure range of the addition of HO to HO, NO, NO2, and CO. I. Saturated laser induced fluorescence measurements at 298 K, The Journal of Chemical Physics, 103, 2949–2958, doi:10.1063/1.470482, 1995.

FORTH/ICE-HT: PEGASOS - Home page, `http://pegasos.iceht.forth.gr/`, accessed: December 2012.

Fulle, D., Hamann, H. F., Hippler, H., and Troe, J.: Temperature and pressure dependence of the addition reactions of HO to NO and to NO2. IV. Saturated laser-induced fluorescence measurements up to 1400 bar, The Journal of Chemical Physics, 108, 5391–5397, doi:10.1063/1.475971, 1998.

Good, N., Topping, D. O., Allan, J. D., Flynn, M., Fuentes, E., Irwin, M., Williams, P. I., Coe, H., and McFiggans, G.: Consistency between parameterisations of aerosol hygroscopicity and CCN activity during the RHaMBLe discovery cruise, Atmospheric Chemistry and Physics, 10, 3189–3203, doi:10.5194/acp-10-3189-2010, 2010.

Guenther, A., Hewitt, C. N., Erickson, D., Fall, R., Geron, C., Graedel, T., Harley, P., Klinger, L., Lerdau, M., Mckay, W. A., Pierce, T., Scholes, B., Steinbrecher, R., Tallamraju, R., Taylor, J., and Zimmerman, P.: A global model of natural volatile organic compound emissions, Journal of Geophysical Research, 100, 8873–8892, doi:10.1029/94JD02950, 1995.

Gysel, M., Crosier, J., Topping, D. O., Whitehead, J. D., Bower, K. N., Cubison, M. J., Williams, P. I., Flynn, M. J., McFiggans, G. B., and Coe, H.: Closure study between chemical composition and hygroscopic growth of aerosol particles during TORCH2, Atmospheric Chemistry and Physics, 7, 6131–6144, doi:10.5194/acp-7-6131-2007, 2007.

de Haij, M., Wauben, W., and Klein Baltink, H.: Continuous mixing layer height determination using the LD-40 ceilometer: a feasibility study, Royal Netherlands Meteorological Institute (KNMI), De Bilt, URL `http://edepot.wur.nl/62411`, 2007.

Häseler, R., Brauers, T., Holland, F., and Wahner, A.: Development and application of a new mobile LOPAP instrument for the measurement of HONO altitude profiles in the planetary boundary layer, Atmospheric Measurement Techniques Discussions, 2, 2027–2054, doi:10.5194/amtd-2-2027-2009, 2009.

Heald, C. L., Kroll, J. H., Jimenez, J. L., Docherty, K. S., DeCarlo, P. F., Aiken, A. C., Chen, Q., Martin, S. T., Farmer, D. K., and Artaxo, P.: A simplified description of the evolution of organic aerosol composition in the atmosphere, Geophysical Research Letters, 37, L08 803, doi:10.1029/2010GL042737, 2010.

Heald, C. L., Coe, H., Jimenez, J. L., Weber, R. J., Bahreini, R., Middlebrook, A. M., Russell, L. M., Jolleys, M., Fu, T.-M., Allan, J. D., Bower, K. N., Capes, G., Crosier, J., Morgan, W. T., Robinson, N. H., Williams, P. I., Cubison, M. J., DeCarlo, P. F., and Dunlea, E. J.: Exploring the vertical profile of atmospheric organic aerosol: comparing 17 aircraft field campaigns with a global model, Atmospheric Chemistry and Physics, 11, 12 673–12 696, doi:10.5194/acp-11-12673-2011, 2011.

Hering, S. and Friedlander, S.: Origins of aerosol sulfur size distributions in the Los Angeles basin, Atmospheric Environment, 16, 2647–2656, doi:10.1016/0004-6981(82)90346-8, 1982.

Hinds, W. C.: Aerosol Technology: Properties, Behavior, and Measurement of Airborne Particles, John Wiley & Sons, Inc., 1999.

Hippler, H., Krasteva, N., Nasterlack, S., and Striebel, F.: Reaction of OH + NO2: High Pressure Experiments and Falloff Analysis, The Journal of Physical Chemistry A, 110, 6781–6788, doi:10.1021/jp0562734, pMID: 16722694, 2006.

Hoek, K. V. D.: Estimating ammonia emission factors in Europe: Summary of the work of the UNECE ammonia expert panel, Atmospheric Environment, 32, 315–316, doi:10.1016/S1352-2310(97)00168-4, 80-95emissions in Europe originates from agricultural practices, 1998.

Hoffmann, T., Odum, J. R., Bowman, F., Collins, D., Klockow, D., Flagan, R. C., and Seinfeld, J. H.: Formation of Organic Aerosols from the Oxidation of Biogenic Hydrocarbons, Journal of Atmospheric Chemistry, 26, 189–222, doi:10.1023/A:1005734301837, 1997.

Holland, F., Hofzumahaus, A., Schäfer, J., Kraus, A., and Pätz, H.-W.: Measurements of OH and HO2 radical concentrations and photolysis frequencies during BERLIOZ, Journal of Geophysical Research, 108, 8246, doi:10.1029/2001JD001393, 2003.

Horn, K. R. V., ed.: Aluminum - Vol. II. Design and Application, American Society for Metals, Metals Park, Ohio, 1967.

Hottle, J. R., Huisman, A. J., DiGangi, J. P., Kammrath, A., Galloway, M. M., Coens, K. L., and Keutsch, F. N.: A Laser Induced Fluorescence-Based Instrument for In-Situ Measurements of Atmospheric Formaldehyde, Environmental Science & Technology, 43, 790–795, doi:10.1021/es801621f, pMID: 19245018, 2009.

Huffman, J. A., Jayne, J. T., Drewnick, F., Aiken, A. C., Onasch, T., Worsnop, D. R., and Jimenez, J. L.: Design, Modeling, Optimization, and Experimental Tests of a Particle Beam Width Probe for the Aerodyne Aerosol Mass Spectrometer, Aerosol Science and Technology, 39, 1143–1163, doi:10.1080/02786820500423782, 2005.

Hussain, M., Madl, P., and Khan, A.: Lung deposition predictions of airborne particles and the emergence of contemporary diseases Part-I, Health, 2, 51–59, 2011.

IPCC: Climate Change 2007: Synthesis Report, Tech. rep., Intergovernmental Panel on Climate Change, 2007.

Jaenicke, R.: Aerosol-Cloud-Climate Interactions, Chapter 1: Tropospheric Aerosols, International geophysics series, Academic Press, Inc., 1993.

Jarvis, A., Reuter, H., Nelson, A., and Guevara, E.: Hole-filled seamless SRTM data V4, URL `http://srtm.csi.cgiar.org`, 2008.

Jayne, J. T., Leard, D. C., Zhang, X., Davidovits, P., Smith, K. A., Kolb, C. E., and Worsnop, D. R.: Development of an Aerosol Mass Spectrometer for Size and Composition Analysis of Submicron Particles, Aerosol Science and Technology, 33, 49–70, doi:10.1080/027868200410840, 2000.

Jenkin, M. E., Saunders, S. M., and Pilling, M. J.: The tropospheric degradation of volatile organic compounds: a protocol for mechanism development, Atmospheric Environment, 31, 81–104, doi:10.1016/S1352-2310(96)00105-7, 1997.

Jimenez, J. L., Bahreini, R., Cocker, David R., I., Zhuang, H., Varutbangkul, V., Flagan, R. C., Seinfeld, J. H., O'Dowd, C. D., and Hoffmann, T.: New particle formation from photooxidation of diiodomethane (CH_2I_2), Journal of Geophysical Research, 108, 4318–4343, doi:10.1029/2002JD002452, 2003a.

Jimenez, J. L., Jayne, J. T., Shi, Q., Kolb, C. E., Worsnop, D. R., Yourshaw, I., Seinfeld, J. H., Flagan, R. C., Zhang, X., Smith, K. A., Morris, J. W., and Davidovits, P.: Ambient aerosol sampling using the Aerodyne Aerosol Mass Spectrometer, Journal of Geophysical Research, 108, 8425–8437, doi:10.1029/2001JD001213, 2003b.

Junninen, H., Ehn, M., Petäjä, T., Luosujärvi, L., Kotiaho, T., Kostiainen, R., Rohner, U., Gonin, M., Fuhrer, K., Kulmala, M., and Worsnop, D. R.: A high-resolution mass spectrometer to measure atmospheric ion composition, Atmospheric Measurement Techniques, 3, 1039–1053, doi:10.5194/amt-3-1039-2010, 2010.

Kamens, R. M. and Jaoui, M.: Modeling Aerosol Formation from α-Pinene + NO_x in the Presence of Natural Sunlight Using Gas-Phase Kinetics and Gas-Particle Partitioning Theory, Environmental Science & Technology, 35, 1394–1405, doi:10.1021/es001626s, 2001.

Kammermann, L., Gysel, M., Weingartner, E., and Baltensperger, U.: 13-month climatology of the aerosol hygroscopicity at the free tropospheric site Jungfraujoch (3580 m a.s.l.), Atmospheric Chemistry and Physics, 10, 10 717–10 732, doi:10.5194/acp-10-10717-2010, 2010.

Kanakidou, M., Seinfeld, J. H., Pandis, S. N., Barnes, I., Dentener, F. J., Facchini, M. C., Van Dingenen, R., Ervens, B., Nenes, A., Nielsen, C. J., Swietlicki, E., Putaud, J. P., Balkanski, Y., Fuzzi, S., Horth, J., Moortgat, G. K., Winterhalter, R., Myhre, C. E. L., Tsigaridis, K., Vignati, E., Stephanou, E. G., and Wilson, J.: Organic aerosol and global climate modelling: a review, Atmospheric Chemistry and Physics, 5, 1053–1123, doi:10.5194/acp-5-1053-2005, 2005.

Klemm, R., Mason, R., Heilig, C., Neas, L., and Dockery, D.: Is daily mortality associated specifically with fine particles? Data reconstruction and replication of analyses., Journal of the Air & Waste Management Association, 50, 1215–1222, doi:10.1080/10473289.2000.10464149, 2000.

Köhler, H.: The nucleus in and the growth of hygroscopic droplets, Transactions of the Faraday Society, 32, 1152–1161, doi:10.1039/TF9363201152, 1936.

Kroll, J. H., Donahue, N. M., Jimenez, J. L., Kessler, S. H., Canagaratna, M. R., Wilson, K. R., Altieri, K. E., Mazzoleni, L. R., Wozniak, A. S., Bluhm, H., Mysak, E. R., Smith, J. D., Kolb, C. E., and Worsnop, D. R.: Carbon oxidation state as a metric for describing the chemistry of atmospheric organic aerosol, Nature Chemistry, 3, 133–139, doi:10.1038/nchem.948, 2011.

Kulmala, M., Vehkamäki, H., Petäjä, T., Maso, M. D., Lauri, A., Kerminen, V.-M., Birmili, W., and McMurry, P.: Formation and growth rates of ultrafine atmospheric particles: a review of observations, Journal of Aerosol Science, 35, 143–176, doi:10.1016/j.jaerosci.2003.10.003, 2004.

Kuwata, M., Zorn, S. R., and Martin, S. T.: Using Elemental Ratios to Predict the Density of Organic Material Composed of Carbon, Hydrogen, and Oxygen, Environmental Science & Technology, 46, 787–794, doi:10.1021/es202525q, 2012.

Lambe, A. T., Onasch, T. B., Massoli, P., Croasdale, D. R., Wright, J. P., Ahern, A. T., Williams, L. R., Worsnop, D. R., Brune, W. H., and Davidovits, P.: Laboratory studies of the chemical composition and cloud condensation nuclei (CCN) activity of secondary organic aerosol (SOA) and oxidized primary organic aerosol (OPOA), Atmospheric Chemistry and Physics, 11, 8913–8928, doi:10.5194/acp-11-8913-2011, 2011.

Larson, T. and Taylor, G.: On the evaporation of ammonium nitrate aerosol, Atmospheric Environment (1967), 17, 2489–2495, doi:10.1016/0004-6981(83)90074-4, 1983.

Liu, B. Y. and Pui, D. Y.: A submicron aerosol standard and the primary, absolute calibration of the condensation nuclei counter, Journal of Colloid and Interface Science, 47, 155–171, doi:10.1016/0021-9797(74)90090-3, 1974.

Liu, P., Ziemann, P. J., Kittelson, D. B., and McMurry, P. H.: Generating Particle Beams of Controlled Dimensions and Divergence: II. Experimental Evaluation of Particle Motion in Aerodynamic Lenses and Nozzle Expansions, Aerosol Science and Technology, 22, 314–324, doi:10.1080/02786829408959749, 1995a.

Liu, P., Ziemann, P. J., Kittelson, D. B., and McMurry, P. H.: Generating Particle Beams of Controlled Dimensions and Divergence: I. Theory of Particle Motion in Aerodynamic Lenses and Nozzle Expansions, Aerosol Science and Technology, 22, 293–313, doi:10.1080/02786829408959748, 1995b.

Liu, P. F., Zhao, C. S., Göbel, T., Hallbauer, E., Nowak, A., Ran, L., Xu, W. Y., Deng, Z. Z., Ma, N., Mildenberger, K., Henning, S., Stratmann, F., and Wiedensohler, A.: Hygroscopic properties of aerosol particles at high relative humidity and their diurnal variations in the North China Plain, Atmospheric Chemistry and Physics, 11, 3479–3494, doi:10.5194/acp-11-3479-2011, 2011.

Liu, P. S. K., Deng, R., Smith, K. A., Williams, L. R., Jayne, J. T., Canagaratna, M. R., Moore, K., Onasch, T. B., Worsnop, D. R., and Deshler, T.: Transmission Efficiency of an Aerodynamic Focusing Lens System: Comparison of Model Calculations and Laboratory Measurements for the Aerodyne Aerosol Mass Spectrometer, Aerosol Science and Technology, 41, 721–733, doi:10.1080/02786820701422278, 2007.

Lu, K., Zhang, Y., Su, H., Brauers, T., Chou, C. C., Hofzumahaus, A., Liu, S. C., Kita, K., Kondo, Y., Shao, M., Wahner, A., Wang, J., Wang, X., and Zhu, T.: Oxidant (O3 + NO2) production processes and formation regimes in Beijing, Journal of Geophysical Research, 115, D07 303, doi:10.1029/2009JD012714, 2010.

Mensah, A. A., Holzinger, R., Otjes, R., Trimborn, A., Mentel, T. F., ten Brink, H., Henzing, B., and Kiendler-Scharr, A.: Aerosol chemical composition at Cabauw, The Netherlands as observed in two intensive periods in May 2008 and March 2009, Atmospheric Chemistry and Physics, 12, 4723–4742, doi:10.5194/acp-12-4723-2012, 2012.

Middlebrook, A. M., Bahreini, R., Jimenez, J. L., and Canagaratna, M. R.: Evaluation of Composition-Dependent Collection Efficiencies for the Aerodyne Aerosol Mass Spectrometer using Field Data, Aerosol Science and Technology, 46, 258–271, doi:10.1080/02786826.2011.620041, 2012.

Morgan, W. T., Allan, J. D., Bower, K. N., Highwood, E. J., Liu, D., McMeeking, G. R., Northway, M. J., Williams, P. I., Krejci, R., and Coe, H.: Airborne measurements of the spatial distribution of aerosol chemical composition across Europe and evolution of the organic fraction, Atmospheric Chemistry and Physics, 10, 4065–4083, doi:10.5194/acp-10-4065-2010, 2010.

Murphy, S. M., Agrawal, H., Sorooshian, A., Padró, L. T., Gates, H., Hersey, S., Welch, W. A., Jung, H., Miller, J. W., Cocker, D. R., Nenes, A., Jonsson, H. H., Flagan, R. C., and Seinfeld, J. H.: Comprehensive Simultaneous Shipboard and Airborne Characterization of Exhaust from a Modern Container Ship at Sea, Environmental Science & Technology, 43, 4626–4640, doi:10.1021/es802413j, 2009.

Ng, N. L., Canagaratna, M. R., Zhang, Q., Jimenez, J. L., Tian, J., Ulbrich, I. M., Kroll, J. H., Docherty, K. S., Chhabra, P. S., Bahreini, R., Murphy, S. M., Seinfeld, J. H., Hildebrandt, L., Donahue, N. M., DeCarlo, P. F., Lanz, V. A., Prévôt, A. S. H., Dinar, E., Rudich, Y., and Worsnop, D. R.: Organic aerosol components observed in Northern Hemispheric datasets from Aerosol Mass Spectrometry, Atmospheric Chemistry and Physics, 10, 4625–4641, doi:10.5194/acp-10-4625-2010, sally triangle, northern hemisphere PMF, 2010.

Nowak, J. B., Neuman, J. A., Bahreini, R., Brock, C. A., Middlebrook, A. M., Wollny, A. G., Holloway, J. S., Peischl, J., Ryerson, T. B., and Fehsenfeld, F. C.: Airborne observations of ammonia and ammonium nitrate formation over Houston, Texas, Journal of Geophysical Research: Atmospheres, 115, doi:10.1029/2010JD014195, 2010.

Odum, J. R., Hoffmann, T., Bowman, F., Collins, D., Flagan, R. C., and Seinfeld, J. H.: Gas/Particle Partitioning and Secondary Organic Aerosol Yields, Environmental Science and Technology, 30, 2580–2585, doi:10.1021/es950943+, 1996.

Paatero, P. and Tapper, U.: Positive matrix factorization: A non-negative factor model with optimal utilization of error estimates of data values, Environmetrics, 5, 111–126, doi:10.1002/env.3170050203, 1994.

Padró, L. T., Tkacik, D., Lathem, T., Hennigan, C. J., Sullivan, A. P., Weber, R. J., Huey, L. G., and Nenes, A.: Investigation of cloud condensation nuclei properties and droplet growth kinetics of the water-soluble aerosol fraction in Mexico City, Journal of Geophysical Research: Atmospheres, 115, D09 204, doi:10.1029/2009JD013195, 2010.

Pandis, S., ed.: Description of Work PEGASOS, European Commission, Framework Programme 7 (FP7-ENV-2010-265148), 2010.

Pandis, S. N., Harley, R. A., Cass, G. R., and Seinfeld, J. H.: Secondary organic aerosol formation and transport, Atmospheric Environment. Part A. General Topics, 26, 2269–2282, doi:10.1016/0960-1686(92)90358-R, 1992.

Parrish, D. F. and Derber, J. C.: The National Meteorological Center's Spectral

Statistical-Interpolation Analysis System, Monthly Weather Review, 120, 1747–1763, doi:10.1175/1520-0493(1992)120<1747:TNMCSS>2.0.CO;2, 1992.

Peirson, D. H., Cawse, P. A., and Cambray, R. S.: Chemical uniformity of airborne particulate material, and a maritime effect, Nature, 251, 675–679, doi:10.1038/251675a0, 1974.

Petters, M. D. and Kreidenweis, S. M.: A single parameter representation of hygroscopic growth and cloud condensation nucleus activity, Atmospheric Chemistry and Physics, 7, 1961–1971, doi:10.5194/acp-7-1961-2007, 2007.

Politovich, M. K. and Cooper, W. A.: Variability of the Supersaturation in Cumulus Clouds, J. Atmos. Sci., 45, 1651–1664, doi:10.1175/1520-0469(1988)045<1651:VOTSIC>2.0.CO;2, 1988.

Pope, C. A.: Mortality Effects of Longer Term Exposures to Fine Particulate Air Pollution: Review of Recent Epidemiological Evidence, Inhalation Toxicology, 19, 33–38, doi:10.1080/08958370701492961, pMID: 17886048, 2007.

Rohrer, F. and Brüning, D.: Surface NO and NO2 mixing ratios measured between 30°N and 30°S in the Atlantic region, Journal of Atmospheric Chemistry, 15, 253–267, doi:10.1007/BF00115397, 1992.

Saunders, S. M., Jenkin, M. E., Derwent, R. G., and Pilling, M. J.: Protocol for the development of the Master Chemical Mechanism, MCM v3 (Part A): tropospheric degradation of non-aromatic volatile organic compounds, Atmospheric Chemistry and Physics, 3, 161–180, doi:10.5194/acp-3-161-2003, 2003.

Seinfeld, J. H. and Pandis, S. N.: Atmospheric Chemistry and Physics: From Air Pollution to Climate Change, John Wiley & Sons, Inc., 1998.

Sensidyne, LP: Gilibrator-2 Specifications, `http://www.shop.sensidyne.com/air-sampling-equipment/calibration-equipment/gilibrator-2.php`, accessed: December 2012.

Sorooshian, A., Murphy, S. M., Hersey, S., Gates, H., Padro, L. T., Nenes, A., Brechtel, F. J., Jonsson, H., Flagan, R. C., and Seinfeld, J. H.: Comprehensive airborne characterization of aerosol from a major bovine source, Atmospheric Chemistry and Physics, 8, 5489–5520, doi:10.5194/acp-8-5489-2008, 2008.

Stull, R.: An Introduction to Boundary Layer Meteorology, Atmospheric Science Library, Springer, 1988.

Tang, I. N.: On the equilibrium partial pressures of nitric acid and ammonia in the atmosphere, Atmospheric Environment (1967), 14, 819–828, doi:10.1016/0004-6981(80)90138-9, hNO3 vapor pressure, 1980.

Todd, J. F. J.: Recommendations for nomenclature and symbolism for mass spectroscopy (including an appendix of terms used in vacuum technology).

(IUPAC Recommendations 1991), Pure and Applied Chemistry, 63, 1541–1566, doi:10.1351/pac199163101541, 1991.

Troe, J.: Analysis of the temperature and pressure dependence of the reaction HO + NO2 + M <-> HONO2 + M, International Journal of Chemical Kinetics, 33, 878–889, doi:10.1002/kin.10019, 2001.

TSI, Inc.: Model 3022A Condensation Particle Counter Instruction Manual, revision i edn., 2002.

Twomey, S.: Pollution and the planetary albedo, Atmospheric Environment (1967), 8, 1251–1256, doi:10.1016/0004-6981(74)90004-3, 1974.

Ulbrich, I. M., Canagaratna, M. R., Zhang, Q., Worsnop, D. R., and Jimenez, J. L.: Interpretation of organic components from Positive Matrix Factorization of aerosol mass spectrometric data, Atmospheric Chemistry and Physics, 9, 2891–2918, doi:10.5194/acp-9-2891-2009, 2009.

van Krevelen, D. W.: Graphical-statistical method for the study of structure and reaction processes of coal, Fuel, 24, 269–284, 1950.

Vanhanen, J., Mikkilä, J., Lehtipalo, K., Sipilä, M., Manninen, H. E., Siivola, E., Petäjä, T., and Kulmala, M.: Particle Size Magnifier for Nano-CN Detection, Aerosol Science and Technology, 45, 533–542, doi:10.1080/02786826.2010.547889, 2011.

von Helmholtz, R.: Untersuchungen über Dämpfe und Nebel, besonders über solche von Lösungen, Annalen der Physik und Chemie, 263, 508–543, 1886.

Vrekoussis, M., Liakakou, E., Mihalopoulos, N., Kanakidou, M., Crutzen, P. J., and Lelieveld, J.: Formation of HNO3 and NO3- in the anthropogenically-influenced eastern Mediterranean marine boundary layer, Geophysical Research Letters, 33, L05 811, doi:10.1029/2005GL025069, 2006.

Wegener, R. and Jäger, J.: personal communication, 2013.

Zhang, Q., Jimenez, J. L., Canagaratna, M. R., Allan, J. D., Coe, H., Ulbrich, I., Alfarra, M. R., Takami, A., Middlebrook, A. M., Sun, Y. L., Dzepina, K., Dunlea, E., Docherty, K., DeCarlo, P. F., Salcedo, D., Onasch, T., Jayne, J. T., Miyoshi, T., Shimono, A., Hatakeyama, S., Takegawa, N., Kondo, Y., Schneider, J., Drewnick, F., Borrmann, S., Weimer, S., Demerjian, K., Williams, P., Bower, K., Bahreini, R., Cottrell, L., Griffin, R. J., Rautiainen, J., Sun, J. Y., Zhang, Y. M., and Worsnop, D. R.: Ubiquity and dominance of oxygenated species in organic aerosols in anthropogenically-influenced Northern Hemisphere midlatitudes, Geophysical Research Letters, 34, L13 801, doi:10.1029/2007GL029979, 2007.

Zhang, Q., Jimenez, J., Canagaratna, M., Ulbrich, I., Ng, N., Worsnop, D., and Sun, Y.: Understanding atmospheric organic aerosols via factor analysis of aerosol mass spectrometry: a review, Analytical and Bioanalytical Chemistry, 401, 3045–3067, doi:10.1007/s00216-011-5355-y, 2011.

Zhang, X., Smith, K. A., Worsnop, D. R., Jimenez, J. L., Jayne, J. T., Kolb, C. E., Morris, J., and Davidovits, P.: Numerical Characterization of Particle Beam Collimation: Part II Integrated Aerodynamic-Lens-Nozzle System, Aerosol Science and Technology, 38, 619–638, doi:10.1080/02786820490479833, 2004.

A. Flight tracks

Flight tracks that are not shown in chapter 3 are depicted here. The background of all figures in this section corresponds to elevation data taken from publicly available Shuttle Radar Topography Mission (SRTM, Jarvis et al. (2008)) data. The flight track data points are colour-coded by averaged pressure altitude in the respective time range.

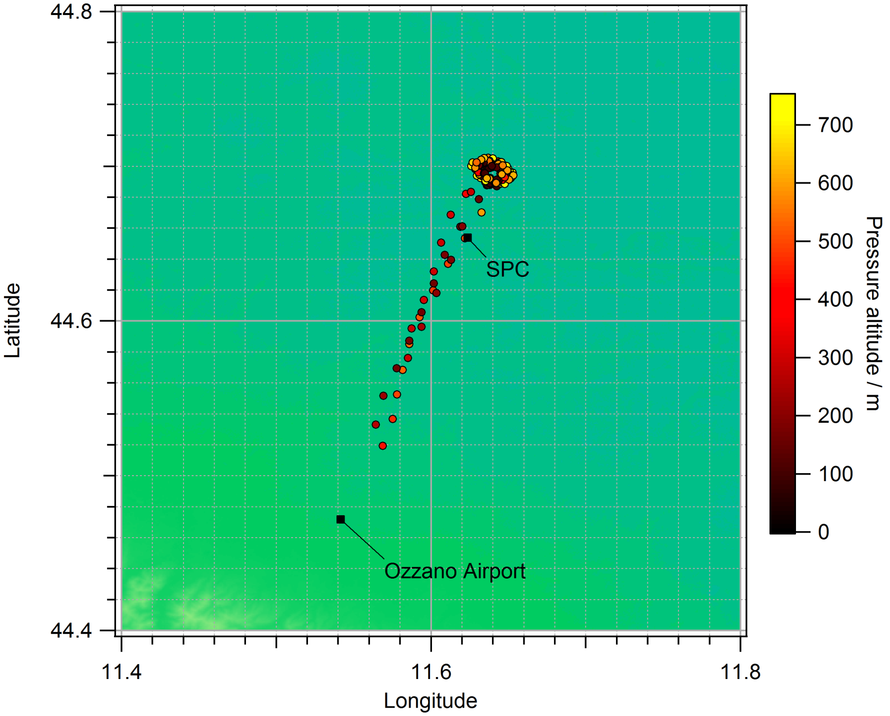

Figure A.1.: Flight track for 20 June 2012.

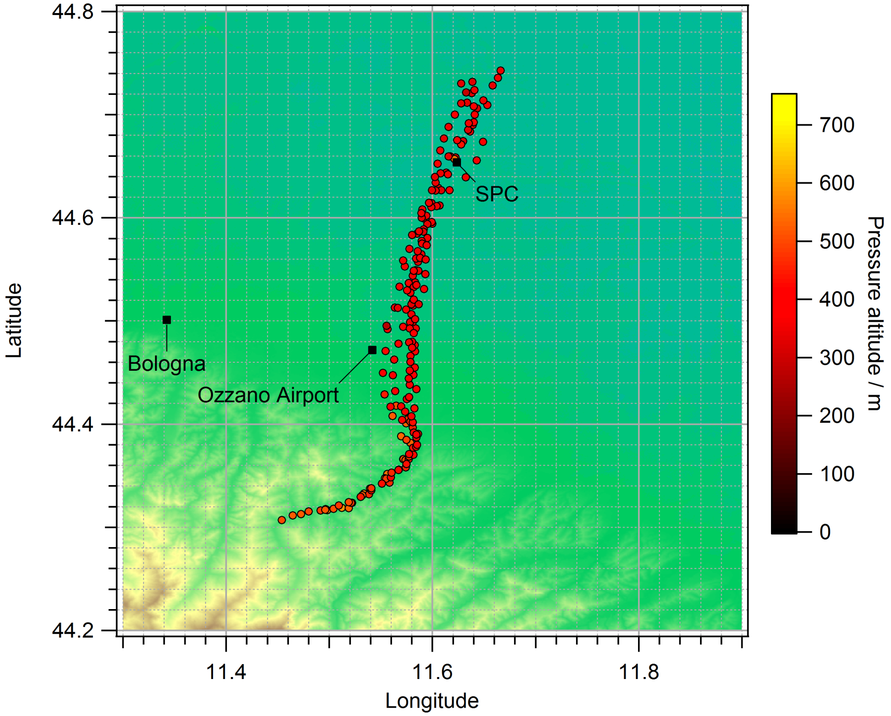

Figure A.2.: Flight track for 21 June 2012.

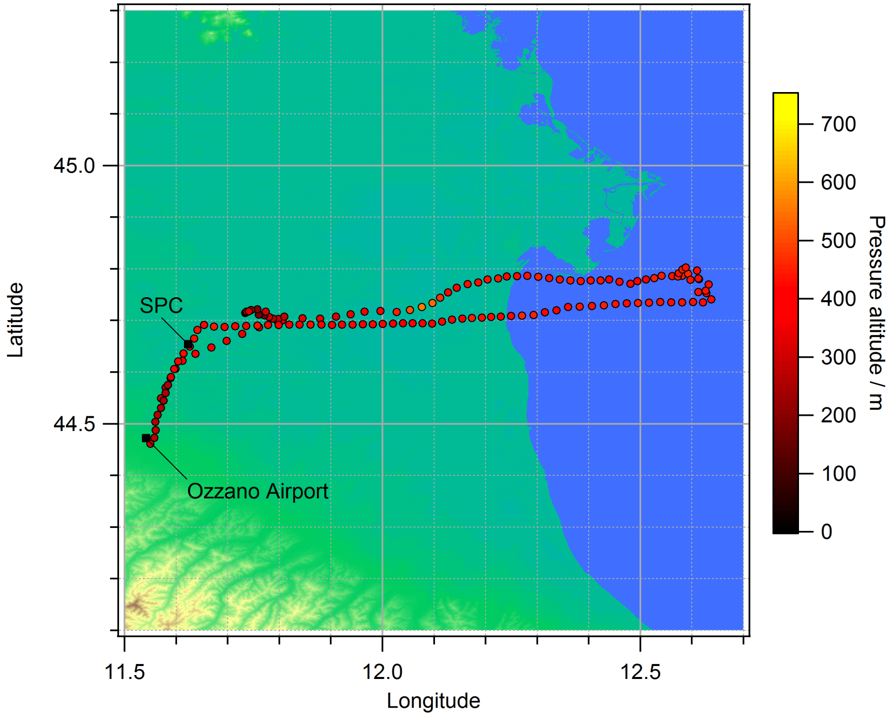

Figure A.3.: Flight track for 22 June 2012.

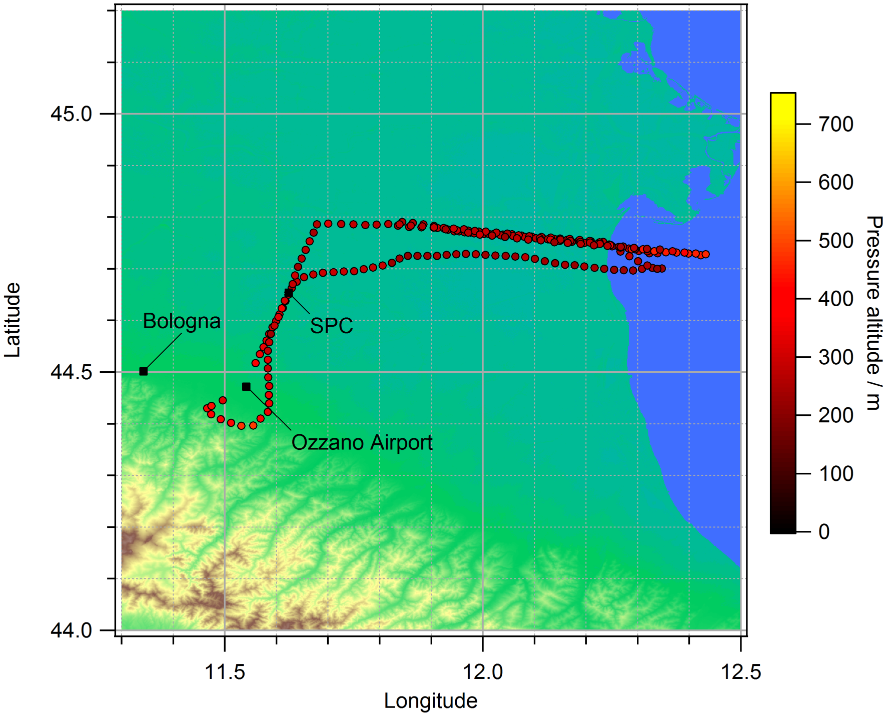

Figure A.4.: Flight track for 24 June 2012.

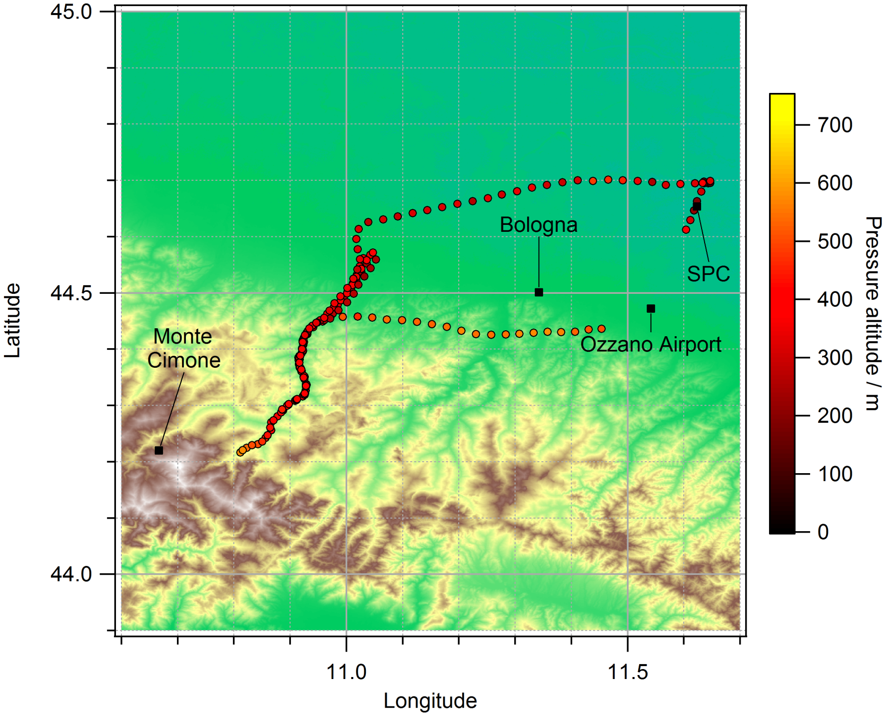

Figure A.5.: Flight track for 4 July 2012.

B. Hygroscopicity parameter time series

For days not discussed in detail in section 4.3, the time series of aerosol component contributions to the hygroscopicity parameter κ are shown here. κ is calculated for hygroscopic growth at 90 % RH.

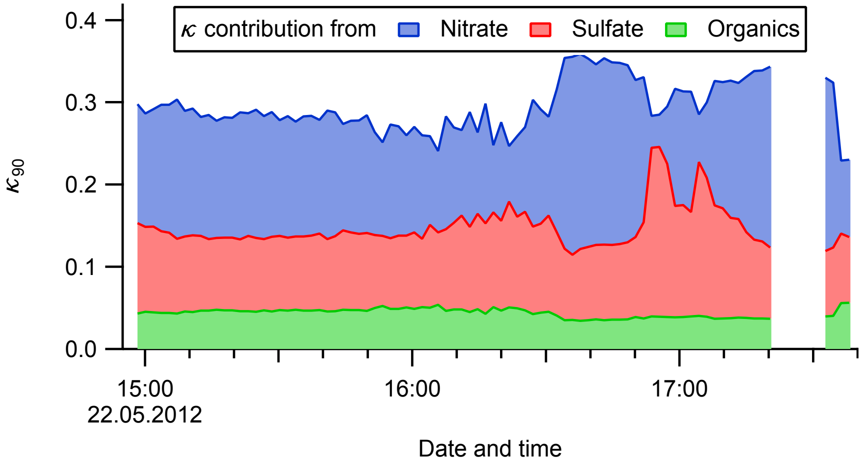

Figure B.1.: Aerosol component contributions to hygroscopicity parameter κ for 22 May 2012.

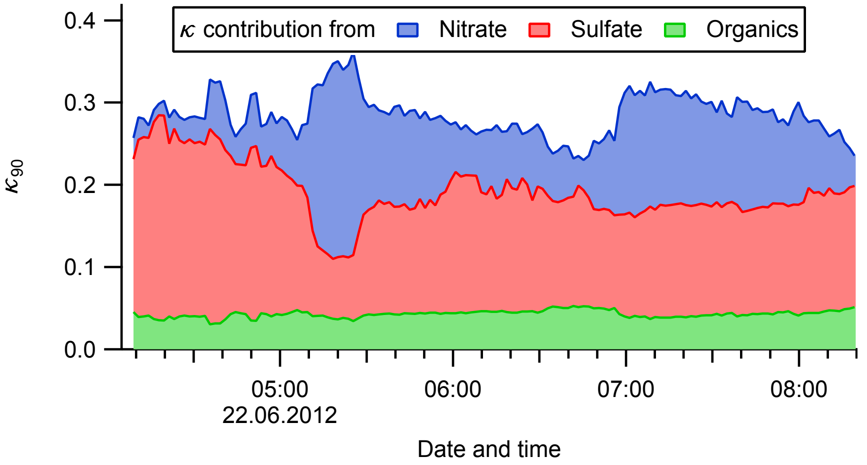

Figure B.2.: Aerosol component contributions to hygroscopicity parameter κ for 22 June 2012.

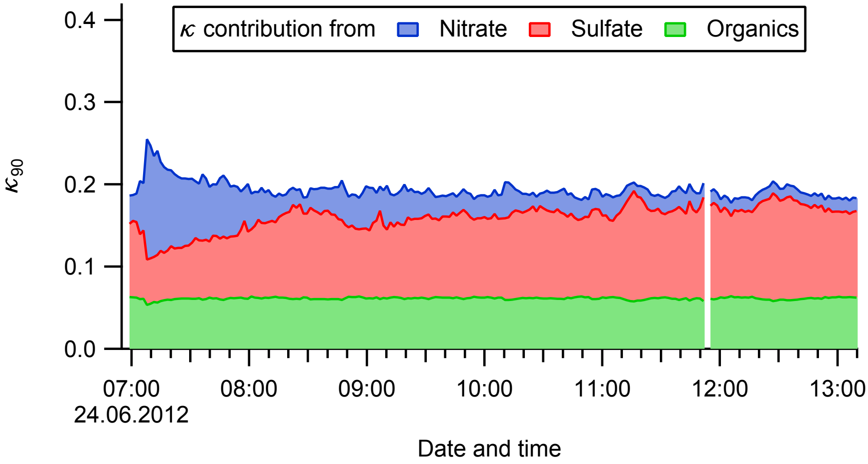

Figure B.3.: Aerosol component contributions to hygroscopicity parameter κ for 24 June 2012.

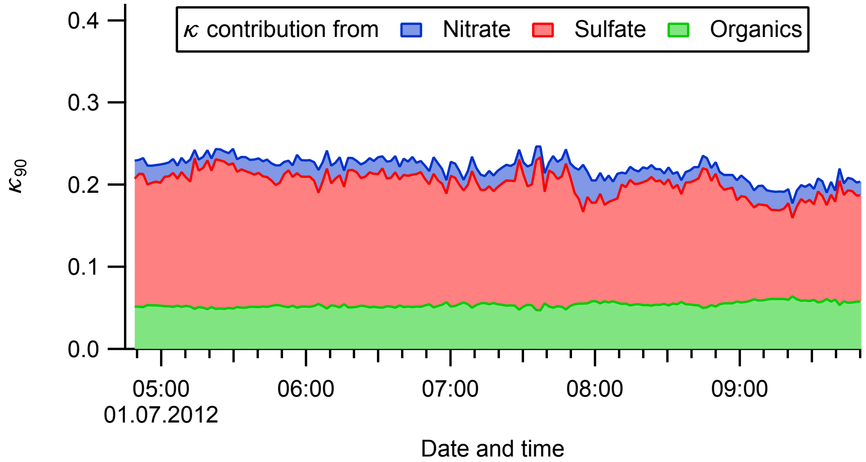

Figure B.4.: Aerosol component contributions to hygroscopicity parameter κ for 1 July 2012.

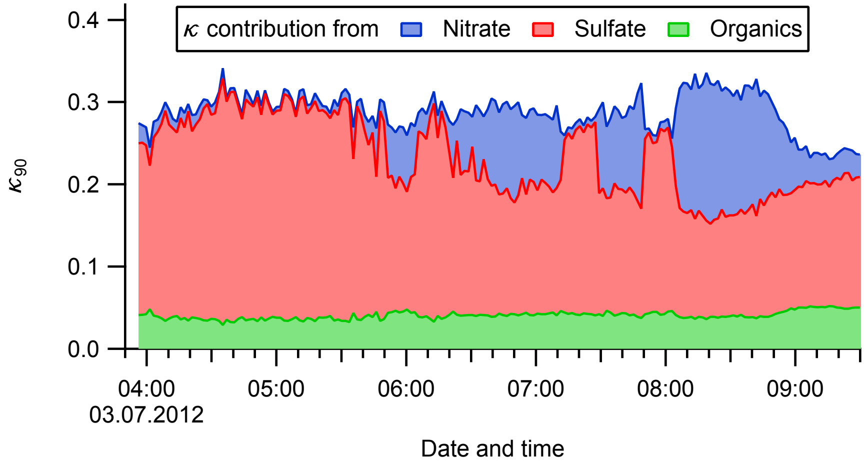

Figure B.5.: Aerosol component contributions to hygroscopicity parameter κ for 3 July 2012.

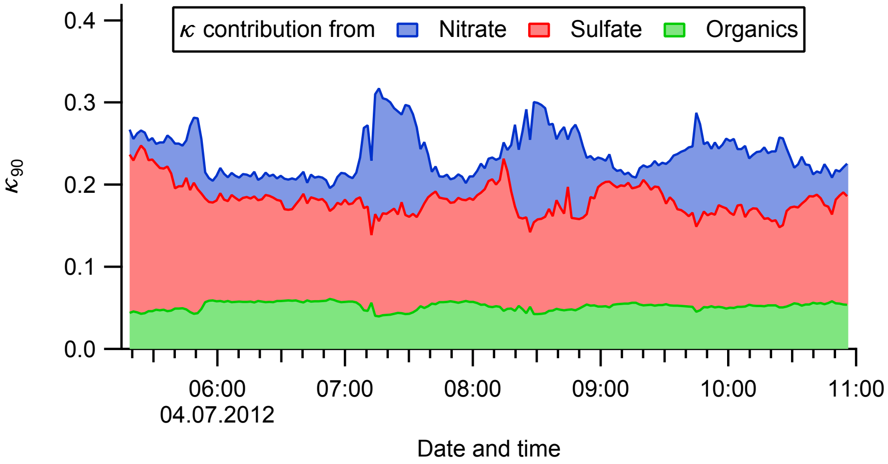

Figure B.6.: Aerosol component contributions to hygroscopicity parameter κ for 4 July 2012.

Acknowledgements

An dieser Stelle möchte ich mich bei all denen bedanken, ohne die diese Arbeit nicht gelungen wäre.

Ein großer Dank geht an Prof. Dr. Thorsten Benter für die Übernahme der universitären Betreuung. Prof. Dr. Andreas Wahner möchte ich für die Möglichkeit, am IEK-8 die hier dargestellten Arbeiten durchzuführen und für die Bereitschaft, diese Arbeit zu begutachten danken. Außerdem danke ich Prof. Dr. Wiesen und PD Dr. Hendrik Kersten für die Bereitschaft, in der Prüfungskommission mitzuwirken.

Ein besonders großes Dankeschön geht an PD Dr. Thomas Mentel, in dessen Arbeitsgruppe ich drei überaus lehrreiche, ereignisreiche und schöne Jahre verbringen durfte. Dr. Achim Trimborn gebührt mein Dank für die großartige Zusammenarbeit während dem Aufbau des Zeppelin-AMS und für die Bereitschaft, sein schier unendliche Wissen rund um das AMS und seine Macken jederzeit zur Verfügung zu stellen. Bei Wolfgang Lüdtke bedanke ich mich für die tolle Hilfe bei allen kleinen und großen elektronischen Aufgaben und Problemen. Dr. Christian Spindler und Dr. Amewu Mensah möchte ich für die Einarbeitung in die Bedienung und Datenauswertung des AMS danken. Bei Dr. Olaf Stein möchte ich mich für die aufschlussreichen Diskussionen über die meteorologisch angehauchten Aspekte dieser Arbeit bedanken. Dem ZAT (heute ZEA-1), insbesondere Dipl. Ing. Knut Dahlhoff gilt mein Dank für die großartige Unterstützung in technischen Fragen und bei der Herstellung der für das Zeppelin AMS benötigten Teile. Beim ZCH (heute ZEA-3) bedanke ich mich für die Unterstützung bei der Umsetzung des Verfahrens zum Erstellen eines Aluminium-Materialnachweises.

Für die gute Zusammenarbeit möchte ich mich auch bei der Firma Zeppelin Luftschifftechnik GmbH bedanken, insbesondere bei Herrn Franck, der große Geduld im Umgang mit nur langsam besser werdenden 3D-CAD Zeichnungen bewiesen hat.

Ich danke Bernadette Rosati, Ralf Tillmann, Dr. Franz Rohrer, Dr. Robert Wegener und Julia Jäger für die zur Verfügung gestellten Daten ihrer Messinstrumente. Insgesamt möchte ich mich beim PEGASOS Kampagnen-Team für die tolle Zeit bedanken, es hat einfach großen Spaß gemacht mit euch!

The PEGASOS project is funded by the European Commission under the Framework Programme 7 (FP7-ENV-2010-265148).

Band / Volume 184
IEK-3 Report 2013. Durable Electrochemical Process Engineering
(2013), ca. 180 pp
ISBN: 978-3-89336-893-8

Band / Volume 185
Light Trapping with Plasmonic Back Contacts
in Thin-Film Silicon Solar Cells
U. W. Paetzold (2013), X, 175 pp
ISBN: 978-3-89336-895-2

Band / Volume 186
Plant-plant interactions, biodiversity & assembly
in grasslands and their relevance to restoration
V. M. Temperton (2013), ca 420 pp
ISBN: 978-3-89336-896-9

Band / Volume 187
Ab initio investigation of ground-states and ionic motion
in particular in zirconia-based solid-oxide electrolytes
J. A. Hirschfeld (2013), v, 144 pp
ISBN: 978-3-89336-897-6

Band / Volume 188
Entwicklung protonenleitender Werkstoffe und Membranen
auf Basis von Lanthan-Wolframat für die Wasserstoffabtrennung
aus Gasgemischen
J. Seeger (2013), V, 130 pp
ISBN: 978-3-89336-903-4

Band / Volume 189
Entwicklung und Herstellung von metallgestützten Festelektrolyt-
Brennstoffzellen (MSC-SOFC) mit einem Sol-Gel-Elektrolyten
S. D. Vieweger (2013), xviii, 176 pp
ISBN: 978-3-89336-904-1

Band / Volume 190
Mobile Brenngaserzeugungssysteme
mit Mitteldestillaten für Hochtemperatur-PEFC
C. Wiethege (2013), iii, 179 pp
ISBN: 978-3-89336-905-8

Schriften des Forschungszentrums Jülich
Reihe Energie & Umwelt / Energy & Environment

Band / Volume 191
Verbundvorhaben Öko-effiziente Flugzeugsysteme für die nächste Generation (EFFESYS) - Teilprojekt Brennstoffzelle, Infrastruktur, Komponenten und System (BRINKS) – Schlussbericht
J. Pasel, R.C. Samsun, H. Janßen, W. Lehnert, R. Peters, D. Stolten
(2013), xii, 152 pp
ISBN: 978-3-89336-908-9

Band / Volume 192
Analyse des Betriebsverhaltens von Hochtemperatur-Polymerelektrolyt-Brennstoffzellen
L. Lüke (2013), 156 pp
ISBN: 978-3-89336-909-6

Band / Volume 193
Full-waveform inversion of crosshole GPR data for hydrogeological applications
A. Klotzsche (2013), X, 164 pp
ISBN: 978-3-89336-915-7

Band / Volume 194
Long Term Stability and Permeability of Mixed Ion Conducting Membranes under Oxyfuel Conditions
X. Li (2013), III, 143 pp
ISBN: 978-3-89336-916-4

Band / Volume 195
Innovative Beschichtungs- und Charakterisierungsmethoden für die nasschemische Herstellung von asymmetrischen Gastrennmembranen auf Basis von SiO_2
J. Hoffmann (2013), V, 152 pp
ISBN: 978-3-89336-917-1

Band / Volume 196
Aerosol processes in the Planetary Boundary Layer: High resolution Aerosol Mass Spectrometry on a Zeppelin NT Airship
F. Rubach (2013), iii, 141 pp
ISBN: 978-3-89336-918-8

Weitere ***Schriften des Verlags im Forschungszentrum Jülich*** unter
http://wwwzb1.fz-juelich.de/verlagextern1/index.asp

Energie & Umwelt / Energy & Environment
Band / Volume 196
ISBN 978-3-89336-918-8